

A Holistic Study on Flow and Thermal Characteristics of Non-  
Stochastic Strut-Based and Surface-Based Lattice Structures for  
Gas Turbine Engines



McGill

Shivangi Sarabhai  
Department of Mechanical Engineering  
McGill University, Montreal

September 2022

A thesis submitted to McGill University in partial fulfillment  
of the requirements of the degree of Master of Science

© Shivangi Sarabhai, 2022

## **Abstract**

Lattice structures are known for their capability to be tailored for achieving specific properties such as high porosity and strength, impact energy absorption and light-weighting. Literature survey showed that the mechanical performance of the strut-based and surface-based lattice structures has already been investigated in the past. However, very little research has been conducted to investigate their flow and heat transfer performance, especially for strut-based lattice structures. This research systematically investigates the friction factor and convective heat transfer coefficient across both strut-based and surface-based lattice structures. Data collection and analysis are conducted to identify the range of suitable strut diameter, surface thickness, strut length, and porosity used in the industries. The dimensions selected to model the lattice structures geometrically are based on the data available in the literature. The modelled structures are simulated in the convective heat transfer environment to gather the heat transfer coefficient and friction factor outputs. Surface-based lattice structures showed optimum performance for both flow and thermal characteristics. The simulation results are populated to define a flow and thermal property chart to support design engineers in selecting potential lattice structures.

## Résumé

Les structures cellulaires périodiques sont reconnues pour leur capacités d'adaptation permettant d'obtenir des propriétés spécifiques comme une porosité et une résistance mécanique élevées, une absorption d'énergie d'impact élevée et une structure légère. La revue bibliographique a montré que les structures cellulaires réticulées périodiques et les structures cellulaires à base de surfaces périodiques ont déjà été traitées par le passé. Cependant, peu de recherches ont été menées pour déterminer leurs propriétés hydrodynamiques et thermiques en particulier pour les structures réticulées périodiques. Ce travail cherche à déterminer systématiquement le coefficient de frottement et la conductivité thermique des structures cellulaires à base de surfaces périodiques et des structures réticulées périodiques. La récolte de données et leur analyse sont conduites afin d'identifier l'intervalle adapté de diamètre des barres des cellules réticulées, de l'épaisseur des surfaces périodiques, de la longueur des barres des cellules réticulées et de la porosité utilisés en industrie. Les dimensions choisies pour modéliser géométriquement les structures réticulées sont basées sur les données disponibles dans la littérature. Les structures ainsi modélisées sont simulées dans un environnement thermique afin de déterminer la conductivité thermique et le coefficient de frottement. Les structures cellulaires à base de surfaces périodiques ont montré des performances optimales à la fois pour les caractéristiques hydrodynamiques et thermiques. Les résultats de simulation sont renseignés dans un graphique de propriétés hydrodynamiques et thermiques afin d'aider les ingénieurs de conception mécanique à choisir de potentielles structures cellulaires périodiques.

## **Acknowledgements**

Foremost, I would like to express my sincere gratitude to my supervisor, Dr. Yaoyao Fiona Zhao, who continually supported me throughout this research. She always steered me in the right direction whenever she thought I needed it. I have learned the importance of punctuality and perseverance from her. These two qualities have immensely helped me to swim through difficult situations, which ultimately helped me complete my research.

I am also very fortunate to get a team of industry supervisors from Siemens Energy, Montreal. I am grateful to Fabian Sanchez, who has the attitude and the substance of a genius. He always conveyed a spirit of adventure for this research to me. I am also thankful to Mitch Kibsey for reviewing my research progress every week and finding all the possible resources for me, which helped me to understand the results of this research. Furthermore, I would like to thank all the members of the additive manufacturing team of Siemens Energy in Montreal, who always answered my pettiest doubts regarding CFD and guided me to understand the science behind it.

I would also like to acknowledge all my colleagues from Additive Design and Manufacturing Lab, McGill, who have always been there at the need of the hour.

Words are always short of expressing my gratitude for my parents and my brother. I am deeply indebted to their constant support and motivation. Without their hard work and perseverance, I would not have been able to achieve my goals. Along with them, my friends have always been my source of happiness.

Last but not least, I am thankful that I got to foster a cat named Luna during the last phase of my research. She always made sure to be by my side whenever I felt exhausted. She came into my life when I needed a companion and taught me a very different and unconditional love language.

# Table of Contents

Abstract.....	i
Résumé.....	ii
Acknowledgements.....	iii
Table of Contents.....	iv
List of Acronyms and Abbreviations.....	vii
List of Tables.....	x
List of Figures.....	xi
Chapter 1: Introduction.....	1
1.1 History of Additive Manufacturing.....	1
1.2 Lattice Structures.....	4
1.3 Applications of Lattice Structures.....	8
1.4 Motivation of the Research.....	10
1.5 Problem Statement and Roadmap of the Thesis.....	12
Chapter 2: Literature Review.....	14
2.1 Mechanical Performance of Lattice Structures.....	14
2.1.1 Compressive Performance of Lattice Structures.....	16
2.1.2 Fatigue Performance of Lattice Structures.....	21
2.2 Heat Transfer Properties of Lattice Structures.....	22
2.2.1 Heat Transfer Coefficient.....	24
2.2.2 Nusselt's Number.....	26
2.2.3 Friction Factor.....	27
2.3 Analysis of the Data Reported in the Literature.....	29
2.3.1 Data Collection and Data Filtration.....	29
2.3.2 Data Analysis.....	32

2.4 Simulation Setup for Heat Transfer .....	33
2.4.1 Computational Flow Domain .....	34
2.4.2 Mesh or Grid Convergence Study .....	37
2.5 Research Gaps in the Literature and Research Scope .....	40
2.5.1 Gaps in the literature.....	40
2.5.2 Scope Definition .....	41
Chapter 3: Methodology .....	43
3.1 Geometric Modelling .....	43
3.1.1 Strut-Based lattice structures .....	44
3.1.2 Surface-Based Lattice Structures.....	48
3.2 Simulation .....	52
3.2.1 Constructing Computational Domain.....	53
3.2.2 Surface Repair .....	54
3.2.3 Mesh Generation.....	55
3.2.4 Boundary Conditions and Choice of Solvers .....	55
Chapter 4: Results and Discussions .....	59
4.1 Mesh Convergence Study.....	60
4.2 Dimensional Characteristics of Lattice Structures .....	61
4.3 Flow Performance Characteristics .....	63
4.3.1 Flow Characteristics of Primitive Lattice Structures.....	64
4.3.2 Flow Characteristics of BCC, BCCZ, FCC and FCCZ Lattice Structures.....	64
4.3.3 Flow Characteristics of Octahedron and Octet Truss Lattice Structures.....	66
4.3.4 Flow Characteristics of Surface-Based Lattice Structures .....	67
4.4 Heat Transfer Characteristics .....	70
4.4.1 Convective Heat Transfer Coefficient of Strut-Based Lattice Structures .....	70

4.4.2 Convective Heat Transfer Coefficient of Surface-Based Lattice Structures .....	74
4.4.3 Nusselt's Number for Benchmarking .....	74
4.5 Flow and Thermal Property charts .....	76
Chapter 5: Conclusions and Future Work.....	82
5.1 Conclusions .....	82
5.2 Future Scope.....	83
Appendix A.....	84
Appendix B .....	87
References .....	89

## List of Acronyms and Abbreviations

2D	Two Dimensional
3D	Three Dimensional
AM	Additive Manufacturing
ANSYS	Analysis System
ASTM F42	American Society for Testing and Materials (F42 Committee)
BCC	Body Centered Cubic
BCC(Z)	BCC and BCCZ
BCC1	BCC Lattice Structure with Strut Diameter of 1 mm
BCC1.5	BCC Lattice Structure with Strut Diameter of 1.5 mm
BCC2	BCC Lattice Structure with Strut Diameter of 2 mm
BCCZ	Body Centered Cubic with z-struts
BCCZ1	BCCZ Lattice Structure with Strut Diameter of 1 mm
BCCZ1.5	BCCZ Lattice Structure with Strut Diameter of 1.5 mm
BCCZ2	BCCZ Lattice Structure with Strut Diameter of 2 mm
B-rep.	Boundary Representation
CAD	Computer Aided Design
CAE	Computer Aided Engineering
CCP	Closed Cubic Packed
CFD	Computational Fluid Dynamics
CFR	Continuous Fiber Reinforcement
CHT	Convective Heat Transfer
CSG	Constructive Solid Geometry
DIY	Do It Yourself
DLP	Digital Light Processing
DMLS	Direct Metal Laser Sintering
EBM	Electron Beam Melting
FCC	Face Centered Cubic
FCC(Z)	FCC and FCCZ
FCC1	FCC Lattice Structure with Strut Diameter of 1 mm

FCC1.5	FCC Lattice Structure with Strut Diameter of 1.5 mm
FCC2	FCC Lattice Structure with Strut Diameter of 2 mm
FCCZ	Face Centered Cubic with z-struts
FCCZ1	FCCZ Lattice Structure with Strut Diameter of 1 mm
FCCZ1.5	FCCZ Lattice Structure with Strut Diameter of 1.5 mm
FCCZ2	FCCZ Lattice Structure with Strut Diameter of 2 mm
FDM	Fused Deposition Modelling
FE	Finite Element
FEA	Finite Element Analysis
FEM	Finite Element Methods
FFF	Fused Filament Fabrication
HTC	Heat Transfer Coefficient
LAM	Laser Additive Manufacturing
LFM	Lattice Frame Materials
LMD	Laser Metal Deposition
LOM	Laminated Object Manufacturing
MJM	Multi Jet Modelling
Octahedron1	Octahedron Lattice Structure with Strut Diameter of 1 mm
Octahedron1.5	Octahedron Lattice Structure with Strut Diameter of 1.5 mm
Octahedron2	Octahedron Lattice Structure with Strut Diameter of 2 mm
Octet Truss1	Octet Truss Lattice Structure with Strut Diameter of 1 mm
Octet Truss1.5	Octet Truss Lattice Structure with Strut Diameter of 1.5 mm
Octet Truss2	Octet Truss Lattice Structure with Strut Diameter of 2 mm
PBIH	Powder bed and inkjet head
Poly.	Polynomial
PP	Plaster based 3D Printing
Primitive1	Primitive Lattice Structure with Strut Diameter of 1 mm
Primitive1.5	Primitive Lattice Structure with Strut Diameter of 1 mm
Primitive2	Primitive Lattice Structure with Strut Diameter of 2 mm
RAM	Random Access Memory
RANS	Reynolds-averaged Navier-Stokes

RCO	Rhombic Cuboctahedron
RD	Rhombic dodecahedron
SGT-A65	Siemens Gas Turbine-Aero-derivative-65
SHC	Square Honeycomb
SHS	Selective Heat Sintering
SLA	Stereolithography
SLM	Selective Laser Melting
SLS	Selective Laser Sintering
SST	Shear Stress Transport
TCO	Truncated Cuboctahedron
TPMS	Triply Periodic Minimal Surface
TPMS Diamond1	TPMS Diamond Lattice Structure with Surface Thickness of 1 mm
TPMS Diamond1.5	TPMS Diamond Lattice Structure with Surface Thickness of 1.5 mm
TPMS Diamond2	TPMS Gyroid Lattice Structure with Surface Thickness of 2 mm
TPMS Gyroid1	TPMS Gyroid Lattice Structure with Surface Thickness of 1 mm
TPMS Gyroid1.5	TPMS Gyroid Lattice Structure with Surface Thickness of 1.5 mm
TPMS Gyroid2	TPMS Diamond Lattice Structure with Surface Thickness of 2 mm
TPMS I-WP	TPMS, I-Graph and Wrapped Package Graph
UC	Ultrasonic Consolidation
UK	United Kingdom
US	United States

## List of Tables

Table 1.1 A Timeline of 3D Printing Technology (Adapted from González [4]) .....	2
Table 1.2 Seven AM Process Categories by ASTM F42 (Adapted from Reddy and Dufera [6])..	3
Table 1.3 Periodic Lattice Structures and their pros (Adapted from Varotsis [8]).....	7
Table 2.1 Value ranges of flow and thermal properties of lattice structures from the literature ..	28
Table 2.2 Dimensional parameters .....	32
Table 2.3 Difference between the box and cylindrical flow domain (adapted from idealsimulations [42]) .....	37
Table 2.4 Mesh Convergence study based on element size [34] .....	39
Table 2.5 Errors captured in StarCCM+ (Adapted from Lidar [45] and Behera [46]).....	40
Table 3.1 Strut-Based lattice structures topology representation .....	46
Table 3.2 Boundary Conditions throughout the research .....	56
Table 3.3 Nomenclature of lattice structures with different dimensions of struts and surfaces ...	58
Table 4.1 Sensitivity Analysis .....	60

## List of Figures

Figure 1.1 Classification of Cellular Structures [7] .....	5
Figure 1.2: Non-Stochastic lattice structures – a) A strut-based lattice structure; b) A TPMS lattice structure (Gyroid) (Adapted from Varotsis [8]).....	6
Figure 1.3 Lattice structures that can be generated in nTopology (Adapted from Varotsis [8])....	7
Figure 1.4 Strut-based Lattice Structures.....	8
Figure 1.5 Surface-based Lattice Structures .....	8
Figure 1.6 Aerojet Rocketdyne modelled using the "Shell and infill " technique [8] .....	9
Figure 1.7 Riddell Speed flex helmet with its side lattice liners by Carbon 3D [9] .....	9
Figure 1.8 Cold plate in power electronics modelled using TPMS Gyroid [8] .....	10
Figure 1.9 Gas Turbine representation by Kawasaki [10] .....	11
Figure 1.10 Material Property chart by Mike Ashby [11] .....	12
Figure 1.11 Research Roadmap .....	13
Figure 2.1 a) Bending dominated , b) Stretch dominated structure [13] .....	14
Figure 2.2 a) Bending-dominated structure, b) Stretch-dominated structure, c) Over-constrained or state of self-stress [12].....	15
Figure 2.3 Comparison of bending-dominated and stretch-dominated structures [17] .....	17
Figure 2.4 Separate stress-strain diagrams of a) Bending-dominated lattice structures, b)Stretch-dominated lattice structures [12].....	17
Figure 2.5 Converting bending dominated to stretch-dominated lattice structures .....	18
Figure 2.6 Stress-strain curve comparison for BCC(Z) and FCC(Z) lattice structure topologies [21].....	19
Figure 2.7 Unit Cell of BCC and BCCZ, when L= Strut Length, D = Strut Diameter .....	19
Figure 2.8 Stress-strain curves of lattice structures with different strut lengths L under compression [25].....	20
Figure 2.9 Stress-strain curves of lattice structures with different strut diameters D under compression [25].....	21
Figure 2.10 A: Fatigue performance of lattice structures with Diamond (D) and truncated cuboctahedron (C) topologies and varying relative densities (%). B: Failure stress after $50 \times 10^3$ cycles and relative densities of these topologies [30]......	22
Figure 2.11 Working process of a heat exchanger with lattice structure [36] .....	23

Figure 2.12 Overall heat transfer coefficient $\bar{h}$ with varying fluid velocity and relative densities [37].....	24
Figure 2.13 Variation of overall HTC with a) cold fluid mass flow b) hot fluid mass flow [33].	25
Figure 2.14 Nusselt number variation with Reynolds number for both internal and external pipe flow [33].....	26
Figure 2.15 Nusselt's number variation at different Reynold's number for the Rhombi-Octet [39] .....	27
Figure 2.16 Percentage use of different topologies across the literature .....	30
Figure 2.17 Industries using lattice structures .....	30
Figure 2.18 Percentage usage of manufacturing technologies in AM .....	31
Figure 2.19 Percentage use of different materials in AM.....	31
Figure 2.20 Finite element model process [41] .....	34
Figure 2.21 a) Experimental setup for open foams b) Lattice structure with cubic unit cell is used for the setup (the nomenclature used in this figure is different from the rest of the thesis) [37]..	35
Figure 2.22 (a) notations for setup; (b) hexagonal cells representation; (c) representation of fin attachment to the walls; and (d) local coordinates. [35] .....	35
Figure 2.23 Test rig with LFM model [38].....	36
Figure 2.24 Isometric view of the computational flow domain [40] .....	36
Figure 2.25 Terminologies while creating mesh [43] [44] .....	37
Figure 2.26 Levels of mesh.....	38
Figure 2.27 Levels of mesh – (reference: Figure 2.20).....	38
Figure 2.28 Mesh convergence study based on the number of elements in the whole geometry [33].....	39
Figure 3.1 Topology selection for modelling (adapted from Figure 2.16) .....	43
Figure 3.2 Modelling Strut-Based lattice structures in NX .....	44
Figure 3.3 Schematic representation of modelling .....	45
Figure 3.4 Distance field representation in nTopology for a sphere. [49].....	48
Figure 3.5 Boolean operations form new faces, vertices, and edges in Conventional CAD techniques. [49].....	49
Figure 3.6 Left: Boolean union, Right: Boolean intersect [49] .....	49
Figure 3.7 a) A circle represented in a B-rep and b) a distance field (right) [50].....	50

Figure 3.8 Distance Field for TPMS Gyroid .....	51
Figure 3.9 Geometry for TPMS Gyroid.....	51
Figure 3.10 Distance Field for TPMS Diamond.....	52
Figure 3.11 Geometry for TPMS Diamond .....	52
Figure 3.12 Computational flow domain for simulation .....	53
Figure 3.13 Surface Repair in Star CCM+ .....	54
Figure 3.14 Mesh Generation .....	55
Figure 4.1 Planes chosen for sensitivity analysis.....	59
Figure 4.2 Mesh/Grid Convergence results for Octet Truss .....	61
Figure 4.3 Mesh/Grid Convergence results for TPMS Diamond .....	61
Figure 4.4 Variation of surface area to volume ratio with porosity of strut-based lattice structures .....	62
Figure 4.5 Variation of surface area to volume ratio with porosity of surface-based lattice structures.....	63
Figure 4.6 Friction factor augmentation ( $f/f_0$ ) across 3 different Reynold's number for Primitive lattice structures .....	64
Figure 4.7 Friction factor augmentation ( $f/f_0$ ) across three different Reynold's numbers for BCC and BCCZ .....	65
Figure 4.8 Friction factor augmentation ( $f/f_0$ ) across three different Reynold's numbers for FCC(Z).....	66
Figure 4.9 Friction factor augmentation ( $f/f_0$ ) across three different Reynold's numbers for Octet Truss and Octahedron .....	67
Figure 4.10 Friction factor augmentation ( $f/f_0$ ) across three different Reynold's numbers for Surface-based lattice structures.....	68
Figure 4.11 Friction Factor augmentation ( $f/f_0$ ) @Re=30000 for benchmarking the results.....	69
Figure 4.12 Friction factor augmentation ( $f/f_0$ ) across the Reynolds number range. [55].....	69
Figure 4.13 Convective HTC ( $W/(m^2-K)$ ) variation for BCC and BCCZ.....	70
Figure 4.14 Convective HTC ( $W/(m^2-K)$ ) variation for FCC and FCCZ.....	71
Figure 4.15 Convective HTC ( $W/(m^2-K)$ ) variation for Octahedron and Octet Truss .....	71
Figure 4.16 HTC ( $W/(m^2-K)$ ) variation with surface area to volume ratio ( $m^{-1}$ ) for different topologies.....	73

Figure 4.17 Convective HTC ( $W/(m^2-K)$ ) variation for surface-based lattice structures.....	74
Figure 4.18 Nusselt's number values for benchmarking.....	75
Figure 4.19 Nusselt's number for all lattice structure samples tested [55].....	75
Figure 4.20 CHT( $W/m^2-K$ ) vs. Friction Factor Augmentation ( $f/f_0$ ) at Reynold's number 292,000 for strut diameter/surface thickness of 1 mm.....	77
Figure 4.21 CHT( $W/m^2-K$ ) vs. Friction Factor Augmentation ( $f/f_0$ ) at Reynold's number 292,000 for strut diameter/surface thickness of 1.5 mm.....	77
Figure 4.22 CHT( $W/m^2-K$ ) vs. Friction Factor Augmentation ( $f/f_0$ ) at Reynold's number 292,000 for strut diameter/surface thickness of 2 mm.....	78
Figure 4.23 CHT( $W/m^2-K$ ) vs. Friction Factor Augmentation ( $f/f_0$ ) at Reynold's number 30,000 for strut diameter/surface thickness of 1 mm.....	78
Figure 4.24 CHT( $W/m^2-K$ ) vs. Friction Factor Augmentation ( $f/f_0$ ) at Reynold's number 30,000 for strut diameter/surface thickness of 1.5 mm.....	79
Figure 4.25 CHT( $W/m^2-K$ ) vs. Friction Factor Augmentation ( $f/f_0$ ) at Reynold's number 30,000 for strut diameter/surface thickness of 2 mm.....	79
Figure 4.26 CHT( $W/m^2-K$ ) vs. Friction Factor Augmentation ( $f/f_0$ ) at Reynold's number 1,800 for strut diameter/surface thickness of 1 mm.....	80
Figure 4.27 CHT( $W/m^2-K$ ) vs. Friction Factor Augmentation ( $f/f_0$ ) at Reynold's number 1,800 for strut diameter/surface thickness of 1.5 mm.....	80
Figure 4.28 CHT( $W/m^2-K$ ) vs. Friction Factor Augmentation ( $f/f_0$ ) at Reynold's number 1,800 for strut diameter/surface thickness of 2 mm.....	81

# **Chapter 1: Introduction**

## **1.1 History of Additive Manufacturing**

Historically, humans are linked with making artifacts using stones, wood, and metal, to give value to raw materials by shaping them into valuable finished goods. The earliest examples of this are traced back to the stone age when we created tools to create valuable things from them. Soon this became the source of living for us by creating different markets to sell these finished goods. Then, human labour, capital, and new techniques helped to expand these markets. Thus, it became a business to earn profits. This expansion was possible when people came forward and formed organizations to manufacture at a large scale. Furthermore, the third industrial revolution in the 20<sup>th</sup> century aided in optimizing the production process. The optimization was possible when the transition from human labour technology to machinery happened, turning artisans into waged workers. One such human labour technique is subtractive manufacturing, where the material is removed and finished to give a customized product [1].

In the 1980s, when the US cold war was approaching its end, military funding for research and development increased, leading to innovative ideas and harnessing manufacturing potential, one of which was - Additive manufacturing (AM). Objectively, it all started when Dr. Hideo Kodama, in the early 1980s, took inspiration from 3D scanning and topographical maps and created a prototyping machine. Four years later, the stereolithography apparatus using UV light to form cross polymers, also known as SLA, was invented by Charles Hull, who further established the first 3D printing company and 3D printing machine in 1986 and 1987, respectively [2].

It should be noted that AM includes a broader range of technologies where the addition of material is not necessarily in layers, and 3D printing is one of them. Nevertheless, it all started with layer-on-layer production, i.e., 3D printing. The invention by Charles Hull inspired Dr. Carl Deckard to replace UV light with the laser to solidify layers of powdered polymers inventing another rival technology- Selective Laser Sintering (SLS). Thus, with the advent of Stereolithography, researchers started exploring and developing new techniques for 3D printing. In 1991, Scott Crump co-founded a new company, Stratasys, to patent a new technology called Fused Deposition Modeling (FDM), probably the most prominent 3D printing technology today. FDM is a material [3] extrusion process from a nozzle to join it to 3D print. Then, the Laminated Object Technology and Solid Ground Curing [2].

In the 2000s, more companies joined the force to build the best technique and machines for 3D printing. Companies like RepRap emerged to make self-replicating machines proliferating FDM 3D printers. This motivated MakerBot (2009) to produce DIY kits for hobbyists trying to create their prototypes and illustrations by 3D printing the ideas. These hobbyists gave new theories of design and prototyping, resulting in the formation of new companies like Prusa Research in 2011, producing a new concept called Prusa i3 3D based on early research on the RepRap machine.

In 2013, revolutionized approaches like Fused Filament Fabrication (FFF) and Continuous Fiber Reinforcement (CFR) were adopted for 3D printers, which added strength and rigidity to the printed parts [2].

A complete summary of the history of AM technology is summarized in Table 1.1

Table 1.1 A Timeline of 3D Printing Technology (Adapted from González [4])

1980	First 3D printing patent application by Hideo Kodama, detailing a system to harden the material using UV rays.
1983	Charles Hull invents the first SLA machine
1986	<ol style="list-style-type: none"> <li>1. First Patent of SLA.</li> <li>2. Hull co-founded 3D Systems Corporation.</li> </ol>
1987	Carl Deckard files patent for SLS process, which was acquired by DTM, Inc in 1989 and was later acquired by 3D systems.
1988	Printer SLA-1 by 3D systems.
1989	<ol style="list-style-type: none"> <li>1. The first patent for FDM. Scott Crump co-founds Stratasys.</li> <li>2. EOS GmbH in Germany becomes a leader in SLS research.</li> </ol>
1997	Aeromat introduces the first metal 3D printer using laser additive manufacturing (LAM)
1999	Applications in Biomedical.
2005	The RepRap open-Source concept is created to replicate printers by Dr. Adrian Bowyer.
2008	<ol style="list-style-type: none"> <li>1. “Darwin,” the first 3D printer under RepRap.</li> <li>2. Shapeways gives 3D printing services for users to customize their designs</li> </ol>
2009	<ol style="list-style-type: none"> <li>1. Patent by Stratasys for FDM expires.</li> </ol>

	<p>2. Makerbot introduces do-it-yourself kits</p> <p>3. Makerbot invents the Thingsiverse file library for customizable files to download and upload.</p>
2011	The University of Southampton 3D prints the first unmanned aircraft.
2012	B9Creator launches alternative 3D printing processes: DLP Technology and Stereolithography
2013	Stratasys acquires Makerbot
2015	Cellink commercializes bio-ink and releases INKREDIBLE, 3D printer for bioprinting.
2019	As the patents starts to expire, now there are over 170 3D printer manufacturers worldwide like Formlabs, Prusa, Desktop Metal and many others.

In 2012, ASTM standardized the definition of different types of AM technologies, as shown in Table 1.2.

Table 1.2 Seven AM Process Categories by ASTM F42 (Adapted from Reddy and Dufera [6])

<b>AM Technology</b>	<b>Material and Description</b>	<b>Related Technology and Companies</b>
Powder Bed Fusion	Thermal energy selectively solidifies the regions of the powder bed. (Metals, Polymers)	Electron beam melting (EBM), selective laser sintering (SLS), selective heat sintering (SHS), and direct metal laser sintering (DMLS).
		EOS(Germany), 3D Systems (US), Arcam (Sweden)
Directed Energy Deposition	As the material is deposited, focused thermal energy melts and solidifies it (Metals)	Laser metal deposition (LMD).
		Optomec (US), POM (US)

<b>AM Technology</b>	<b>Material and Description</b>	<b>Related Technology and Companies</b>
Material Extrusion	Material is dispensed through a orifice or a nozzle (Polymers)	Fused Metal Deposition
		Stratasys (Israel), Bits from Bytes (UK)
Vat Photo polymerization	Liquid photopolymer is cured by light. (Photopolymers)	Stereo lithography (SLA), digital light processing (DLP)
Binder Jetting	A liquid bonding agent is used to bond material selectively. (Polymers, Foundry Sand, Metals)	Powder bed and inkjet head (PBIH), plaster-based 3D printing (PP). 3D Systems (US), Ex One (US)
Polymers, Foundry Sand, Metals	Droplets material is deposited selectively. (Polymers, Waxes)	Multi-jet modelling (MJM). Object (Israel), 3DSYSTEMS (US)
Sheet Lamination	Sheets of material are bonded. (Paper, Metals)	Laminated object manufacturing (LOM), ultrasonic consolidation (UC). Fabrisonic (US), Mcor (Ireland)

## 1.2 Lattice Structures

Nature gives the best designs; thus, humans have been imitating cellular structures to achieve accuracy close to what natural structures offer. Animal bones, leaves, corals, shark skin and beehives are examples of these structures. These cellular structures can be classified into stochastic and non-stochastic structures depending on how the unit cells are arranged in the 3D space. These again can be divided into two subcategories, namely, open cell and closed cell form. Open cell structures are usually designed to let fluids pass through them freely, as these structures have open cell walls. In contrast, the closed cell category has intact walls for impermeability. Also, stochastic structures consist of metallic and non-metallic foams, which have properties like sponges. Whereas non-stochastic structures behave like trusses and honeycombs since a unit cell's arrangement is

generally repetitive and known as lattice structures [7]. Figure 1.1 gives a brief and diagrammatic classification of cellular structures.

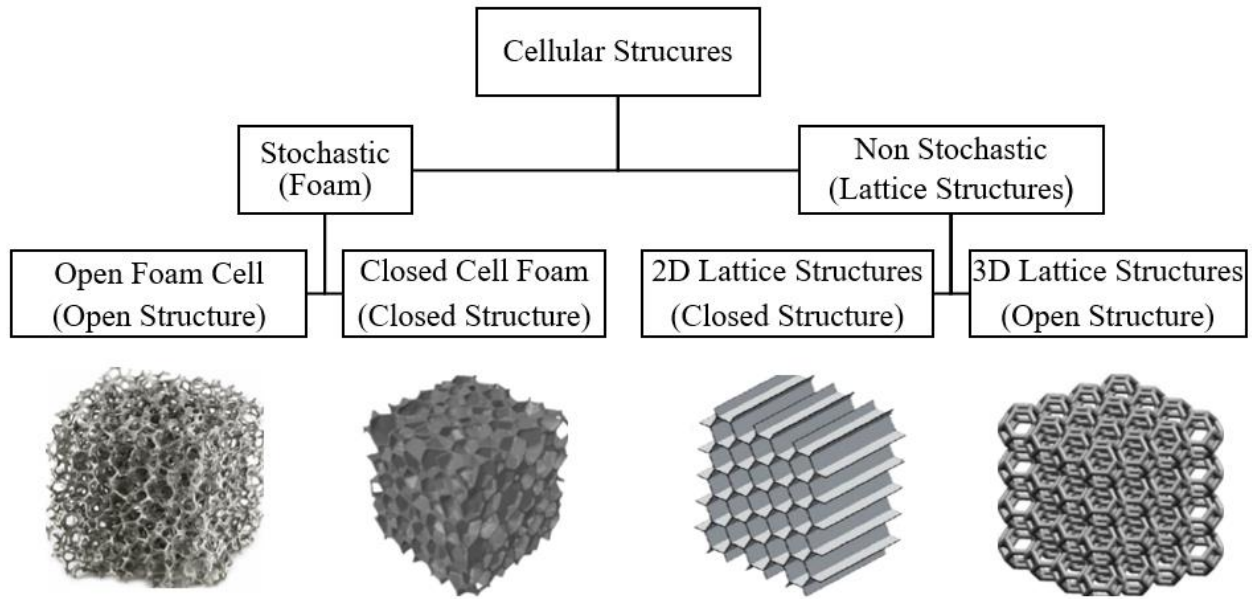


Figure 1.1 Classification of Cellular Structures [7]

Additive Manufacturing makes the fabrication of lattice structures much more feasible. It also allows the fabrication of very complex lattice structures, which can achieve lightweighting and other derived properties. Thus, lattice structures in AM are one of the most researched topics these days.

Non-stochastic lattice structures are repeating patterns of a unit cell, and they can either conform to a surface or fill a volume. They are inspired by biological lattice structures like the honeycomb of a beehive or bones. Moreover, these structures, at the main scale, have been used by engineers for decades. For example, the Eiffel Tower or sandwiched panels of airplane wings designs have these optimized beam or strut based structures. Their remarkable structural properties are owed by the unit cell. A unit cell is the fundamental building block of any lattice structure. These unit cells are arranged in an order known as a cell map that can be cylindrical, rectangular, spherical, or wrapped between two sinusoidal surfaces. Thus, the properties of the lattice structures are determined by the basic dimensions of the unit cell. For example, the size of the unit cell, the type of struts used to construct the unit cell, the thickness of the struts or surfaces and the orientation of

the struts and surfaces relative to each other are important factors to consider in the design and optimization of these structures [8].

3D lattice structures studied in this research can be broadly classified into two categories, as depicted in Figure 1.2:

- a) Strut-based lattice structures consist of circular struts or rods varied by the parameters such as strut diameter, length, and orientation.
- b) A triply Periodic Minimal (TPMS) lattice structure is referred to as a surface-based lattice structure. They consist of surfaces governed by certain periodic equations.

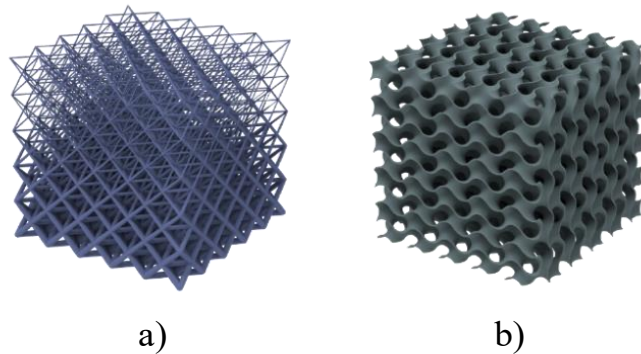


Figure 1.2: Non-Stochastic lattice structures – a) A strut-based lattice structure; b) A TPMS lattice structure (Gyroid) (Adapted from Varotsis [8])

The lattice structures listed above can be geometrically modelled in several different ways. The commonly used methods are:

1. They can be modelled using cylindrical struts, periodic surfaces (like TPMS) or plates.
2. They can be fit on a surface or can be used to fill a volume.
3. They can be trimmed to conform to a design space.
4. They can be generated via creating a mesh, a CAD model or modelled as an implicit body.

A more comprehensive representation of how designers can model lattice structures is pictorially represented by Varotsis [8] nTopology in Figure 1.3.

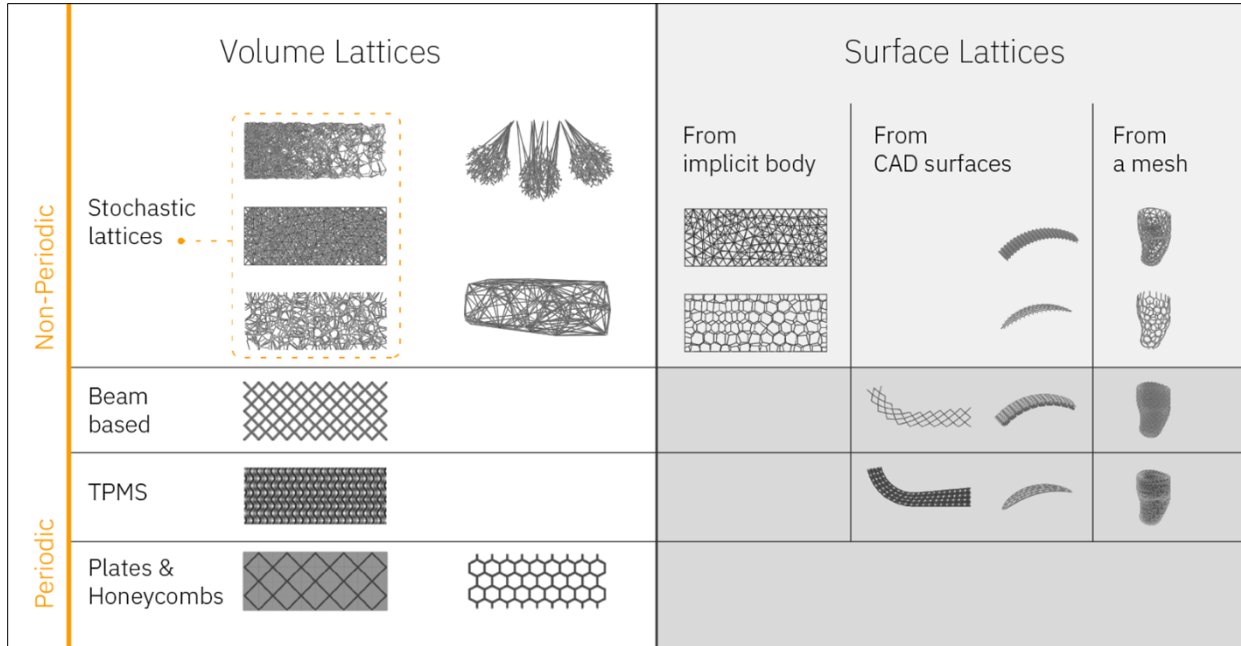


Figure 1.3 Lattice structures that can be generated in nTopology (Adapted from Varotsis [8])

The focus of this research is only on 3D lattice structures, and therefore the term “lattice structures” is used throughout this research thesis. As discussed, their properties usually depend on the type of unit cell chosen. Table 1.3 describes the key properties of lattice structures.

Table 1.3 Periodic Lattice Structures and their pros (Adapted from Varotsis [8])

Types of Periodic Lattice Structures	Properties that they Offer
Strut-based lattice structures	1. High Stiffness to weight ratio. 2. Good elasticity
TPMS lattice structures	Good Mechanical Properties
Honeycombs and Plates	High Stiffness

Other properties include good elongation and energy absorption, which can be achieved by varying the porosity of these structures to obtain desired weight for the product design. Along with the mechanical properties, the surface area of these structures can be used to improve the thermal and flow characteristics of the product.

In this research, the lattice Structures, as shown in Figures 1.4 and 1.5, are chosen to study the flow and thermal characteristics across them. These are selected based on literature survey, and

the basis of their selection and modelling methodologies are discussed in Section 3.1 of Chapter 3.

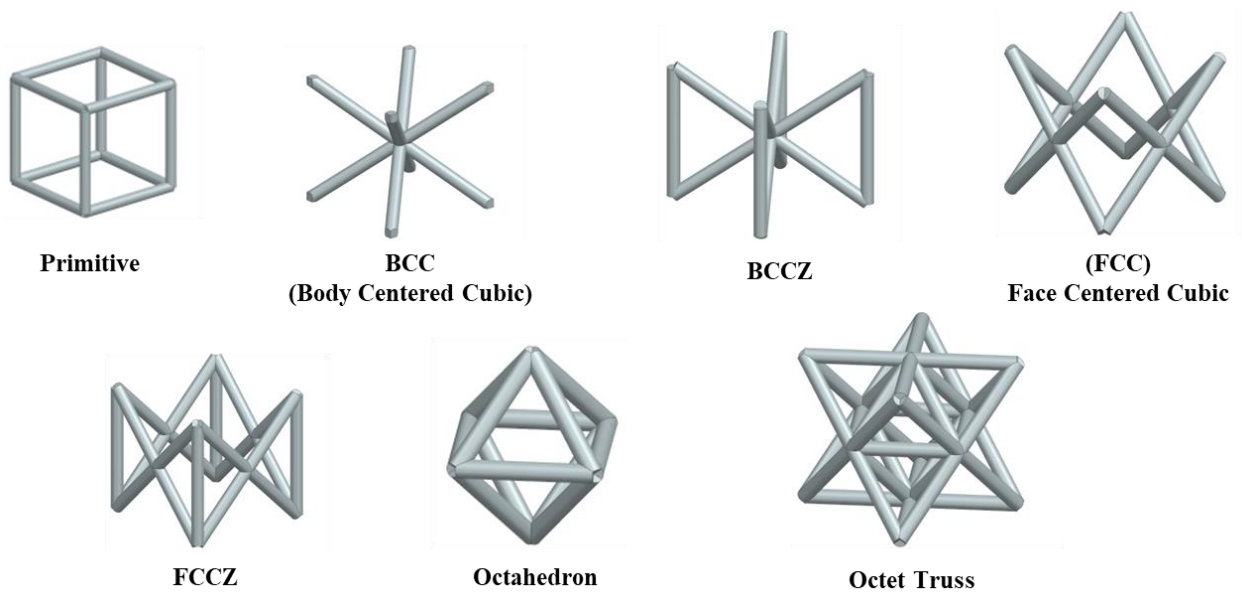


Figure 1.4 Strut-based Lattice Structures

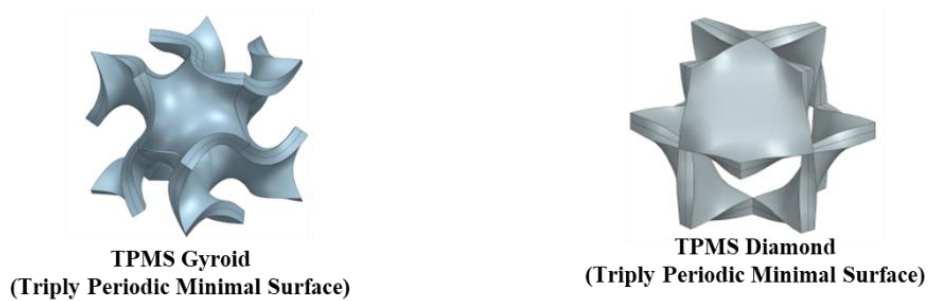


Figure 1.5 Surface-based Lattice Structures

### 1.3 Applications of Lattice Structures

As lattice structures can achieve specific desired properties and AM made the fabrication of these structures much easier, some of their important applications are below.

1. **Lightweighting:** Lattice structures can help aerospace industries to achieve lightweight designs. And design engineers choose lattice structures more often to reduce the material without compromising the performance of their parts. The most common approach to deploy

these requirements is by filling a design volume with a lattice structure. One of these approaches is shell and lattice infill, as depicted in Figure 1.6. This approach has resulted in 50% or higher weight reduction. Moreover, it also reduces manufacturing and raw material costs. And lastly, lightweighting not only adds to cost reduction but also gives highly resilient parts to damage [8].

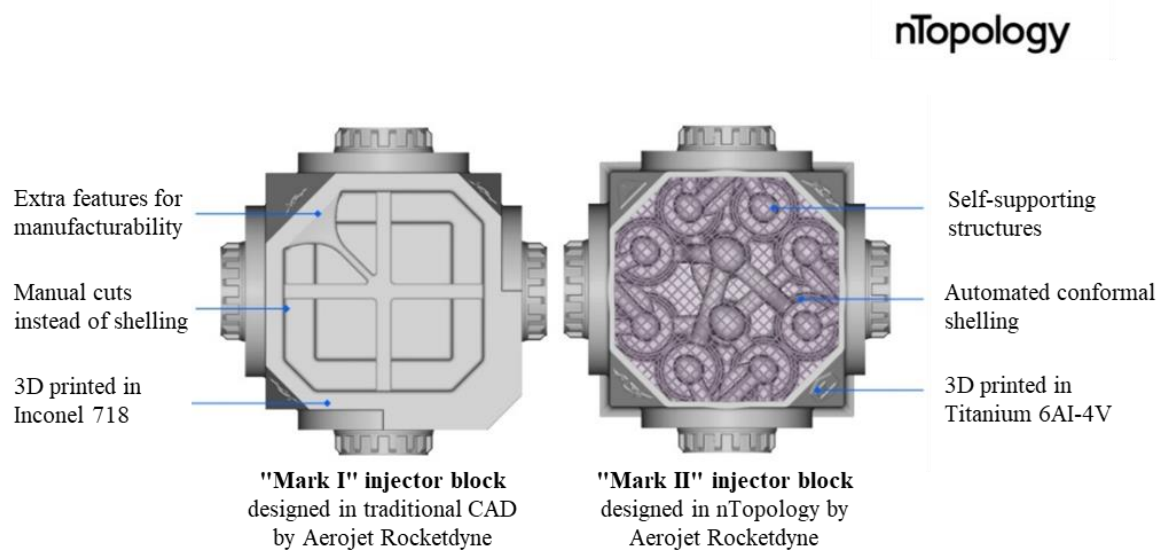


Figure 1.6 Aerojet Rocketdyne modelled using the "Shell and infill " technique [8]

2. Energy Absorption: Solid structures should absorb energy in any form, be it sound or impact energy. Thus, lattice structures are used for energy absorption in helmets, speakers, and headphones. In addition to that, they are good vibration dampers (Figure 1.7). This is possible due to their high porosity [8].



Figure 1.7 Riddell Speed flex helmet with its side lattice liners by Carbon 3D [9]

3. Thermal Management: Heat transfer rate is a function of surface area in contact, and lattice structures can provide high surface area. TPMS Diamond and Gyroid provide a larger surface

area for better convection and conduction. They have been used for heat exchanger applications (Figure 1.8) in the industries like automotive, aerospace, electronics etc. Furthermore, the Gyroid lattice structure has additional advantages allowing flow to be split into multiple channels providing a higher surface area to volume ratio for heat dissipation [8].

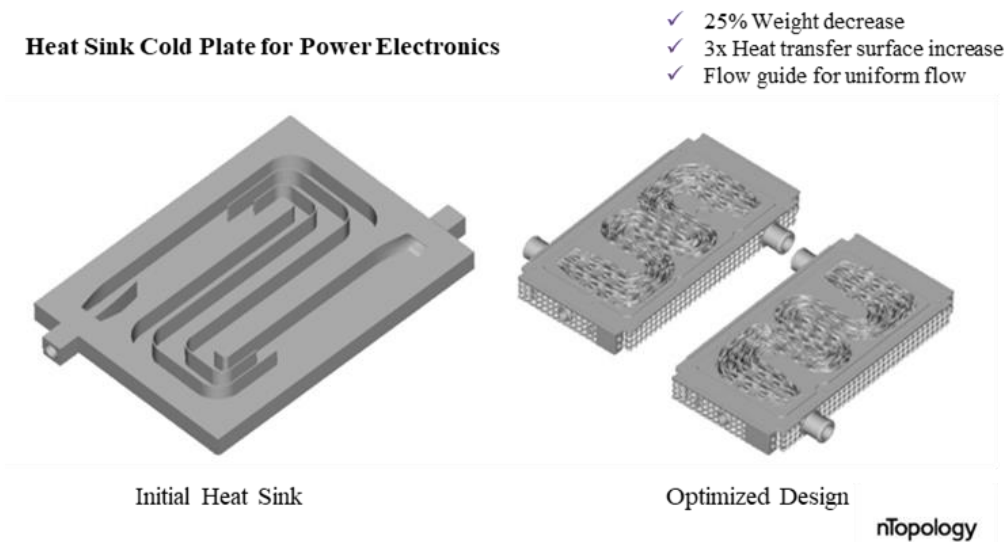


Figure 1.8 Cold plate in power electronics modelled using TPMS Gyroid [8]

## 1.4 Motivation of the Research

Previous sections explained the history of AM, types of lattice structures and their applications. Since AM-fabricated lattice structures are becoming more accessible, there is a lot of research and development testing the structural rigidity of lattice structures but very few on thermal and flow behaviour. And this research is sponsored by Siemens Energy with a focus on understanding the thermal and flow behaviour of highly compressed air across lattice structures to understand the potential of employing lattice structures in their products, such as gas turbine engines.

A typical gas turbine is shown in Figure 1.9, where it has three main mechanical systems:

1. Compressor: Compresses the atmospheric pressure to high pressure.
2. Combustor: Adds energy to the compressed air from the compressor to increase the temperature with minimal pressure loss.
3. Turbine: Produces shaft work output in the whole process.

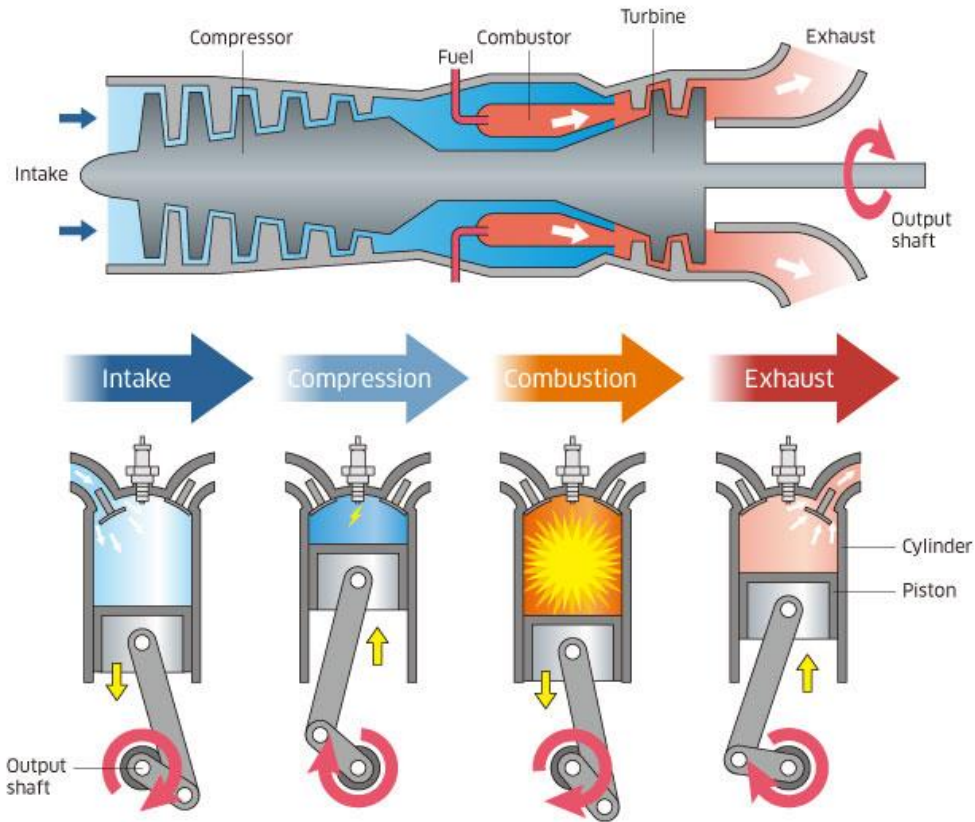


Figure 1.9 Gas Turbine representation by Kawasaki [10]

The flow from the combustor system is generally axial and must deviate at an angle of 90 degrees and should be divided around the eight pots, as shown in Figure 1.9. Thus, to ensure that this transition is smooth, structures like foams are provided to remove high turbulence and homogenize the flow direction in high temperature and vibrational environments. This is possible as the foam will slow down the flow, which in turn helps it to settle down equally in the pots, and some of the transient pulsating behaviour is also lost.

So far, the optimized geometry of the architected structures like foam and lattice structures for properties like pressure drop and vorticity change is never selected or calculated. Since lattice structures like TPMS Gyroid and Octet Truss provide large surface area for the convection of heat, along with helping to dampen the vibrations, they have high potential in these applications. Thus, having a flow and thermal property chart similar to material property charts such as Ashby charts shown in Figure 1.10 to correlate lattice structures and their flow and thermal properties is of high research value.

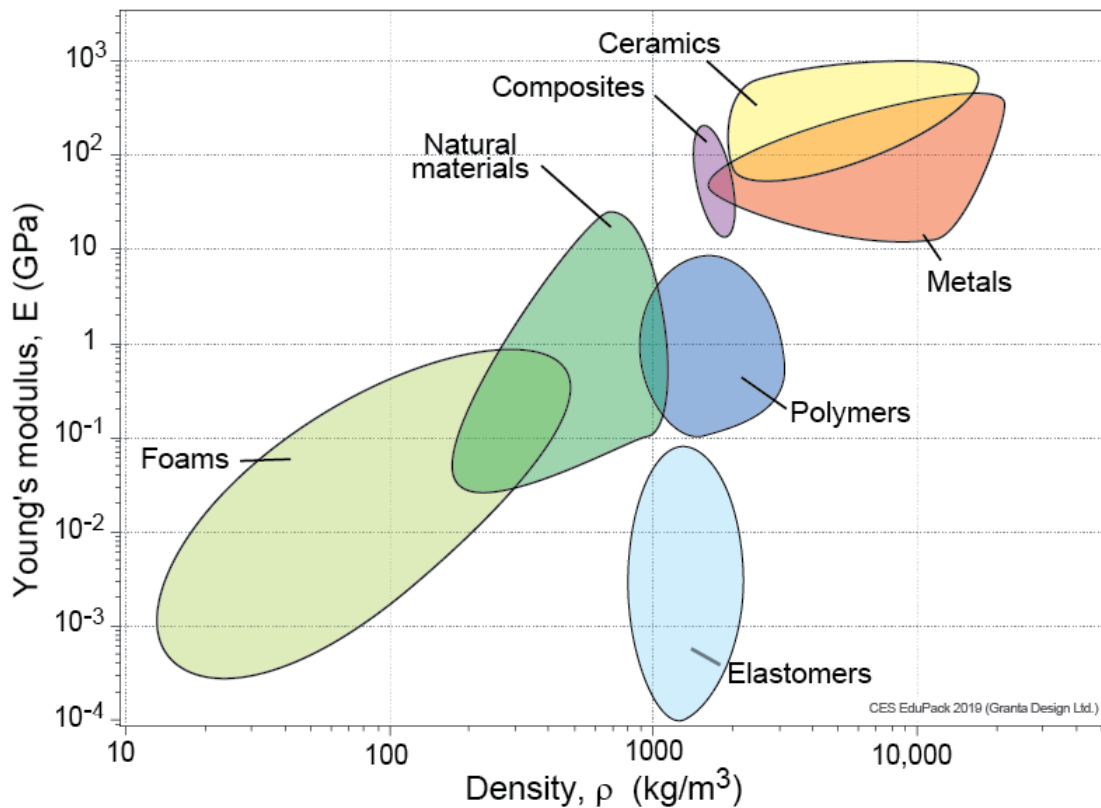


Figure 1.10 Material Property chart by Mike Ashby [11]

## 1.5 Problem Statement and Roadmap of the Thesis

The objectives of this research are:

1. To establish effective geometric modelling methods for the generation of a comprehensive list of lattice structures.
2. To develop surface repair and mesh convergence strategy for the effective computational fluid dynamics (CFD) simulation of the chosen lattice structures.
3. To identify flow and thermal characteristics to generate a property chart.

To achieve the objectives mentioned above, this thesis follows the roadmap shown in Figure 1.11.

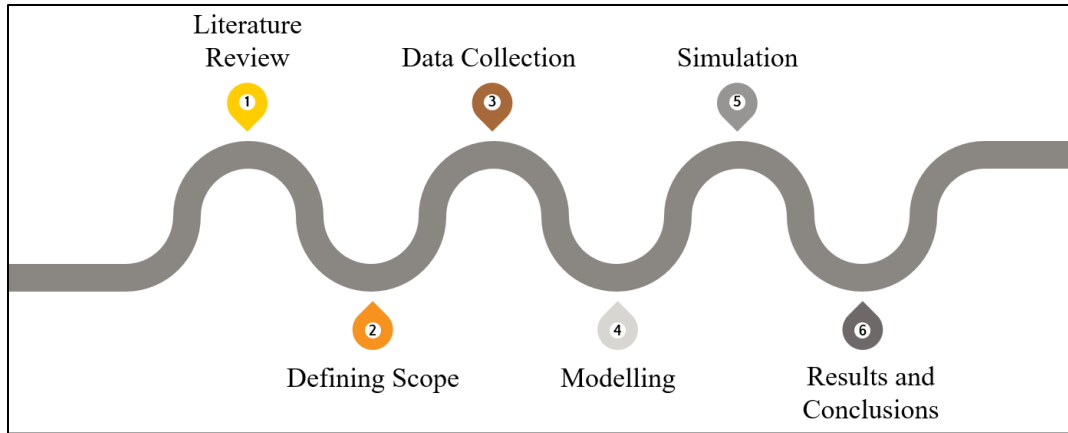


Figure 1.11 Research Roadmap

The purpose of the literature review (Chapter 2) is to collect data for different lattice structures existing across industries, along with their dimensions, types, and modelling techniques. Thereafter, the gap would be identified to make the scope of this research more specific.

Data analysis for obtaining the approximate dimensions to model the identified lattice structures from the literature is done in Chapter 3. Moreover, a stepwise implementation of methods is discussed in the same chapter to explain the methods used to model lattice structures geometrically. Methods for repairing the modelled structures to transfer them to the simulation environment and methods used for CFD simulation are also explained in Chapter 3.

The results obtained from the implementation of the methods are presented and discussed in Chapter 4: , along with the representation of the flow and thermal property charts. And finally, these discussions are summarized in Chapter 5: along with the possible future scope.

## Chapter 2: Literature Review

The purpose of the literature review in this research is to identify relevant research works which have mechanical, thermal and flow performance data of lattice structures. Ashby and Gibson are well known for the development of mathematical analogies and formulas for lattice structures. Their extensive work [12] shows that the following factors influence the mechanical and thermal properties of a lattice structure:

1. Material of the structure
2. Unit Cell topology
3. Relative density of the structure

According to Ashby [12], a unit cell of a lattice structure is of a few millimetres or micrometres. Thus, this allows “lattices” to be viewed both as materials and as structures. Therefore, a lattice should not only be considered as a network of struts or beams but also as monolithic material. However, this research is based on the structural behaviour of lattices, but the literature review covers their material-like behaviour as well. Therefore, the term “lattice structure” is used throughout this research thesis to refer to all the 3D “lattices.”

### 2.1 Mechanical Performance of Lattice Structures

Generally, lattice structures are of two types: 1. bending-dominated structures and 2. stretch-dominated structures. Bending-dominated structures are usually composed of joints with low connectivity at the joints. Whereas stretch dominated is typically composed of triangulated lattice structure unit cells, as shown in Figure 2.1.

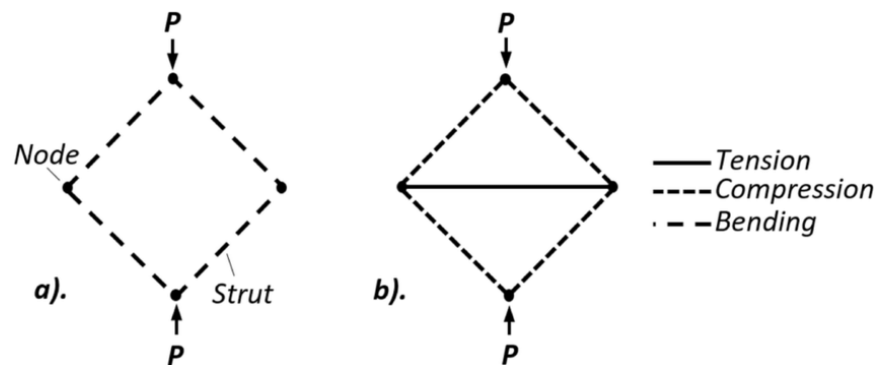


Figure 2.1 a) Bending dominated , b) Stretch dominated structure [13]

Here P is the applied force. As clear from the figure above, the members of the first figure are under bending due to the bending moment induced due to P. Thus, they are bending-dominated. Whereas in the second figure, the members are more under compressive and tensile loads due to the extra member introduced. Thus, they are stretch dominated. Maxwell’s stability rule can explain this concept and can be expressed as:

$$M = b - 3j + 6 = s - m \quad (2.1)$$

The above condition is for the pin-joint frame where b is the number of struts, j is the number of frictionless joints, s is the number of states of self-stress, and m is the number of mechanisms. If,

1.  $M < 0$  as in the case of Figure 2.2 a), then the frame has one or more than one degree of freedom; thus, it is a mechanism, i.e., the term “m” has some quantity. This also implies that this frame has no stiffness. The members or struts will surely bend under the load. This behaviour is shown by bending-dominated structures
2.  $M = 0$  as in the case of Figure 2.2 b), then the frame has stiffness and strength. Thus, the structure will carry tension or compression in the struts. And it is known to be both statically and kinematically determinate. This behaviour is shown by stretch-dominated structures, and they are “*just-rigid frameworks.*”
3.  $M > 0$  in Figure 2.2 c) signifies the fact that the extra member carries the compressive load from other members. Thus, it is always under compression even if the load applied is 0. This is called the concept of self-stress.

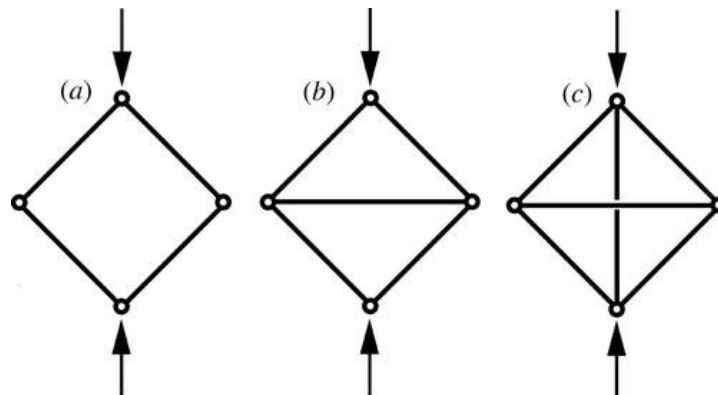


Figure 2.2 a) Bending-dominated structure, b) Stretch-dominated structure, c) Over-constrained or state of self-stress [12]

As the research progressed from the framework of Ashby [12], several different lattice structure architectures were studied. One of them is based on the concept of triply periodic minimal surface (TPMS). The surfaces of these structures are governed by certain periodic equations. Schwarz [14] first introduced the concept of TPMS Diamond in the 19<sup>th</sup> century. Their properties might differ from those of strut-based lattice structures, but their relative densities  $\rho$  can be the basis of comparison, which can be expressed as: It is as described in the following equation:

$$\rho = \frac{\bar{\rho}}{\rho_s} = \frac{V_L}{V_S} \quad (2.2)$$

where,  $\bar{\rho}$  is the density of the lattice structure core with volume  $V_L$  and  $\rho_s$  is the density of the solid core of the volume  $V_S$ . The mass is the same for both the lattice structure and the solid core. Since lattice structures are popular due to their light weighting property, it is very important to investigate that how much porous they are. Thus, another property known as porosity must be investigated. It is the ratio of void volume to the total volume occupied by the structure. It is generally a function of strut diameter or thickness, strut length and the volume of the space occupied. The porosity of lattice structures can be represented by:

$$\phi = (1 - \rho) * 100 \quad (2.3)$$

Since the material of the lattice structures is not within the research scope, this property compares them structurally.

### 2.1.1 Compressive Performance of Lattice Structures

There are three stages of deformation of lattice structures, as can be seen in Figure 2.3: Linear elastic deformation which ends at the onset of plasticity and is caused due to bending of the struts. Plastic deformation, where the curve shows the plateau behaviour and is caused by a progressive collapse of the struts, and densification, where the stress increases suddenly due to the intrusion of struts against each other [15]. And according to Ashby [12], the members of a lattice structure undergo three reasons for failure under compression: Buckling, yielding and fracture. The comparison of bending-dominated and stretch-dominated lattice structures for different failures can be seen in Figure 2.4, where

1. the bending-dominated lattice structures continue to deform under a constant state of stress. In contrast, stretch-dominated structures require oscillating stress for further deformation after yielding or buckling. This stress is referred to as Plateau stress.
2. during the densification, a lattice structure undergoes three failure modes: cell collapse, crack propagation and diagonal shear [16]. About 50% of the strength is lost at this stage.

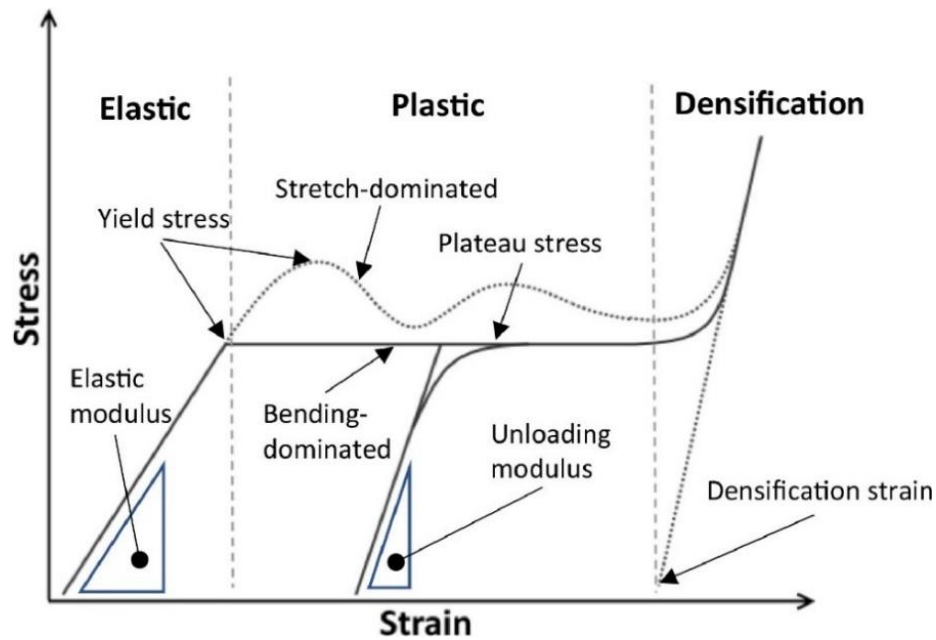


Figure 2.3 Comparison of bending-dominated and stretch-dominated structures [17]

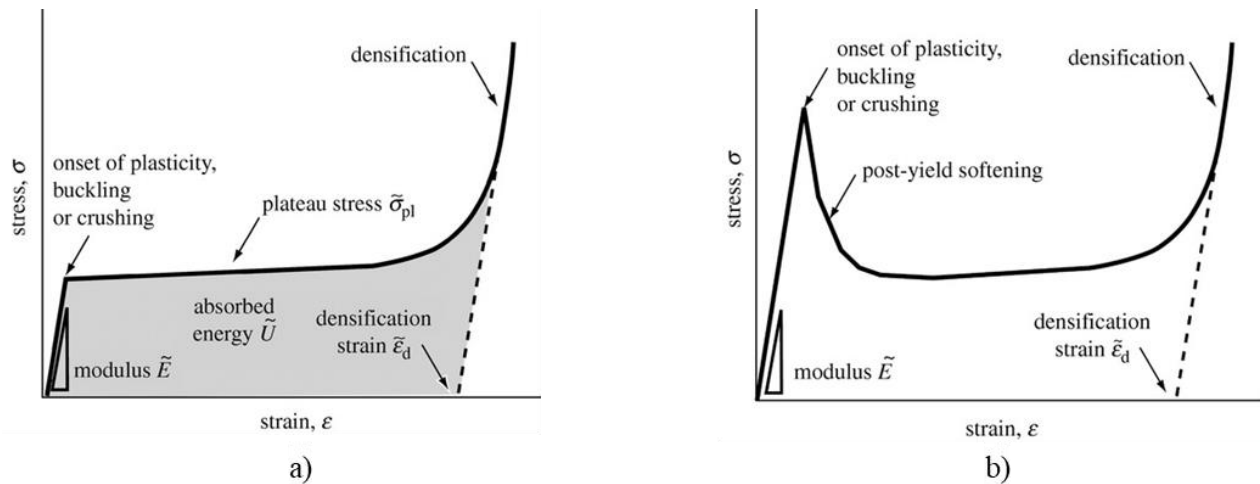


Figure 2.4 Separate stress-strain diagrams of a) Bending-dominated lattice structures, b) Stretch-dominated lattice structures [12]

Thus, stretch-dominated lattice structures are more weight efficient but not good at withstanding sudden failures, whereas bending-dominated lattice structures have a prominent transition toward failure [18]. It is found that stretch-dominated lattice structures fail layer by layer post-yield softening [19, 20]. Since material specifications are not taken into consideration here, cell topologies play a vital role in determining the strength and failure properties of these structures.

Furthermore, according to a research by Leary, Mazur [21], compressive strength decreases with the increase of unit cell size when porosity is kept constant. Simple topologies like BCC and FCC are bending-dominated structures following a trend as depicted in Figure 2.4 a). However, when these topologies are reinforced with some extra struts (z-struts), as shown in Figure 2.5, they become stretch-dominated structures (Figure 2.6).

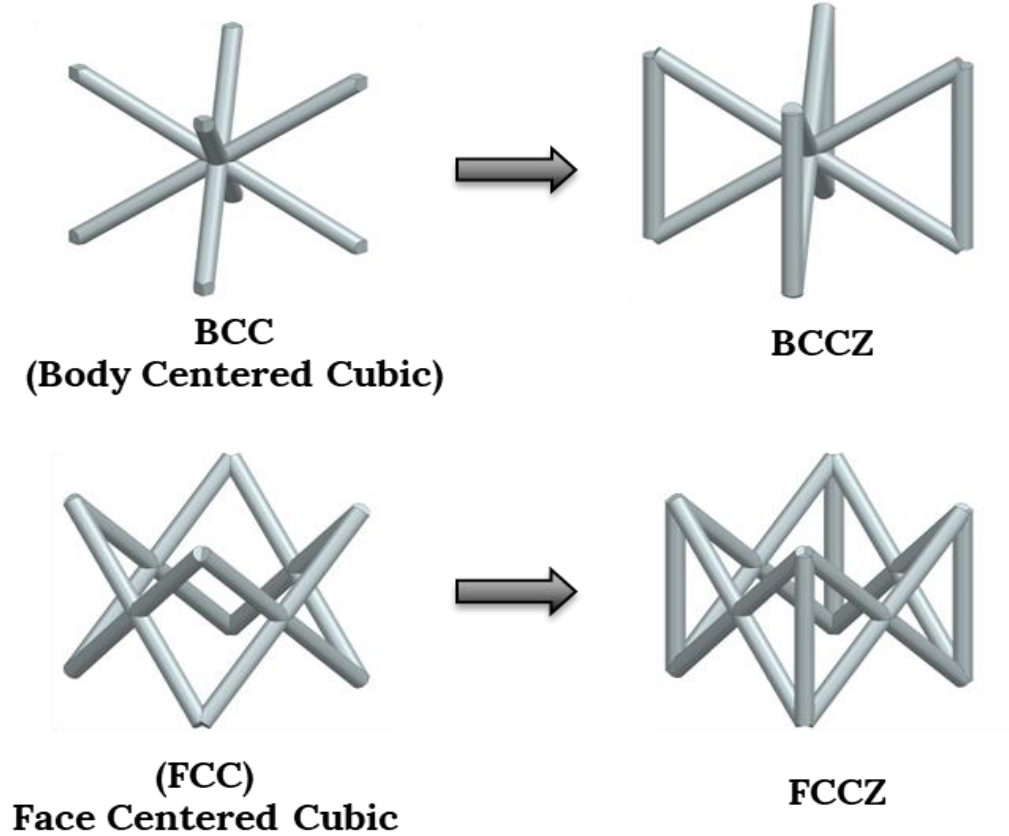


Figure 2.5 Converting bending dominated to stretch-dominated lattice structures

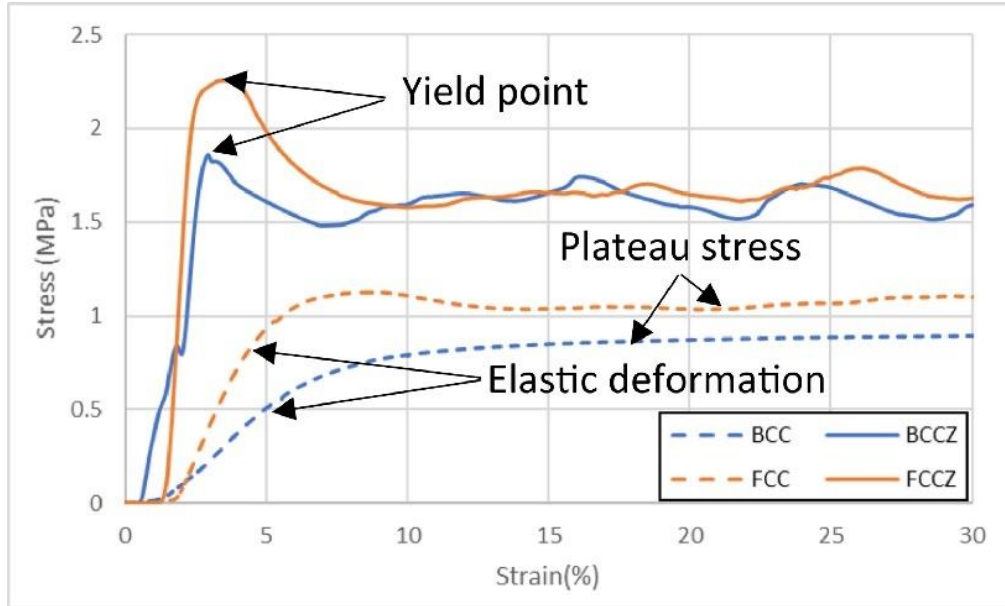


Figure 2.6 Stress-strain curve comparison for BCC(Z) and FCC(Z) lattice structure topologies [21]

Studies by [22] and [23] show that the direction of the struts has a great impact on the mechanical properties of the lattice structures. Horizontally built parts differ from the vertically built parts inside a lattice structure. The latter is prone to buckling, while the former is to both crushing and buckling. It has also been seen that the number of layers inside a lattice structure can also affect the deformation and energy absorption capacity of these structures [24]. They concluded that the total absorbed energy and strength increase when the lattice structure layers increase during the fabrication process.

Figure 2.7 shows the essential parameters of a unit cell governing the mechanical performance of lattice structures.

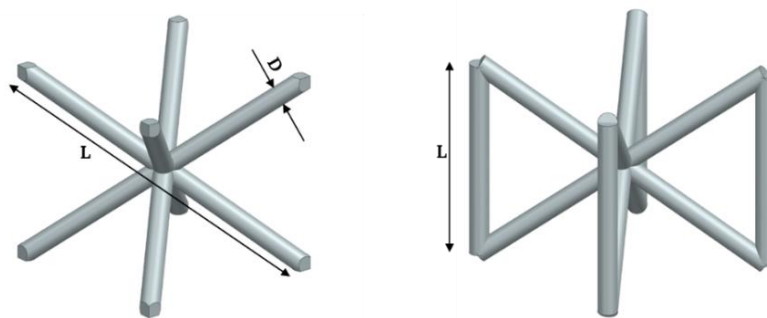


Figure 2.7 Unit Cell of BCC and BCCZ, when  $L =$  Strut Length,  $D =$  Strut Diameter

Also, it should be noted that buckling and crushing depend on the struts' slenderness ratio (Length to diameter ratio) of the strut.

A similar result was demonstrated by Xue, Wang [25], where it was seen that the longer the strut length ( $L$ ) is, the lower the compressive strength of these structures becomes, and the same goes with their elastic modulus. Their main area of investigation was auxetic lattice structures, and a graphical representation of the stress-strain curve for different re-entrant strut lengths can be seen in Figure 2.8. They also investigated the effect on Poisson's ratio of auxetic structures. It was found that the absolute value of Poisson's ratio increases with an increase in strut length.

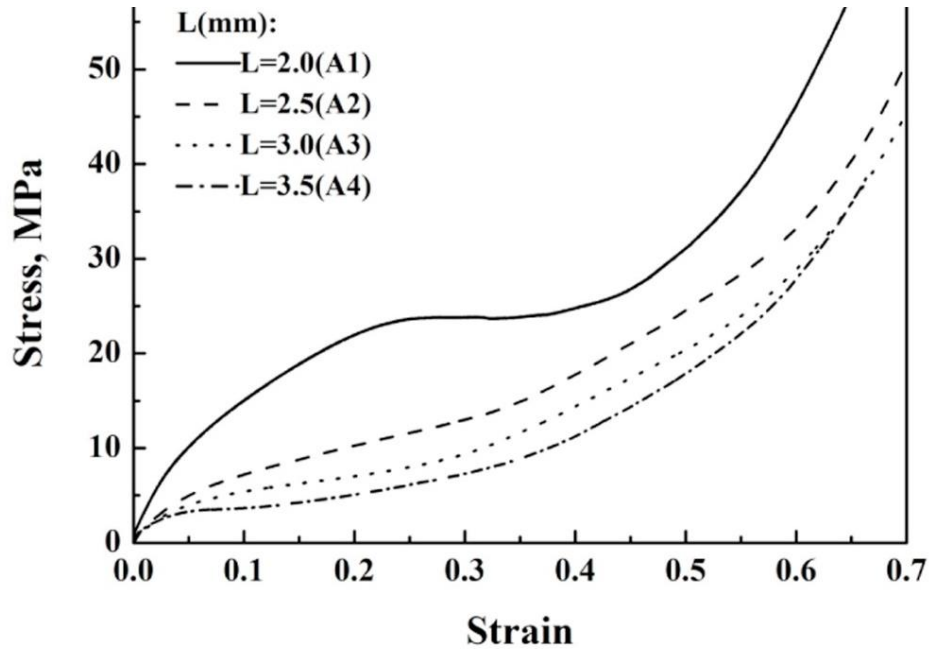


Figure 2.8 Stress-strain curves of lattice structures with different strut lengths  $L$  under compression [25]

As far as strut diameter is considered, it was seen that increasing its value from 0.6mm to 1.2 mm, increased the compressive strength of these structures by more than ten times (Figure 2.9) [26]. In addition to apparent density, strut diameter and strut length, the angle of the strut also play an important role in determining the mechanical performance of these structures.

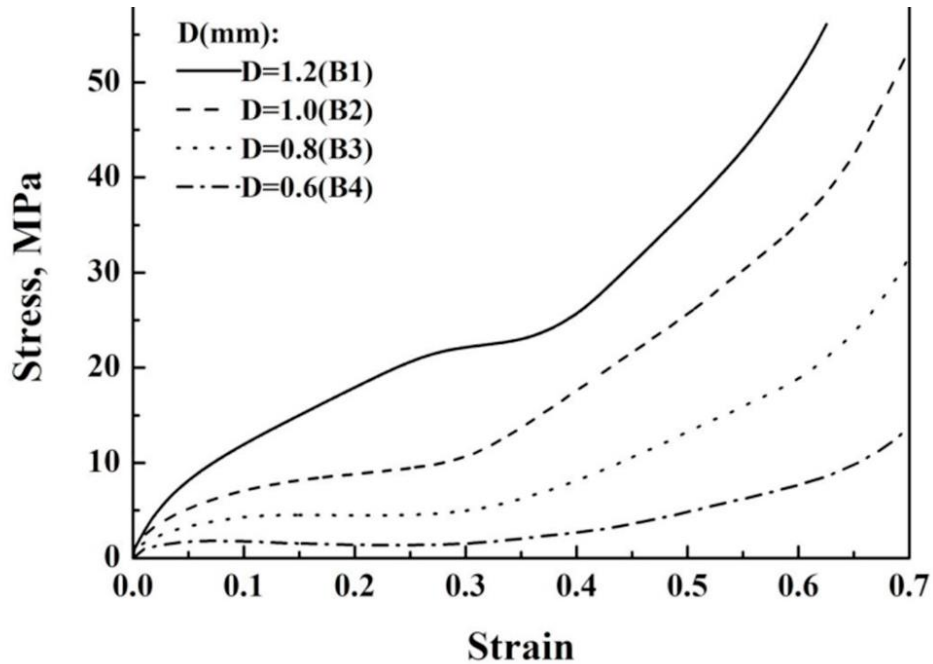


Figure 2.9 Stress-strain curves of lattice structures with different strut diameters  $D$  under compression [25]

### 2.1.2 Fatigue Performance of Lattice Structures

Fatigue Performance is a vital parameter to judge the performance of the components, especially those that are subjected to cyclic loading [27]. The stages of fatigue behaviour under cyclic loading can be broken down into three categories:

1. The strain increases rapidly or accumulation of strain, known as Cyclic Ratcheting [28].
2. Strain remains approximately constant for  $10^4$  to  $10^6$  cycles
3. The exponential increase in the strain leading to fatigue failure [27].

The porosity of the structure, the topology adopted, and the geometry of the strut significantly affects the fatigue performance of lattice structures. The material property also plays an important role, but its effect on fatigue performance is out of this research scope. Cyclic ratcheting depends on the cell topology and local geometry of the cell [29] [30]. It was found that topologies like Diamond and truncated cuboctahedron can sustain between  $1.5 \times 10^5$  and  $2 \times 10^5$  cycles, while topologies with cubic unit cells do not fail even after  $10^6$  cycles. Further, they found that the greater the relative density or lower the porosity is, the greater the load-bearing capacity becomes for the larger number of cycles (Figure 2.10 A). However, if the relative density remains the same, topologies play a vital role, as can be seen in Figure 2.10 B.

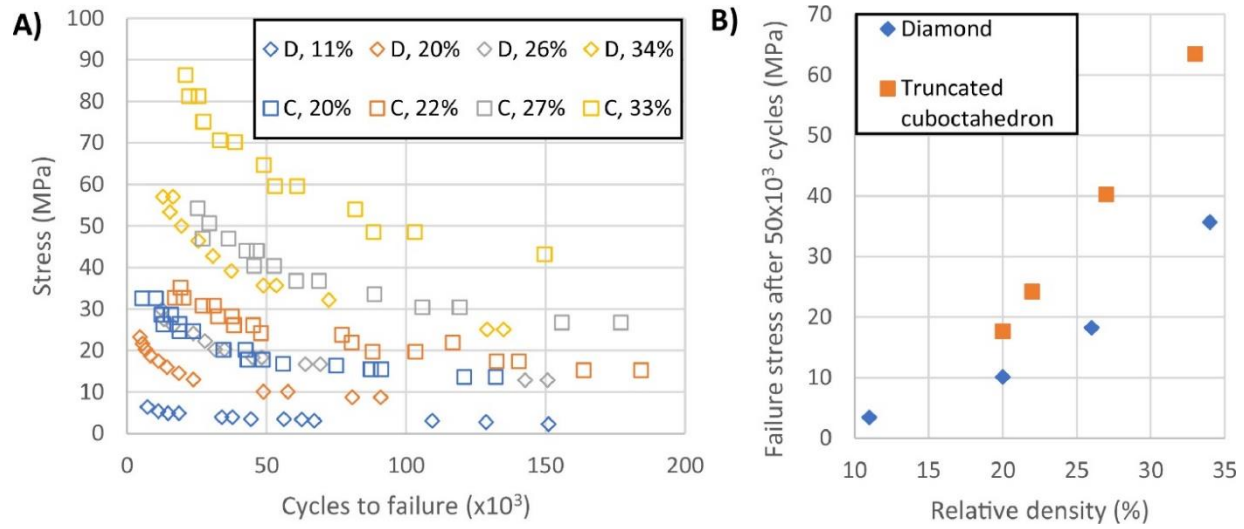


Figure 2.10 A: Fatigue performance of lattice structures with Diamond (D) and truncated cuboctahedron (C) topologies and varying relative densities (%). B: Failure stress after  $50 \times 10^3$  cycles and relative densities of these topologies [30].

Apart from cell topology and design, manufacturing defects also affect the performance of lattice structures. Numerous research has been done to identify these defects [27]. Defects like the staircase effect and porous defects during manufacturing significantly affect the fatigue strength of these structures [31]. Although these research findings are evidential that design parameters affect fatigue performance significantly, this area is still under investigation in the research industries to see a larger picture [32].

## 2.2 Heat Transfer Properties of Lattice Structures

Lattice structures showed good mechanical performances, but for their further evaluation, thermal properties should also be considered. However, no commercial solution to measure their thermal behaviour exists. Previously, researchers like Ashby had given formulations to judge their thermal performances. Reported research is more concentrated on their mechanical performance. Ashby [12] stated that convection is usually suppressed within these structures due to their small dimensions. However, heat transfer through them is the sum of heat conducted through their struts and that through the air. He gave the following formula for conductivity through these cells:

$$\bar{\lambda} = \frac{1}{3} \left( \frac{\bar{\rho}}{\rho_s} \right) \lambda_s + \left( 1 - \left( \frac{\bar{\rho}}{\rho_s} \right) \right) \lambda_g \quad (2.4)$$

The first term in the above equation for the conduction through solid struts (solid conductivity,  $\lambda_s$ ) and surfaces, while the second one is for the conduction within the gases ( $\lambda_g$ ). There is only very little numerical and experimental research that investigated heat transfer and flow properties of lattice structures. Most repeated research on this topic is focused on micro heat exchangers, as shown in Figure 2.11. These heat exchangers with lattice structures are shown to have exceptional heat transfer capacity.

1. Narkhede and Sur [33] demonstrated the thermal characteristics of the Octahedral lattice structure numerically. They carried out the study on ANSYS Fluent to calculate the variation of Nusselt Number with different Reynold's numbers for laminar flow. The heat transfer coefficient was in the range of 2201 to 3235 W/m<sup>2</sup>K.
2. Calmidi and Mahajan [34] performed both numerical and experimental studies to study forced convection behaviour in high porosity metal foams. For a very low Reynold's number, they obtained Nusselt's number between 10 and 11.
3. Lu [35] carried out a heat transfer study on metal honeycombs for different Reynold's numbers and obtained a convective heat transfer coefficient between 1000-4000 W/m<sup>2</sup>K for air cooling. Also, the pressure loss across these structures was found to be very small.

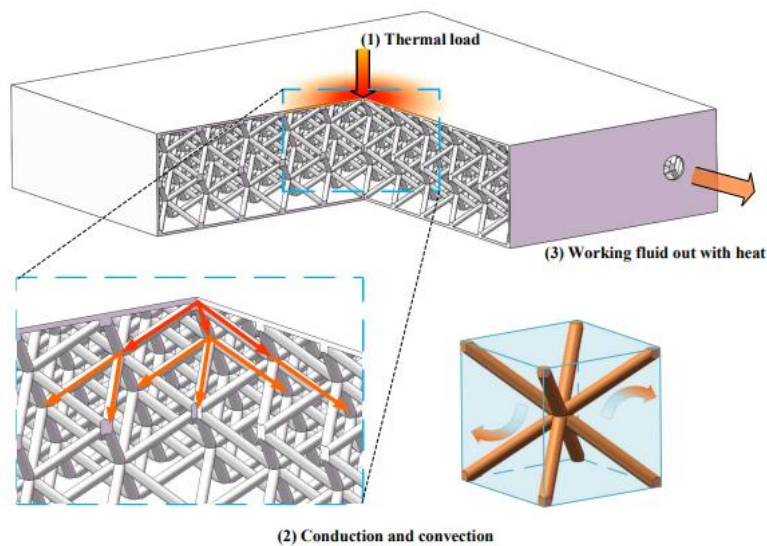


Figure 2.11 Working process of a heat exchanger with lattice structure [36]

All these studies have worked around the output properties discussed in the following sections to compare different lattice structures.

### 2.2.1 Heat Transfer Coefficient

Mathematically, the heat transfer coefficient is the ratio of heat flux to the change in temperature and can be calculated by the following formula:

$$U_0 = \frac{\dot{Q}}{A\Delta T} \quad (2.5)$$

Where,  $U_0$  is the overall heat transfer coefficient in  $W/m^2 \cdot K$ ;  $\dot{Q}$  is the rate of heat transfer in  $W$ ;  $A$  is the overall heat transfer in  $m^2$  and  $\Delta T$  is the overall temperature difference in Kelvin. The higher the value of the heat transfer coefficient is, the higher the heat transfer rate becomes. In this thesis, since the material is not considered for judging the heat transfer properties of lattice structures, only the convective heat transfer coefficient is taken into consideration which is:

$$h = \frac{\dot{Q}}{A\Delta T} \quad (2.6)$$

Where,  $h$  is the convective heat transfer coefficient in  $W/m^2 \cdot K$ ;  $\dot{Q}$  is the rate of heat transfer in  $W$ ;  $A$  is the overall heat transfer in  $m^2$  and  $\Delta T$  is the overall temperature difference in Kelvin. Lu, Stone [37] demonstrated that the heat transfer coefficient is also a function of fluid velocity  $v_f$  and open foam density  $\rho$  (Figure 2.12).

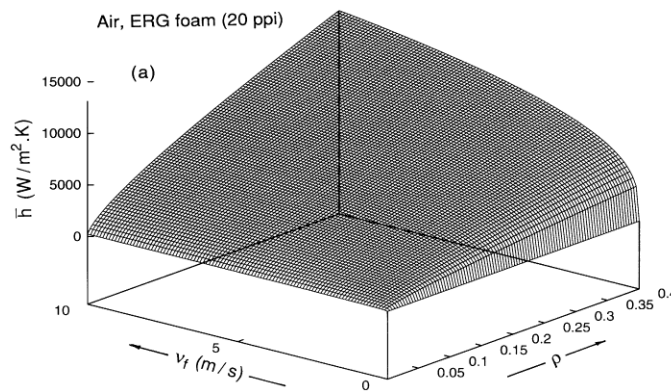
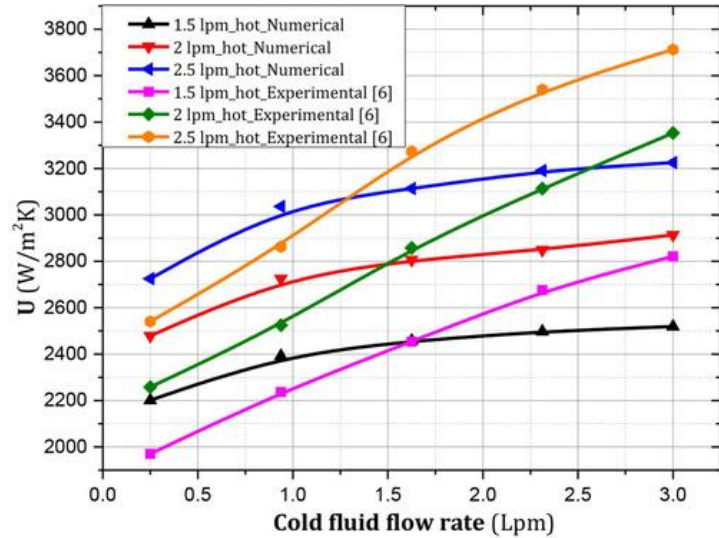


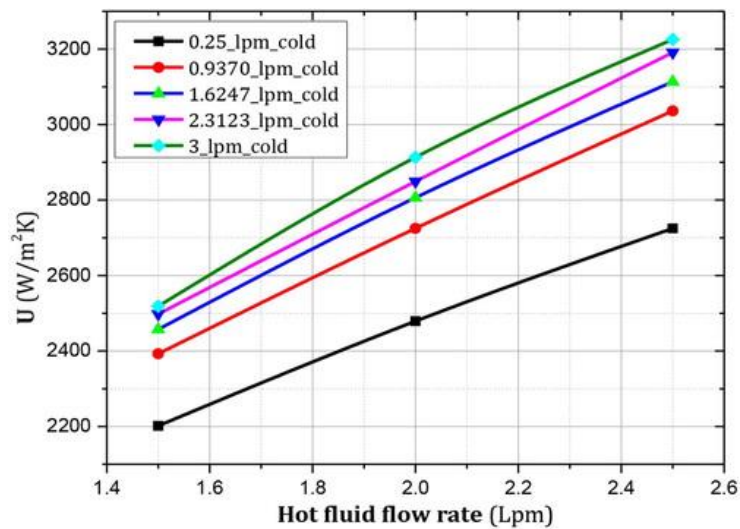
Figure 2.12 Overall heat transfer coefficient  $\bar{h}$  with varying fluid velocity and relative densities [37]

Narkhede and Sur [33] also showed that whether it is hot fluid or cold liquid, the trend and range of convective heat transfer coefficient is very high and follow the same trend with the mass flow rate of the fluid as well (Figure 2.13).

Thus, the heat transfer coefficient is a function of flow velocity, that is, Reynold's number of the flow. Furthermore, it also depends on the density of the lattice structure or the dimensional properties of the lattice structures.



a)



b)

Figure 2.13 Variation of overall HTC with a) cold fluid mass flow b) hot fluid mass flow [33]

### 2.2.2 Nusselt's Number

Nusselt's number,  $Nu$ , is the ratio of convective heat transfer to conductive heat transfer within the fluid.

$$Nu = \frac{hl}{k} \quad (2.7)$$

Where,  $k$  is the thermal conductivity of the fluid in  $W/m.K$ ;  $l$  is the characteristic length in meters and  $h$  is the convective heat transfer coefficient from equation 2.6. If its value is greater than one, then the heat transfer is predominantly by convection. Narkhede and Sur [33] found that Nusselt's number increases as Reynold's number is increased for octahedral lattice structure (Figure 2.14).

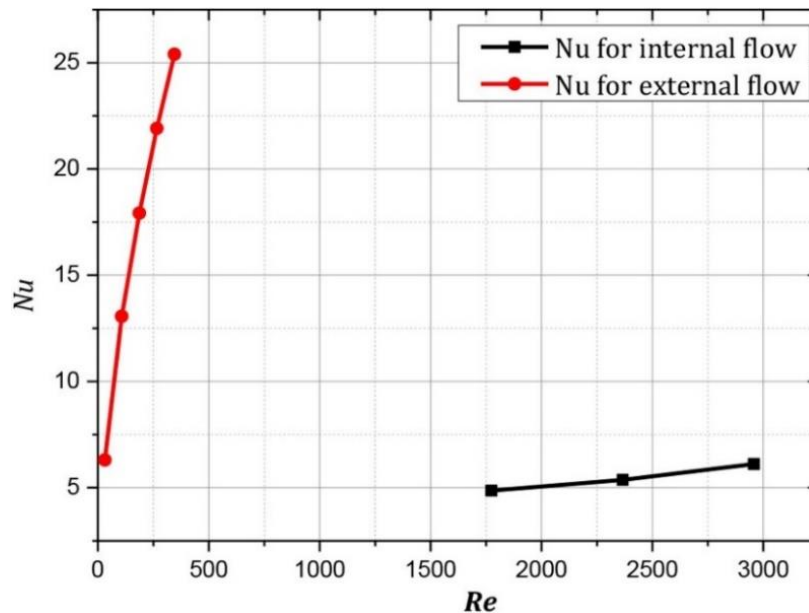


Figure 2.14 Nusselt number variation with Reynolds number for both internal and external pipe flow [33]

A very similar trend was observed by Kim, Zhao [38] and Calmidi and Mahajan [34] by analyzing the Nusselt Number variation for convective heat dissipation with aluminum lattice-frame materials. Another unit cell type called Rhombi-Octet was investigated by Ho, Leong [39] for different strut diameters and porosity (which are identified as L1, L2....) (Figure 2.15).

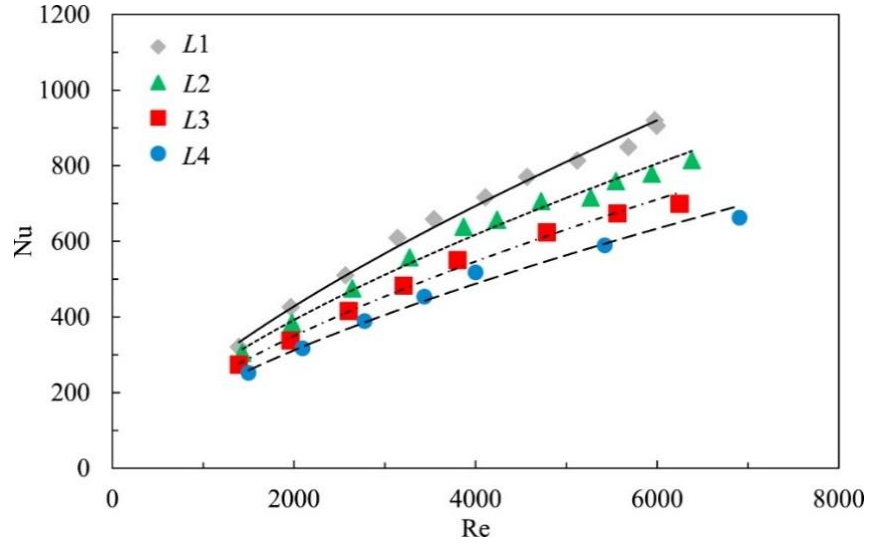


Figure 2.15 Nusselt's number variation at different Reynold's number for the Rhombi-Octet [39]

Thus, all these data show that the Nusselt number increases as one increases Reynold's number of any type of flow across lattice structures.

### 2.2.3 Friction Factor

As minimizing pressure losses is very important in the aerospace and automotive industries, the friction factor across the lattice structures is an important parameter to measure. Pressure loss by Darcy Weisbach equation is given as:

$$\Delta P = f \left( \frac{l}{d} \frac{\rho_f V^2}{2} \right) \quad (2.8)$$

Where,  $\Delta P$  is the pressure loss in  $N/m^2$ ;  $f$  is the Darcy friction factor;  $l$  is the characteristic length of the pipe in meters;  $d$  is the hydraulic diameter in meters;  $V$  is the mean flow velocity of the fluid in m/s and  $\rho_f$  is the fluid density in  $kg/m^3$ . The friction factor of lattice structures is generally compared with the friction factor,  $f_0$ , of a similar and hydraulically smooth channel given by the following correlations:

---


$$1. \quad \frac{f}{\sqrt{f_0}} = 1.8 \log \left( \frac{Re}{6.9} \right) ; \text{ for } Re = 5 \times 10^3 - 10^7, \text{ (Colerbrook, 1938)} \quad (2.9)$$

---


$$2. \quad f_0 = \frac{0.184}{(Re)^{0.2}} ; \text{ for } Re = 3 \times 10^4 - 10^6, \text{ (Kays and Perkins, 1985)} \quad (2.10)$$


---

---


$$3. f_0 = \frac{64}{Re}; \text{ for laminar flows} \quad (2.11)$$


---

These three properties are the focus of this research to investigate the flow and thermal performance of lattice structures. Researchers have calculated these parameters by varying different input parameters like strut diameter or thickness, strut length, relative density or porosity of the unit cell and Reynold's number of the fluid flowing across these structures. The ranges of these output flow and thermal properties reported in the literature are summarized in Table 2.1.

Table 2.1 Value ranges of flow and thermal properties of lattice structures from the literature

<b>Author</b>	<b>Property</b>	<b>Range of property</b>	<b>Input Parameter Range</b>	<b>Topology Type</b>
[38]	Nusselt's Number	100-1000	Reynold's Number 3000-35000	Fully triangulated, lightweight (porosity ~ 0.938), aluminum lattice-frame materials (LFMs)
	Friction Factor	0.1-1	Reynold's Number 100-3100	
[37]	Heat transfer coefficient	0-5000	Density of foam 0-0.4	Open cell foams with simple cubic unit cells
	Pressure Drop per unit length	0-100		
[35]	Heat transfer coefficient	1000-4000	Porosity 0-1	Honeycomb
[34]	Nusselt's Number	5-15	Reynold's Number 15-65	Metal Foams (Porosity=0.89-0.97)
[33]	Heat transfer coefficient	2000-3800	Fluid flow rate 1.4-2.6 Lpm	Octahedral Micro lattice structure (Porosity = 0.91)
	Nusselt Number	5-25	Reynold's Number 0-3000	

Author	Property	Range of property	Input Parameter Range	Topology Type
[39]	Nusselt Number	200-1000	Reynold's Number 1000-8000	Rhombi-Octet (unit cell size from 5mm to 12mm)
	Friction Factor and Darcy Number ( $f \cdot Da^{1/2}$ )	0.05-0.3		
[35]	Heat transfer coefficient	1000-4000	Reynold's Number <2000	Metal Honeycombs (porosity from 0-1)
[40]	Heat transfer coefficient	1000-2500	Mean velocity of fluid 0-0.06 m/s	Strut-based lattice structures

## 2.3 Analysis of the Data Reported in the Literature

The purpose of this section is to collect, filter and analyze the data from the literature for different lattice structure topologies.

### 2.3.1 Data Collection and Data Filtration

The data collected is appended in Appendix A. This contains a list of all the lattice structure topologies from the literature. This data is filtered to get

1. the frequency of the occurrence of different lattice structure topologies that are studied for their mechanical and thermal performances in the literature (Figure 2.16).
2. the industries for which these lattice structure topologies are studied (Figure 2.17).
3. the manufacturing method and material (Figures 2.18 and 2.19).

From Figure 2.16, it is found that BCC is the most researched lattice structure because they provide high stiffness after introducing z-struts with high porosity/relative density. And low porosity/relative density gives the maximum light weighting opportunity, which is a very important aspect.

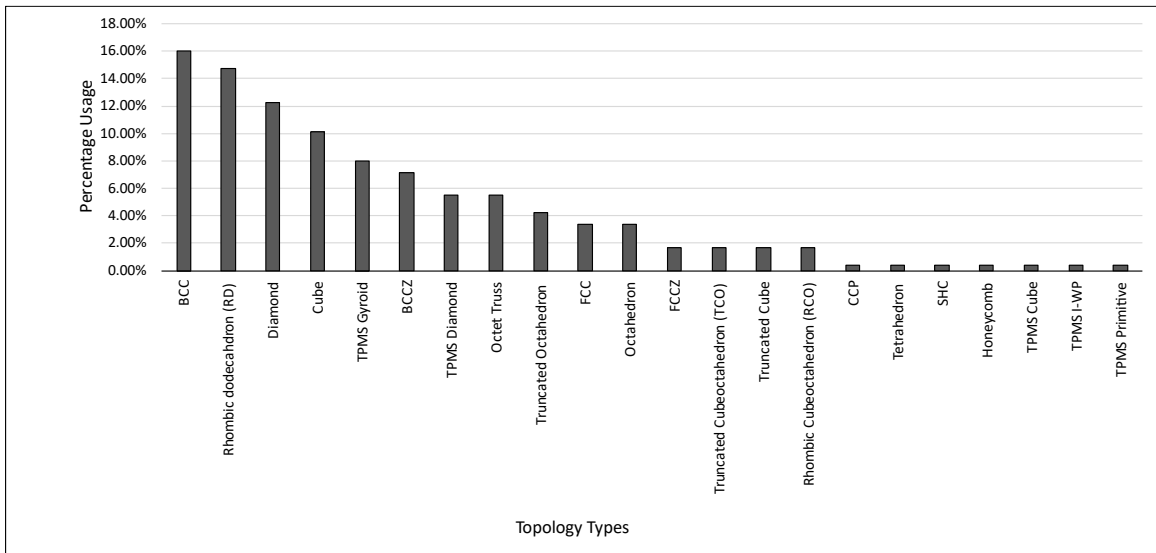


Figure 2.16 Percentage use of different topologies across the literature

It is also evident from Figure 2.17 that lattice structures are mostly used in the aerospace industries, followed by biomechanics. The field “not given” are for those research papers which have not specified the industries where the investigated lattice structure topologies are used. The top 90 percentile of the lattice structures were further selected from the above data to study their heat transfer and flow characteristics in this research. The modelling of these lattice structures is explained in the next chapter. These lattice structures include both struts-based and surface-based lattice structures. Both categories follow different geometric modelling techniques but the only property which connects them is their relative density/porosity.

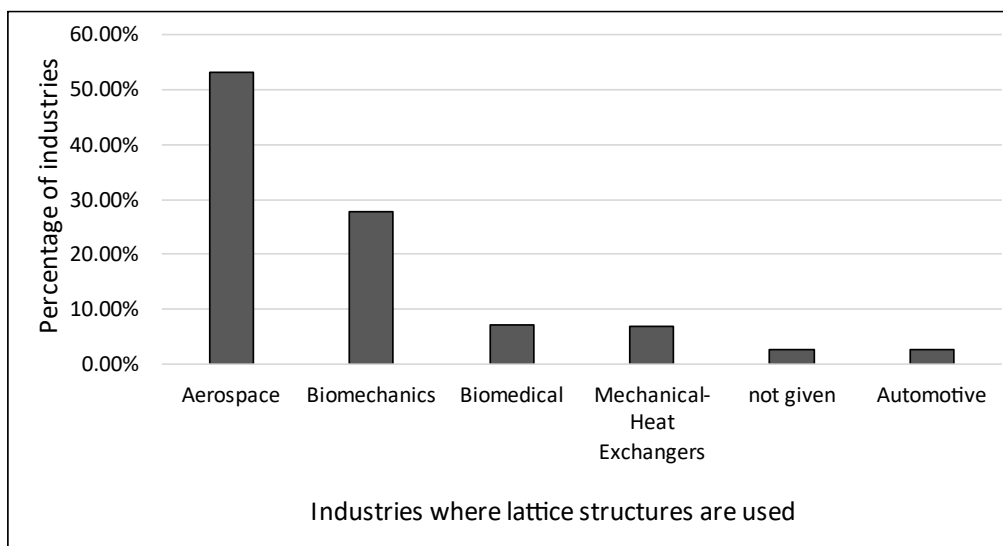


Figure 2.17 Industries using lattice structures

Figure 2.18 represents the percentage of different AM technologies used to manufacture these lattice structure topologies. It is evident that most industries use SLM to manufacture lattice structures. This is due to the reason that end products are stronger and have fewer voids/defects.

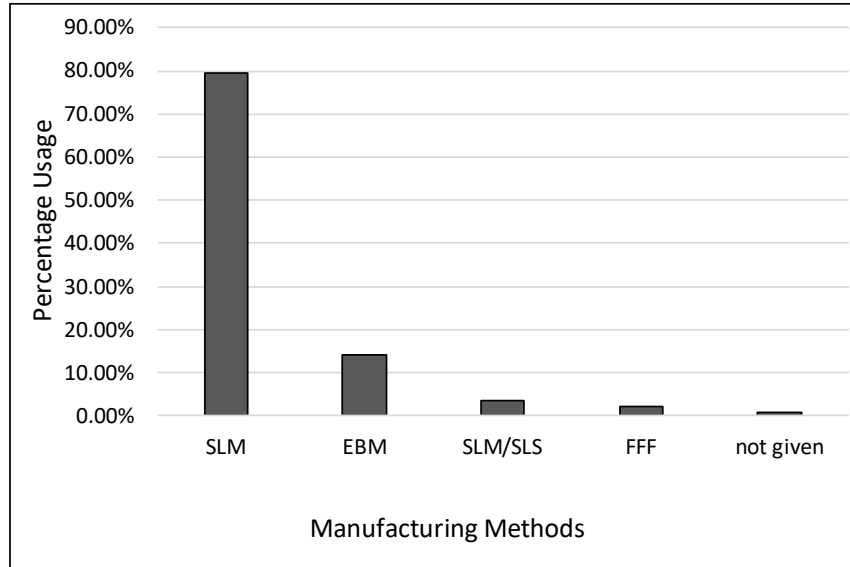


Figure 2.18 Percentage usage of manufacturing technologies in AM

The most common powder materials used in SLM include Steel, Titanium alloys and Nickel alloys, and Figure 2.19 also illustrates that Titanium-based alloys are the most investigated. This supports the fact that most aerospace industries are interested in such materials for light weighting their components.

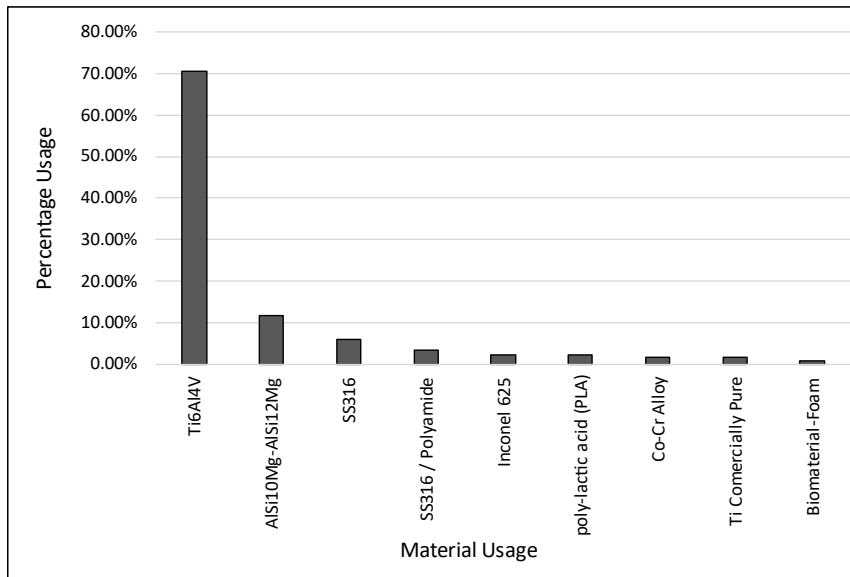


Figure 2.19 Percentage use of different materials in AM

### 2.3.2 Data Analysis

After data collection and filtration to identify suitable lattice structures to study, the next step involves deciding upon the dimensional parameters. These parameters are very important to model and structure the simulation. Thus, to get an idea of what dimensions should be used to model the structures, the data in the previous section was analyzed. All the dimensions were extracted from the data to get an average value of dimensions used to model the lattice structure geometry. Four major parameters are discovered:

1. Strut Diameter for the lattice structures, which have cylindrical beams.
2. Surface thickness for the surface-based lattice structures.
3. Strut length.
4. Porosity or relative density.

From Table 2.2, the average strut diameter or thickness lies between 1 – 2.5 mm, and the average strut length can be up to 2 mm (in some cases, 3.2 mm). Porosity depends on these dimensional parameters, but some reported research used the backwards approach, that is, to calculate the dimensions from the given porosity.

Table 2.2 Dimensional parameters

Type	Average Strut Diameter (mm)	Average Strut Thickness (mm)	Average Strut Length (mm)	Average Porosity/Relative Density
BCC	0.67		0.25	0.92
BCCZ	0.64			
CCP			0.50	0.77
Cube	1.88	0.80		0.92
Diamond	0.64			
FCC	0.64		0.60	0.46
FCCZ	0.50	0.80		
Honeycomb	1.20			0.84
Octahedron	0.20	4.02	0.80	
Octet Truss	2.46	0.38	0.55	
Rhombic Cuboctahedron (RCO)	0.28			
Rhombic dodecahedron (RD)	2.38	2.07	3.42	0.91
SHC			0.60	0.77
Tetrahedron		0.24		

Type	Average Strut Diameter (mm)	Average Strut Thickness (mm)	Average Strut Length (mm)	Average Porosity/Relative Density
TPMS Cube		0.90		
TPMS Diamond		0.71		0.43
TPMS Gyroid	0.80	0.74	1.80	
TPMS I-WP		0.25		0.44
TPMS Primitive		0.40		0.50
Truncated Cube	0.73			
Truncated Cuboctahedron (TCO)	0.33			
Truncated Octahedron	0.34			
Grand Total Average	<b>1.093571</b>	<b>1.368649</b>	<b>1.807632</b>	<b>0.872084</b>

Strut diameters are used when the lattice structure is strut-based, and thickness is used when it is surface-based, but some reported research considered the mapping between strut-based and surface-based lattice structures. For example, one can begin with the strut diameter and map that dimension to produce a TPMS Gyroid of equivalent thickness. This sometimes helps to compare these two different categories of lattice structures. The majority of reported research has used fixed unit cell size and filled the volume of lattice structure inside it. The geometric modelling aspects will be discussed in the next chapter.

## 2.4 Simulation Setup for Heat Transfer

All the reported research either used the experimental setup, analytical analysis, or numerical analysis to evaluate the flow and heat transfer characteristics. This research primarily focuses on carrying out computational fluid dynamics (CFD) simulations to investigate the flow and thermal properties of lattice structures. Softwares like ANSYS or StarCCM+ provide both numerical and analytical setups. However, it is seen that most of the reported research has not used CFD models, and the reason for this will be discussed in more detail in Section 2.5.1 .

There are three basic steps involved in conducting simulation using software:

1. Geometry Preparation
2. Discretization of the geometry (Figure 2.20)
3. Integrating the solution for all the discretized elements produced in step 2.

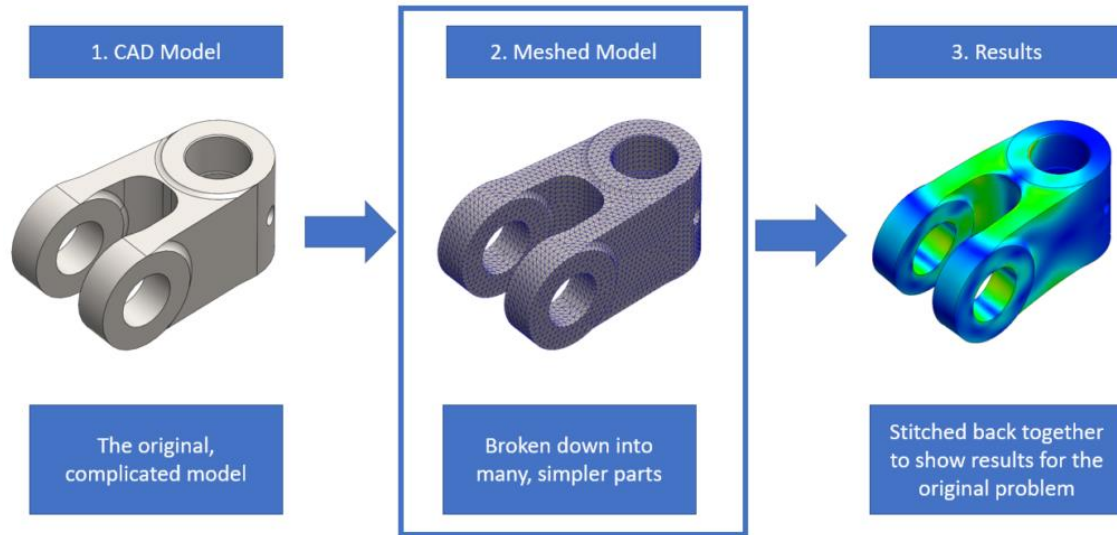


Figure 2.20 Finite element model process [41]

This whole process is referred to as the Finite Element Method. It involves both analytical as well as numerical approaches. Step 1 and Step 2 are purely analytical methods where the geometry is divided or discretized into the amount of nodes/surfaces/volume. This includes meshing and generation of shape function by stiffness matrix. The problem here is solved node-wise, like differentiating a function and then solving each node individually mathematically. Then at the simulation stage, the stiffness matrices for each node get converted into a single global stiffness matrix. This is done using numerical methods by the software.

### 2.4.1 Computational Flow Domain

A computational flow domain is very important while setting up the CFD simulation. It is the geometry in the space where the numerical analysis takes place. It is very similar to the experimental setup. The setup inside the simulation software is generally similar to the real-life experimental setup.

Lu, Stone [37] considered the steady-state flow through open foams sandwiched between two plates, as shown in Figure 2.21. Plates are of length  $L$  and width  $W$ . Furthermore, they chose a simple cubic unit cell. In their subsequent study on the heat transfer efficiency of metal honeycombs, a similar model was created (Figure 2.22) [35]. In experimental analysis, test rigs are set up to test the model for its thermal performance.

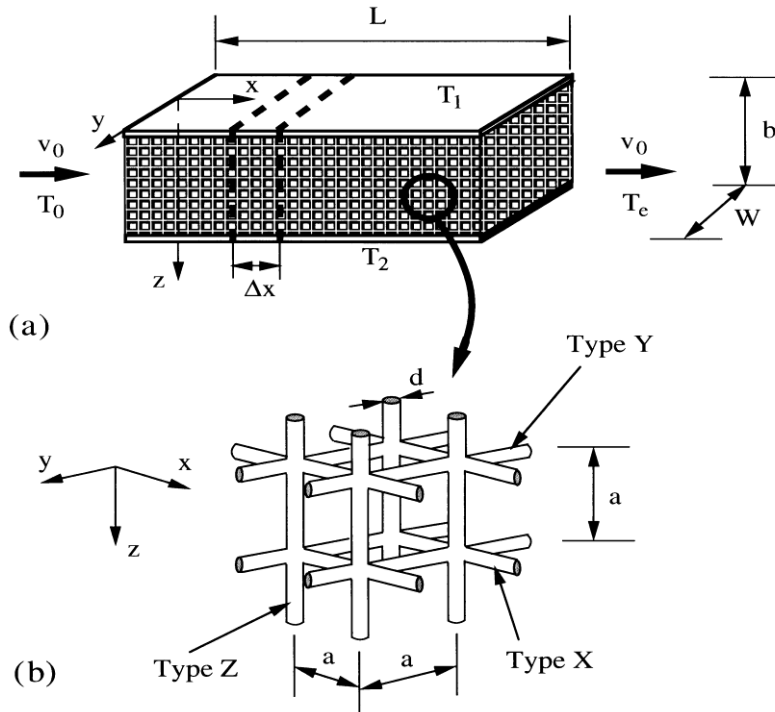


Figure 2.21 a) Experimental setup for open foams b) Lattice structure with cubic unit cell is used for the setup (the nomenclature used in this figure is different from the rest of the thesis) [37]

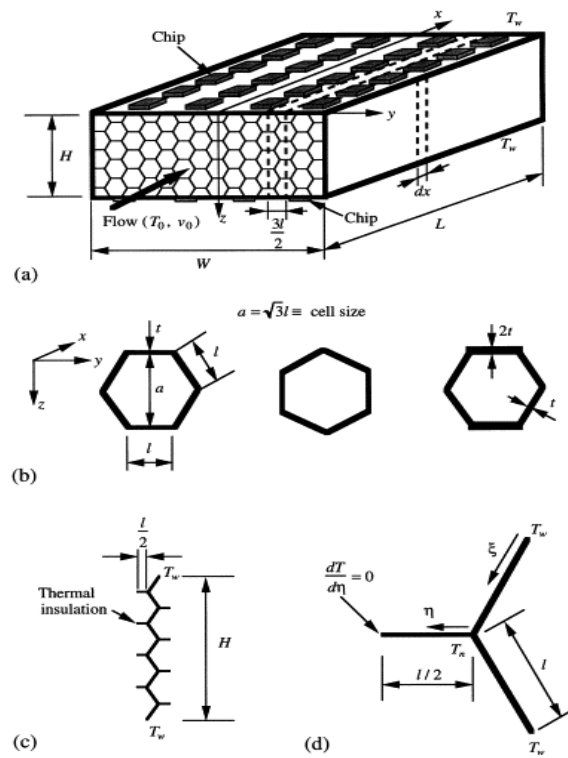


Figure 2.22 (a) notations for setup; (b) hexagonal cells representation; (c) representation of fin attachment to the walls; and (d) local coordinates. [35]

One similar test rig for testing metal frame material was shown by Kim, Zhao [38] in Figure 2.23, where the lattice structure is treated as a heat sink in the forced convective channel.

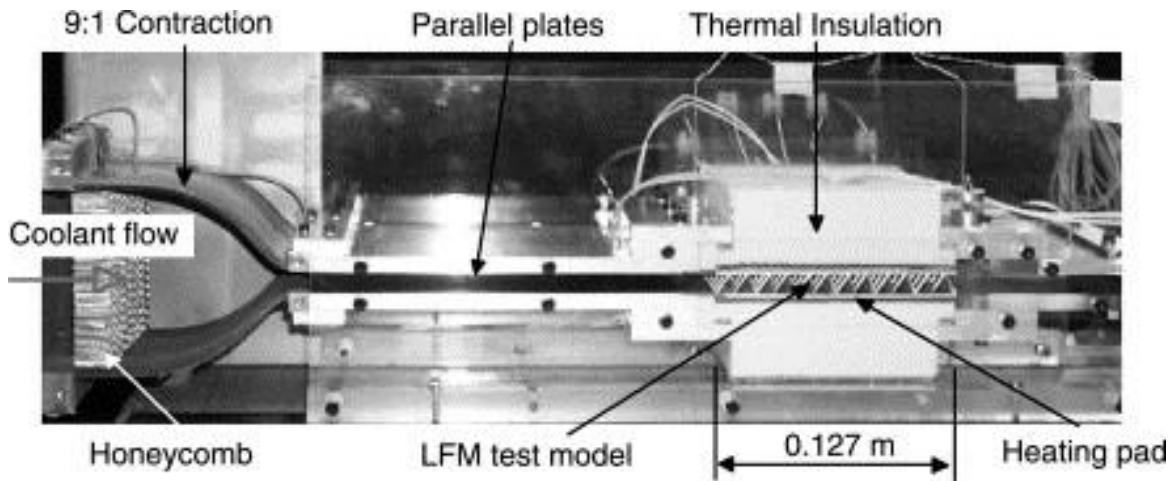


Figure 2.23 Test rig with LFM model [38]

For simulation on Software, different numerical and analytical domains can be defined as shown in Figure 2.24.

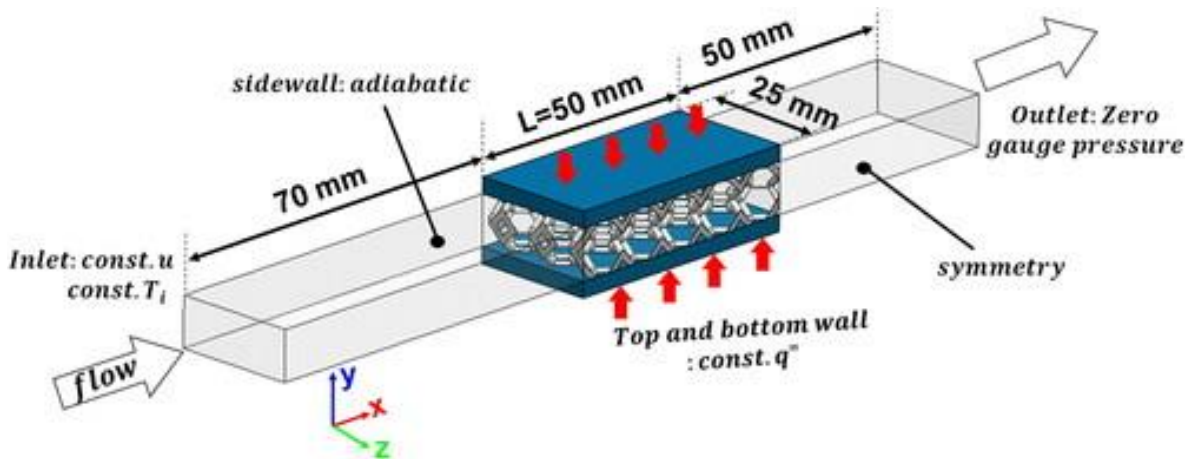


Figure 2.24 Isometric view of the computational flow domain [40]

These models show that lattice structures are simulated inside a flow domain which can be a box or a cylinder. Table 2.3 summarizes the differences between these two simulation/computational flow domains.

Table 2.3 Difference between the box and cylindrical flow domain (adapted from idealsimulations [42])

Box Computational Flow Domain	Cylindrical Computational Flow Domain
Boundaries are easier to define due to a greater number of faces.	One spherical wall is there, along with an inlet and an outlet.
More suitable for the interaction of a car with a moving road or aeroplane in ground effect.	Suited for free stream analysis and for axis-symmetric bodies like lattice structures.
Hydraulic Diameter can vary as the object might not be symmetric.	Hydraulic diameter is the diameter of the cylinder.

For lattice structures, to reduce the computational cost, the cylindrical domain is chosen in this research. The simulation software chosen in this research is selected by Siemens Energy.

### 2.4.2 Mesh or Grid Convergence Study

This section covers the step, which is the beginning of the analytical simulation. Mesh or grid generation is a very important step and is step two (as discussed in Figure 2.20) after geometry or flow domain definition. The geometry is discretized at this step into a number of elements (Figure 2.25) or, numerically, into a number of stiffness matrices. Thus, to create those elements, the smallest size of the element must be known, which is also known as base size in StarCCM+ or element size in ANSYS. This whole process in FEM is known as mesh generation. Typically, the smaller the mesh size or element size is, the more accurate the results are, but the number of elements would increase. However, as the number of elements increases, the computational time increases significantly, and so does the cost of computation. Thus, engineers often perform mesh convergence studies or grid convergence studies to reach an optimum level of mesh/grid size, where the results are independent of the size of the element, along with saving time and cost.

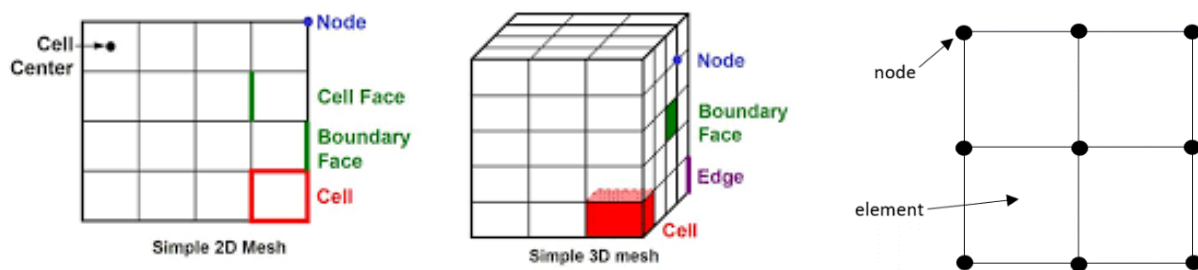


Figure 2.25 Terminologies while creating mesh [43] [44]

Generally, there are three different levels of mesh: fine, coarse, and medium, as shown in Figures 2.26 and 2.27. A fine mesh has a smaller element or base size (which gives a large number of elements), followed by medium and coarse, respectively. As the refinement of mesh decreases, the total number of elements generated also decreases.

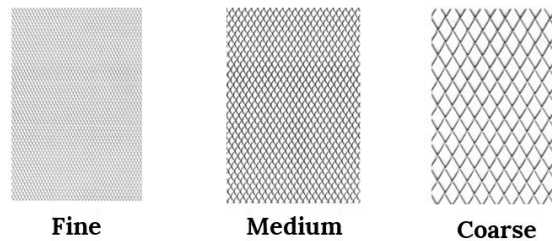


Figure 2.26 Levels of mesh

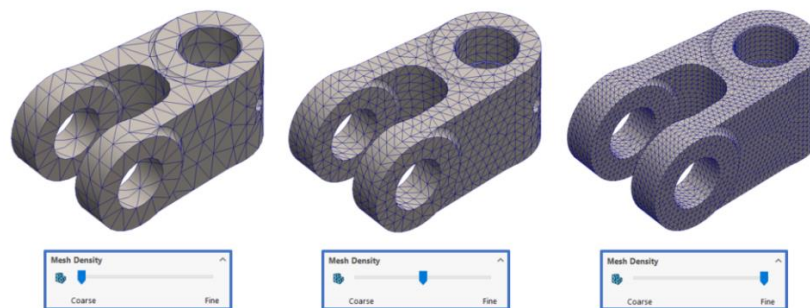


Figure 2.27 Levels of mesh – (reference: Figure 2.20)

The following steps are used to do a mesh/grid convergence study:

1. Fix the base size/ smallest element size equal to the smallest value of the dimensional parameter of the CAD geometry.
2. Generate the mesh and simulate using the boundary conditions given.
3. Choose an output parameter like temperature, Nusselt's number or friction factor to get the result and store its value.
4. Decrease the base size and again generate a new mesh. Compare the value of the output parameter to the one which was obtained previously.
  - 4.1 if the values of the output parameter remain unaltered, that means the results are not dependent on the base size.

4.2 if the values of the output parameters do not match with previous output parameters, then the base size should be, and follow step 4. This must be done iteratively until the change of base size does not affect the output results.

Calmidi and Mahajan [34] performed a grid convergence study and found that the value of the Nusselt number does not change after a certain grid spacing or, in simple terms, after a minimum size of the element (Table 2.4). Their study illustrated that the size of the element chosen does not affect their results much.

Table 2.4 Mesh Convergence study based on element size [34]

Element size	Nusselt Number
$5 \times 10^{-4}$	10.97
$2.5 \times 10^{-4}$	11.02

Another type of mesh convergence study was performed by Narkhede and Sur [33], where they investigated for the minimum number of elements required so that the results are independent of the initial base/element size (Figure 2.28). Thus, the results of the grid convergence study can be analyzed either by choosing the optimum base size (after which results remain unaltered) or by counting the number of elements generated on particular grid size. However, the number of elements obtained depends on the base size.

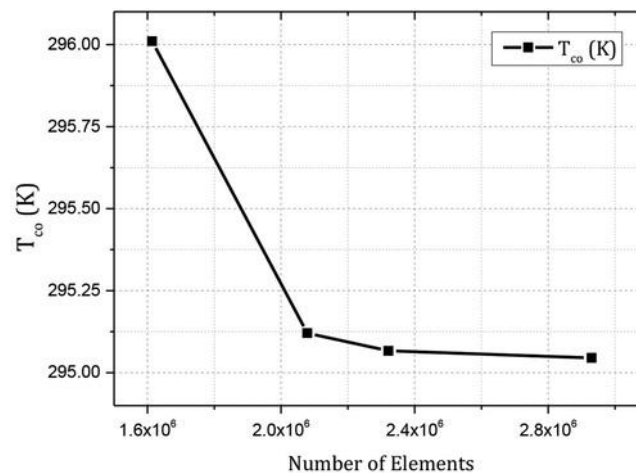


Figure 2.28 Mesh convergence study based on the number of elements in the whole geometry [33]

Furthermore, the dimensions of lattice structures are in millimetres. Thus, the smallest element size should be smaller than those dimensions to sustain the surface features of lattice structures.

## 2.5 Research Gaps in the Literature and Research Scope

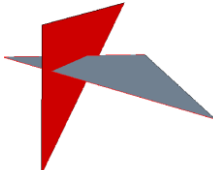
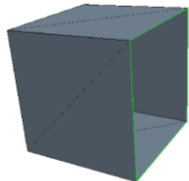
This section covers gaps found in the literature and, in turn, discusses the final research scope of this thesis.

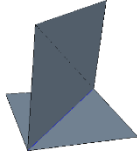
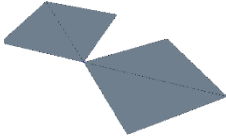
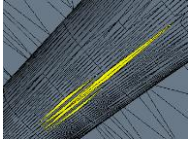
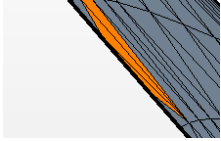
### 2.5.1 Gaps in the literature

Summarising the literature, it is found that extensive research has been carried out to understand the mechanical performance of lattice structures. However, very little research investigates the flow and thermal performance of these structures. This is due to the following facts:

1. As discussed in Section 2.4.2 high computational cost made the simulation of lattice structures to investigate their flow and thermal behaviour more challenging.
2. Exporting the CAD model to the simulation platform can result in a failed mesh due to poor tessellation or poor surface of the geometry. This, in turn, can fail the mesh generation process. Thus, it becomes necessary to identify the problems with the CAD geometry before exporting it to the simulation software. Some of these issues are shown in Table 2.5. These examples are gathered using StarCCM+.

Table 2.5 Errors captured in StarCCM+ (Adapted from Lidar [45] and Behera [46])

<b>Problems in CAD Geometry</b>	<b>Explanation</b>	<b>Pictorial representation</b>
<b>Pierced Face</b>	Two faces intersect each other.	
<b>Free edges</b>	They do not make a closed volume.	

<b>Problems in CAD Geometry</b>	<b>Explanation</b>	<b>Pictorial representation</b>
<b>Non-Manifold Edges</b>	These edges are connected to three or more faces.	
<b>Non – Manifold vertices</b>	Only one vertex is connected to two faces.	
<b>Face Quality – Tessellation or Curvature</b>	The curvature is lost while meshing.	 [46]
<b>Face proximity</b>	How close faces are to each other.	 [46]

Apart from these facts, the majority of experimental data presented in the literature only focused on a particular type of lattice structure, and there is no basis for comparison between different lattice structures. This is due to the fact that the 3D printing cost of metal lattice structures is still high.

### **2.5.2 Scope Definition**

Based on the research gaps discussed in the previous section, the following points define the scope of this research:

1. To identify the lattice structures that can be generated on the Siemens NX and nTopology.
2. To repair the geometry on StarCCM+ for successful mesh generation in ANSYS.

3. To optimize the size of the element while generating the mesh (mesh convergence study) to minimize the computational cost and time on ANSYS.
4. To compare the flow and thermal performance of strut-based and surface-based lattice structures.
5. To prepare the flow and property charts for design engineers based on Nusselt number, friction factor, Reynold's number, convective heat transfer coefficient and dimensional characteristics of the structure.

## Chapter 3: Methodology

This chapter introduces the methods adopted to carry out the geometric modelling, the mesh generation study, and the simulations of lattice structures.

### 3.1 Geometric Modelling

From Section 2.3.1 the top 90 percent of the lattice structures investigated in the literature are chosen to be the target of this research. They include all the lattice structure types highlighted in solid bars in Figure 3.1. The list includes BCC, Rhombic Dodecahedron, Diamond, Cube, TPMS Gyroid, BCCZ, TPMS Diamond, Octet Truss, Truncated Octahedron, FCC, FCCZ, Octahedron, FCCZ, Truncated Cubeoctahedron (TCO), Truncated Cube, Rhombic Cubeoctahedron (RCO), CCP, Tetrahedron, SHC, Honeycomb, TPMS Cube, TPMS I-WP, TPMS Primitive.

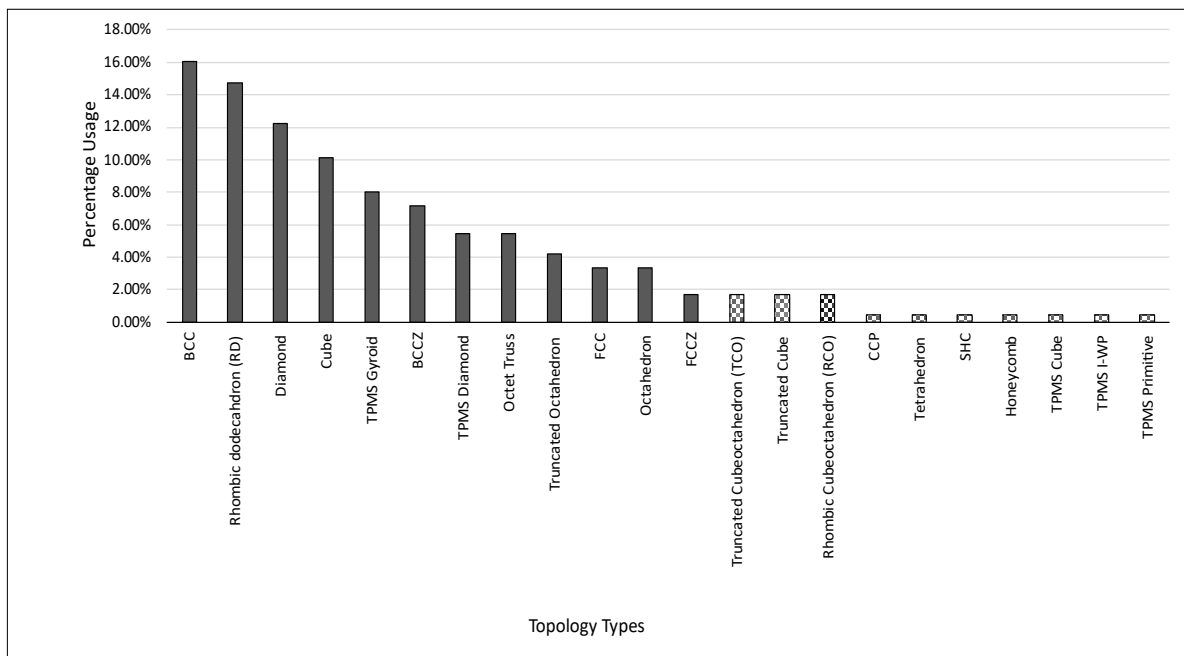


Figure 3.1 Topology selection for modelling (adapted from Figure 2.16)

These lattice structures contain strut-based and surface-based lattice structures. The platforms provided by Siemens Energy include NX and StarCCM+ for geometric modelling and surface repair of lattice structures, respectively. Due to the limitation of fabrication capability, the minimum strut diameter can not be less than 0.5mm. Linear patterns of lattice structures can be modelled using typical CAD tools. Thus, the strut-based lattice structures are modelled using Siemens NX. However, surface-based lattice structures have to be modelled separately. Implicit modelling is a common technique used to model surface-based lattice structures, as the surfaces

of these lattice structures are expressed as mathematical equations. The following sections discuss the geometric modelling of strut-based and surface-based lattice structures.

### 3.1.1 Strut-Based lattice structures

Computer-aided design modelling in Siemens NX combines wireframes, solid, surface parametric and direct modelling [47]. A designer can use any of these approaches; thus, in this research, solid modelling of strut-based lattice structure geometries is done using features and constraints, which is known as parametric modelling. It has the following benefits:

1. Once a unit cell is modelled, its dimensions can be parametrized so that they can be altered easily.
2. Once a unit cell is modelled, it can be modified into other topologies as well.

Thus, once the parameters and constraints are fed to a parametric modeller, it computes a model which can be represented in various formats like B-rep, voxel, or mesh. In Siemens NX, geometric models are generally represented in the format of B-rep. An illustration of this process is given in Figure 3.2.

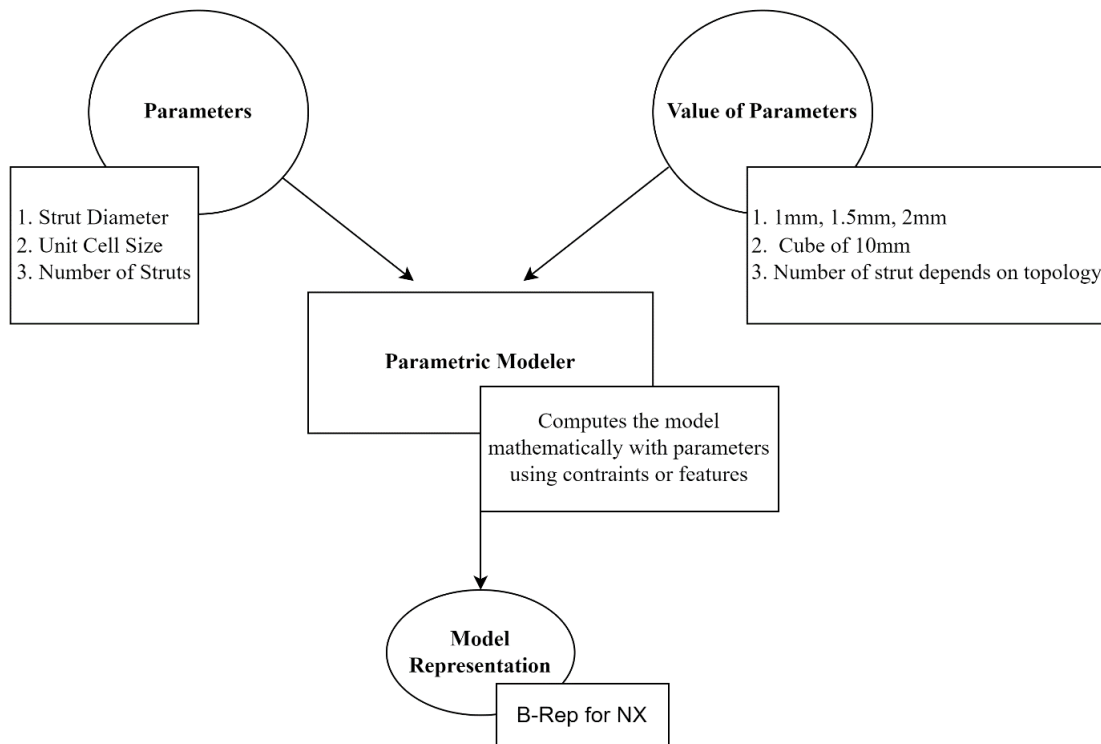


Figure 3.2 Modelling Strut-Based lattice structures in NX

B-rep of models have two basic entities:

1. Topology, which has faces, edges and vertices.
2. Geometry which has surfaces, curves, and points.

The bounded portion of a surface is called the face, a bounded piece of the curve is called the edge, and a vertex lies on a point. Other entities are formed by using these basic entities to connect surfaces (known as the shell), multiple edges to bound a face (known as a loop) and half edges (known as loop-edge links) [48].

With the parameters defined as shown in Figure 3.2, seven types of strut-based lattice structures-geometric models are generated. A schematic diagram of the modelling of a BCC unit cell is shown in Figure 3.3.

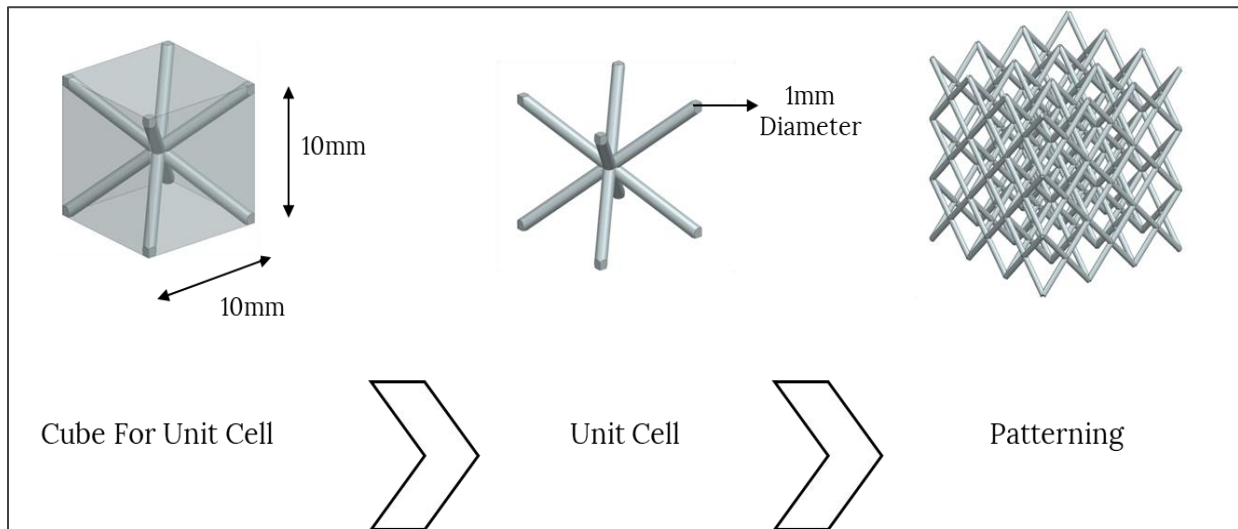
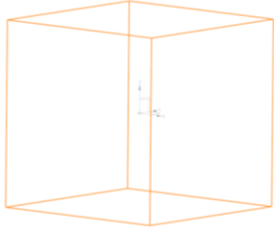
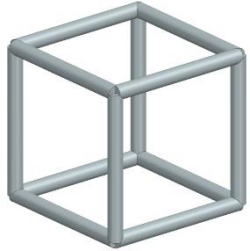
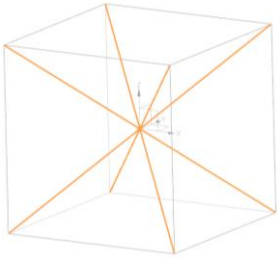
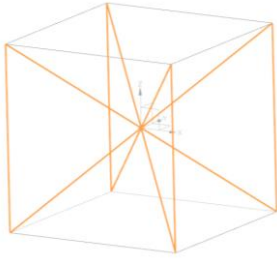
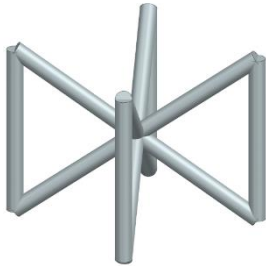
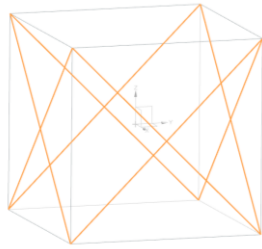
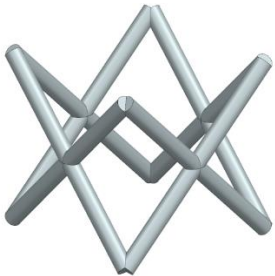
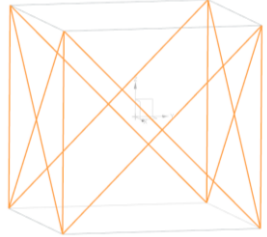
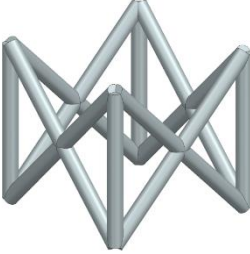
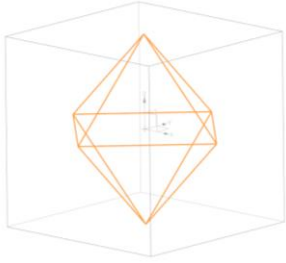
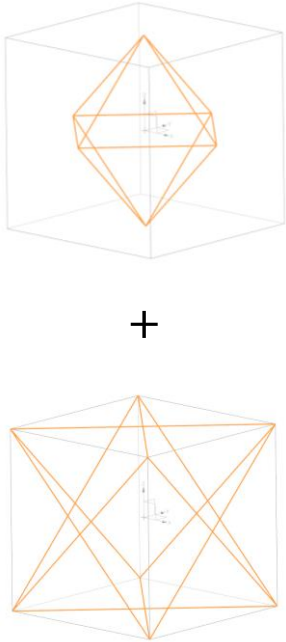
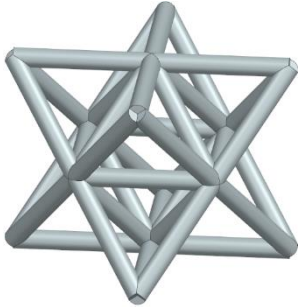


Figure 3.3 Schematic representation of modelling

The strut length size and the unit cell size remain the same, but the arrangement of the rods or struts changes. BCCZ and FCCZ lattice structures are obtained by adding z struts to the BCC and the FCC lattice structures, respectively. The features curves of all the seven strut-based lattice structure topologies, along with their B-reps, are shown in Table 3.1.

Table 3.1 Strut-Based lattice structures topology representation

Topology	Feature Curves used for the model inside a cube	B-rep
Primitive or Cubic		
Body-centred Cubic (BCC)		
Body-centred Cubic with z-struts (BCCZ)		
Face-centred Cubic (FCC)		

Topology	Feature Curves used for the model inside a cube	B-rep
Face-centered Cubic with z-struts (FCCZ)		
Octahedron		
Octet Truss		

### 3.1.2 Surface-Based Lattice Structures

Surface-based lattice structures, such as TPMS, are defined by equations and not by the network of surfaces and edges or polygons. Thus, they can not be modelled using traditional geometric modelling techniques.

Implicit modelling came into the picture when 3D geometry required modelling through equations rather than vertices, faces and edges (B-rep or Mesh). A very good analogy was given by the pioneers in the field nTopology [49]. They gave an example of a situation where one often navigates the weather applications to find the optimal places for camping or resting while covering huge distances by road. Information like temperature, wind speed, visibility, and rain precipitation assist in finding locations at different distances to stop and take a rest. The information like temperature is consistent everywhere, which helps to create a sample of temperature predictions for different locations. Temperature is known as a field and is used to make decisions. In a very similar way, other fields like force, velocity, and distance are used to define a geometry or a model.

On nTopology platform, distance fields are used to define a geometry. For every equation fed to the solver inside this software, the output is not only the representation of the geometry but also the value of distances outside or inside the boundaries. Thus,

1. If the distance value is equal to zero, then it defines the boundary of the geometry.
2. If it is negative defines the inside of the boundary.
3. A positive value signifies outside of this boundary. (Figure 3.4)

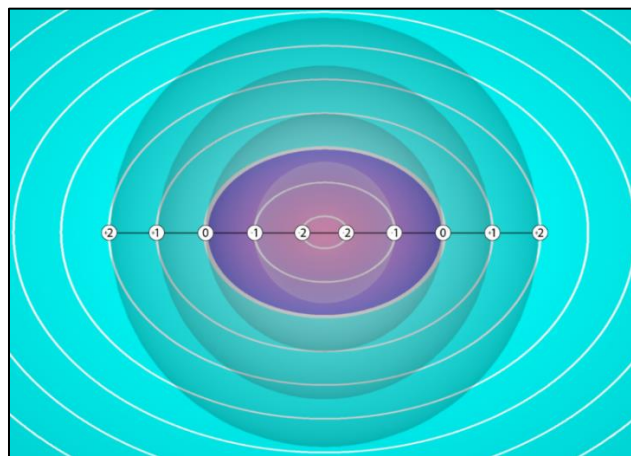


Figure 3.4 Distance field representation in nTopology for a sphere. [49]

There are two main advantages of implicit modelling:

1. The offsetting of the geometries becomes easy and consumes less data.
2. Simple Boolean operations generally fail in the conventional CAD system due to the complexity of the geometries, as the system must recalculate and generate new faces or entities, as shown in Figure 3.5. However, in implicit modelling, the maximum and minimum values are extracted between the fields (as shown in Figure 3.6) for boolean intersection and boolean union, respectively.

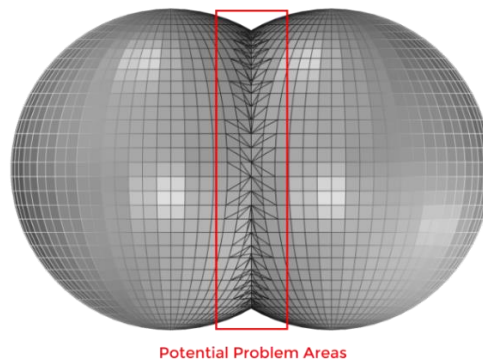


Figure 3.5 Boolean operations form new faces, vertices, and edges in Conventional CAD techniques. [49]

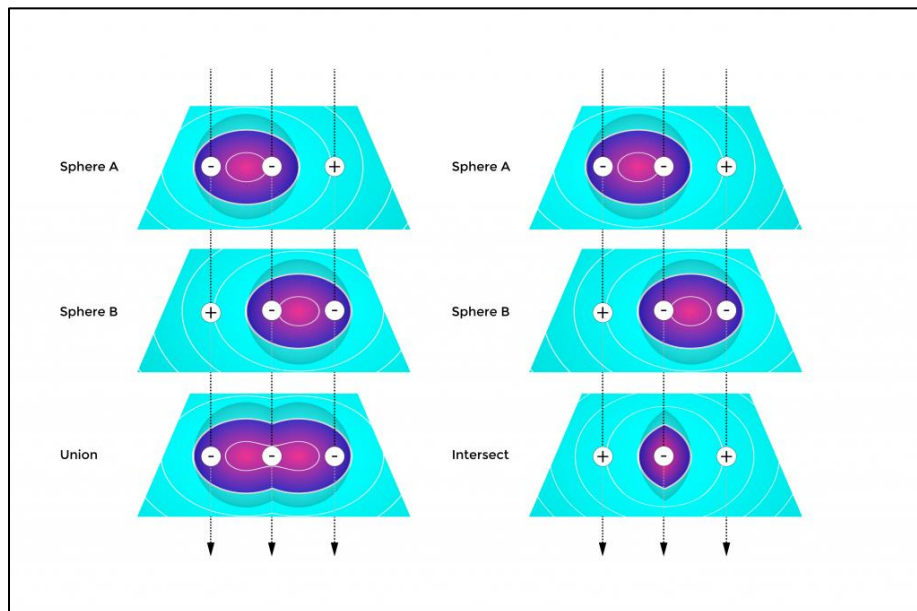


Figure 3.6 Left: Boolean union, Right: Boolean intersect [49]

A clear depiction of difference between B-rep and implicit representation is shown in Figure 3.7.

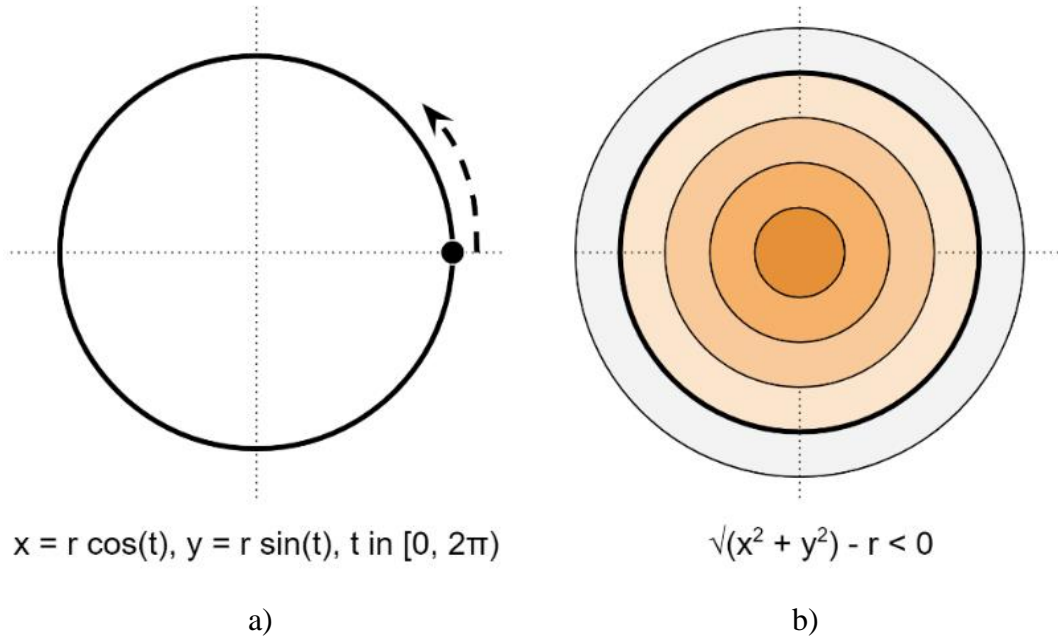


Figure 3.7 a) A circle represented in a B-rep and b) a distance field (right) [50].

Therefore, in a very similar way, TPMS structures are modelled on the nTopology platform using implicit modelling in this research. The following are the details of the implicit modelling steps of TPMS surface-based lattice structures.

If a surface of geometry has mean curvature of zero at any point, then it is known as a minimal surface, and along with this, if this surface is both periodic and infinite in 3D, then it is known as TPMS [51].

#### TPMS Gyroid:

- The equation used to create the surface:

$$f(x, y, z) = \sin(X)\cos(Y) + \sin(Y)\cos(Z) + \sin(Z)\cos(X) = C \quad (3.1)$$

where X, Y and Z are constants related to the size of the unit cell in the x, y and z directions, respectively. And the function  $f(x,y,z)$  is calculated over a constant value C which defines the curvature of these surfaces.

- The distance field of Equation (3.1) is highlighted in blue in Figure 3.8

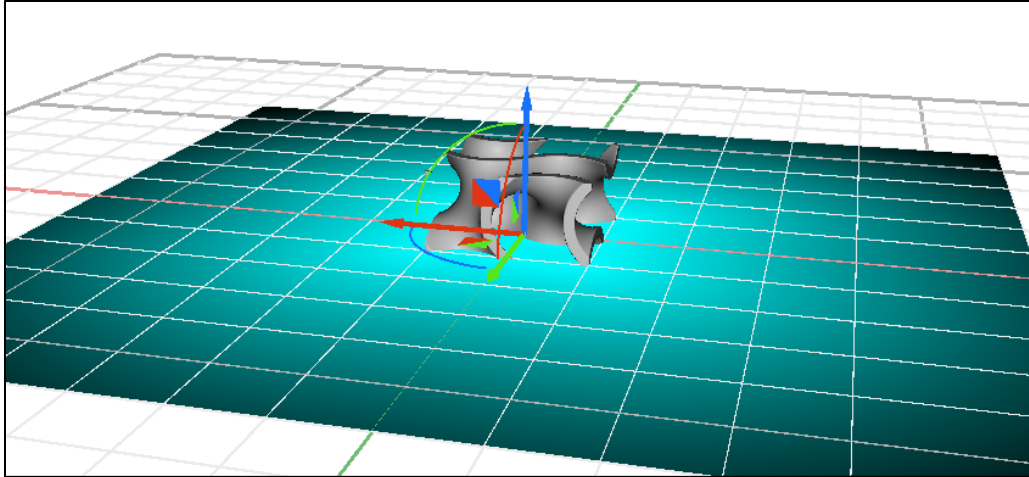


Figure 3.8 Distance Field for TPMS Gyroid

- The implicit body of TPMS Gyroid is shown in Figure 3.9.

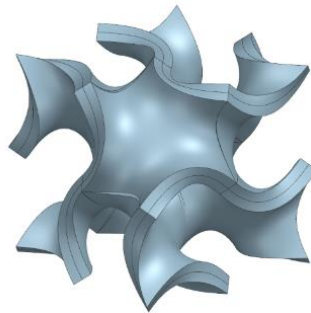


Figure 3.9 Geometry for TPMS Gyroid

### TPMS Diamond:

- The equation used to create the surface:

$$f(x, y, z) = \sin(X) * \sin(Y) * \sin(Z) + \sin(X) * \cos(Y) * \cos(Z) + \cos(X) * \sin(Y) * \cos(Z) + \cos(X) * \cos(Y) * \sin(Z) = C \quad (3.2)$$

where X, Y and Z are constants related to the size of the unit cell in the x, y, and z directions, respectively. And the function  $f(x,y,z)$  is calculated over a constant value C which defines the curvature of these surfaces.

- The distance field of Equation (3.2) is highlighted in blue in Figure 3.10.

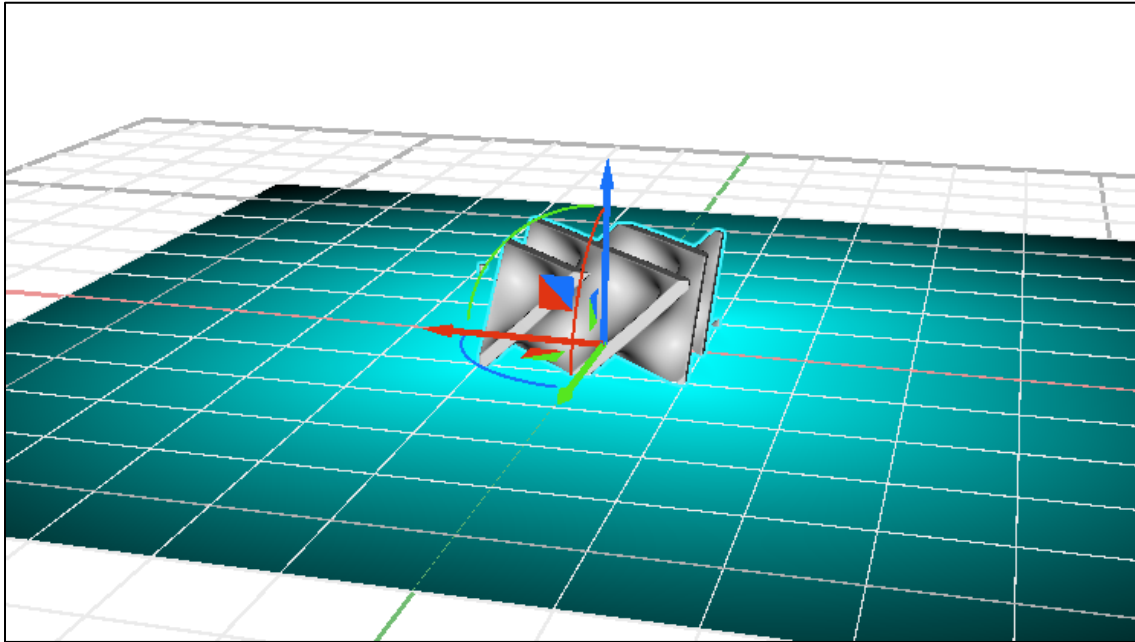


Figure 3.10 Distance Field for TPMS Diamond

- The implicit Geometry of the TPMS Diamond is shown in Figure 3.11.

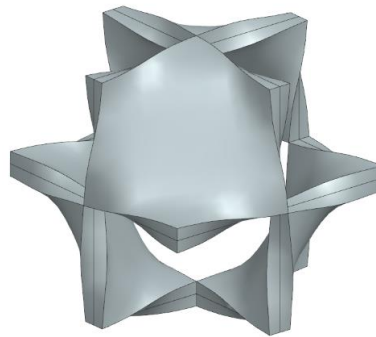


Figure 3.11 Geometry for TPMS Diamond

### 3.2 Simulation

The next step after modelling is to prepare the models for simulation. As discussed in Section 2.5.1, the geometric models must be repaired in Star CCM+ for discretizing the geometry for meshing in ANSYS. Thereafter, a grid convergence study is carried out to identify the best mesh quality (optimum base/element size) to carry out the required CFD simulation. Then, the final step is to

feed the prepared mesh geometry for simulation to get the required results. This section introduces the methods adopted on various platforms to implement these steps.

### 3.2.1 Constructing Computational Domain

As discussed in Section 2.4.1 of Chapter 2, the simulation domain chosen for this research is cylindrical due to the fact that the lattice structures are axis-symmetric and require only one main wall, one inlet, and one outlet for the simulation. Furthermore, a cylindrical computational flow domain saves computational time because a cylinder has only one wall, while a cuboid has multiple faces acting as walls. Mesh quality is also consistent (conformal mesh) throughout the wall of the cylindrical domain.

To design the computational domain for CFD, the geometric model of that domain must be generated. This is because air or any fluid in CFD interacts with the computational domain and the boundaries of the geometry. This computational domain is the region around the lattice structure which is the negative of the original geometry. Thus, the lattice structure network of 3x3x9 is subtracted from the cylinder height of 600 mm and radius of 30 mm to create a lattice structure seat, as shown in Figure 3.12. The dimensions of the computational domain do not affect the results if the flow is fully developed.

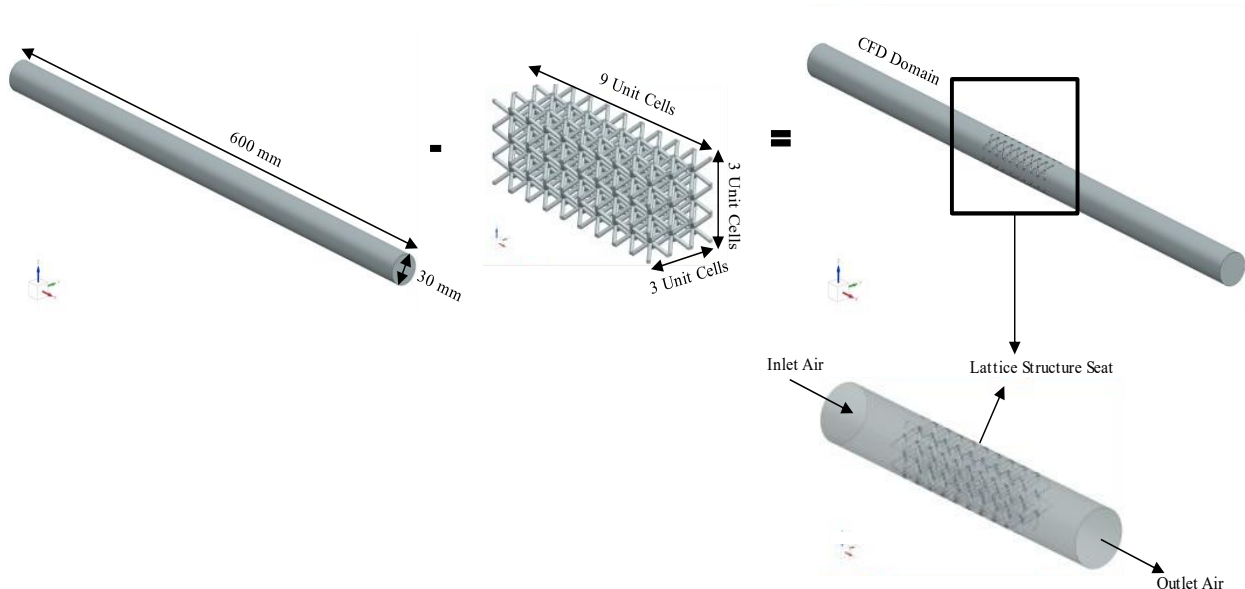


Figure 3.12 Computational flow domain for simulation

To compare the characteristics of lattice structures, the computational flow domain is kept consistent throughout the research.

### 3.2.2 Surface Repair

To diagnose the geometrical errors in the CAD models, which can lead to improper or failed mesh generation (discussed in Section 2.5.1 of Chapter 2), the surface repair tool provided by Siemens Star CCM+ is used to repair the surfaces. This built-in tool automatically detects the problems in the geometry, which further may cause inaccurate discretization during the mesh generation step, as shown in Figure 3.13. The following strategies are adopted to repair the geometric models in this research.

1. Pierced faces are generally fixed by removing the unwanted surfaces and patching them properly again.
2. Face quality is fixed by decreasing the tessellation of the surface or wrapping up the surface again using curved faces.
3. Face proximity is fixed by moving the overlapping surfaces apart. This can also be done by decreasing the tessellation of the surface.
4. Free edges are fixed by filling the gap between these edges with curved faces.

The fixations mentioned above are automatically performed by StarCCM+. But detection of these errors is a more important step before fixing them.

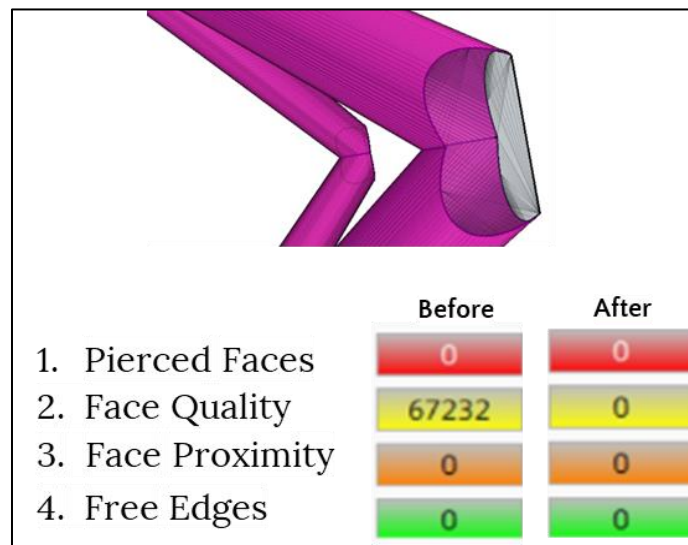


Figure 3.13 Surface Repair in Star CCM+

### 3.2.3 Mesh Generation

The next step after the surface repair is mesh generation, which is the discretization of the computational domain. To reduce the computational effort and cost, three different regions are defined. Two areas are the regions without the lattice structure seat, as shown in Figure 3.12, and one with the lattice structure seat. The former ones are given the coarser mesh with the bigger element size, and the latter is given the smaller size, that is, the finer mesh, as shown in Figure 3.14. This resulted in less number of elements and a conformal mesh generation.

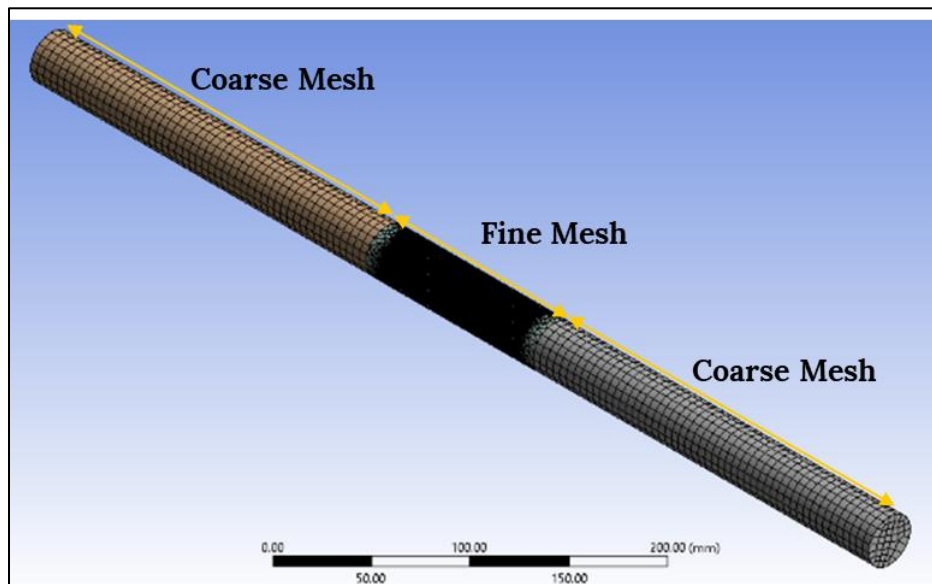


Figure 3.14 Mesh Generation

The grid/Mesh convergence study was done on three different base/element sizes. The results of this study can only be generated once the simulation is complete on each base/element size. Thus, they are discussed in the next chapter.

### 3.2.4 Boundary Conditions and Choice of Solvers

Setting up the boundary conditions and the selection of solvers are the final steps for the simulation. Since the lattice structures are planned to aid the combustion inside the combustor of the turbine engine, Siemens Energy provided the boundary conditions of the highly pressurized air entering the combustion chamber. These conditions are tabulated in Table 3.2.

Table 3.2 Boundary Conditions throughout the research

<b>Property</b>	<b>Value</b>	<b>Units</b>
Temperature of the inlet air	848	K
Pressure of the inlet air	3310000	Pa
Inlet Reynold's number	292000 (Highly turbulent), 30000 (Turbulent) and 1800 (Laminar)	-
Temperature at the lattice structure seat	1200	K
Density of the compressed air	13.60	Kg/m <sup>3</sup>
Dynamic viscosity of the air	0.00003757	Pa-s
Constant pressure specific heat capacity of the air	1109.81	J/kg-K
Thermal conductivity of the air	0.059891	W/m-K
Mach number	Less than 0.3	-

The Mach number calculated for the inlet velocity for all three Reynold's numbers is below 0.3. Thus, it is assumed that the air acts as an incompressible fluid. Moreover, it is also assumed that air is dry, perfect gas.

Ansys allows different turbulence methods to solve the turbulence models. The k-omega SST (Shear stress transport) model is the most commonly used model in the industry to solve such problems in CFD. It comes under the family of Reynolds-averaged Navier-Stokes (RANS) models. The conventional model, known as the k-omega model, is sensitive to free stream inlet turbulence properties. Therefore SST model was built to consider the effect of adverse pressure gradient, which is the case in the current research. Also, high Reynold's number flows create eddies by turbulence which cause shear instability near the walls and can give inaccurate outputs [52]. Thus, eddy viscosity is added to the conventional equations to conserve the energy more realistically.

The accurate mathematical representation for the k-omega SST model is given by the following equations:

The turbulent kinetic energy  $k_t$  is governed by [53]:

$$k_t = \frac{3}{2}(UI)^2 \quad (3.3)$$

where,  $U$  is the mean flow velocity, and  $I$  is the turbulence intensity.  $I$  is the level of turbulence or turbulent intensity and is generally defined at the inlet and is given by:

$$I = \frac{u'}{U} \quad (3.4)$$

where,  $u'$  root mean square of the turbulent velocity fluctuations and is calculated by:

$$u' = \sqrt{\frac{1}{3}((u'_x)^2 + (u'_y)^2 + (u'_z)^2)} = \sqrt{\frac{2}{3}k_t} \quad (3.5)$$

The mean velocity,  $U$  is calculated as follows:

$$U = \sqrt{(U_x)^2 + (U_y)^2 + (U_z)^2} \quad (3.6)$$

$\omega$  is the specific turbulent dissipation rate and can be calculated as follows:

$$\omega = (C_\mu)^{\frac{3}{4}} \frac{(k_t)^{1/2}}{l_t} \quad (3.7)$$

where,  $C_\mu$  is the turbulence model constant and is usually equals 0.09,  $k$  is turbulent kinetic energy and  $l_t$  is the turbulent length scale, which is the size of the energy domain containing eddies due to turbulent flow. Thus, turbulent viscosity,  $\nu_t$  is calculated as:

$$\nu_t = \frac{k_t}{\omega} \quad (3.8)$$

Also, to make the model even more realistic, ANSYS takes the values of turbulent intensity at the inlet. The model gives the following options:

1. High Turbulence: 5% to 20%: For high velocity flows entering the complex geometries such as the lattice structures or heat exchangers.
2. Medium Turbulence: 1% to 5%: For the flows with the geometries with medium complexity.
3. Low Turbulence: below 1%: Highly viscous fluid or stand-still fluids.

Thus, with the above-mentioned solver settings and boundary conditions, the lattice structures are tested for their flow and thermal performances for

1. Three different Reynold's Numbers: 292000 (For the combustor), 30000 and 1800 for comparing different types of flows.
2. Three different strut diameters or thicknesses at each Reynold's Number: 1mm, 1.5mm and 2mm. The nomenclature of different lattice structures with different strut diameters is given in Table 3.3.

Table 3.3 Nomenclature of lattice structures with different dimensions of struts and surfaces

<b>Strut Diameter/Surface thickness</b>	<b>Nomenclature</b>
1 mm	BCC1, FCC1, BCCZ1, FCCZ1 and so on.
1.5 mm	BCC1.5, FCC1.5, BCCZ1.5, FCCZ1.5 and so on.
2 mm	BCC2, FCC2, BCCZ2, FCCZ2 and so on.

As the output of the simulation, the convective heat transfer coefficient and friction factor across the structures are calculated. Also, the friction factor is compared with the friction factor for a similar standard flow channel, as discussed in the section. Thus, the values of the augmented friction factor, i.e.,  $f/f_0$  are obtained, where  $f$  is the friction factor obtained for lattice structures. The detailed simulation results and analysis are discussed in the next chapter.

## Chapter 4: Results and Discussions

This chapter discusses the results obtained from the methods followed from the design phase to the simulation phase. Section 4.1 focuses on the results of the mesh convergence study conducted to identify the base/element size, which does not affect the results obtained. Section 4.3 and 4.4 discusses the effects of geometric parameters and topology of lattice structure on the flow and convective heat transfer performance of the structures.

The planes chosen for obtaining the input and output parameters are illustrated in Figure 4.1. This sensitivity analysis is performed to choose a plane where the flow is fully developed. And then, the inlet plane is used to get the results by placing an output plane at the same distance from the origin where the input plane is selected but in the reverse direction.

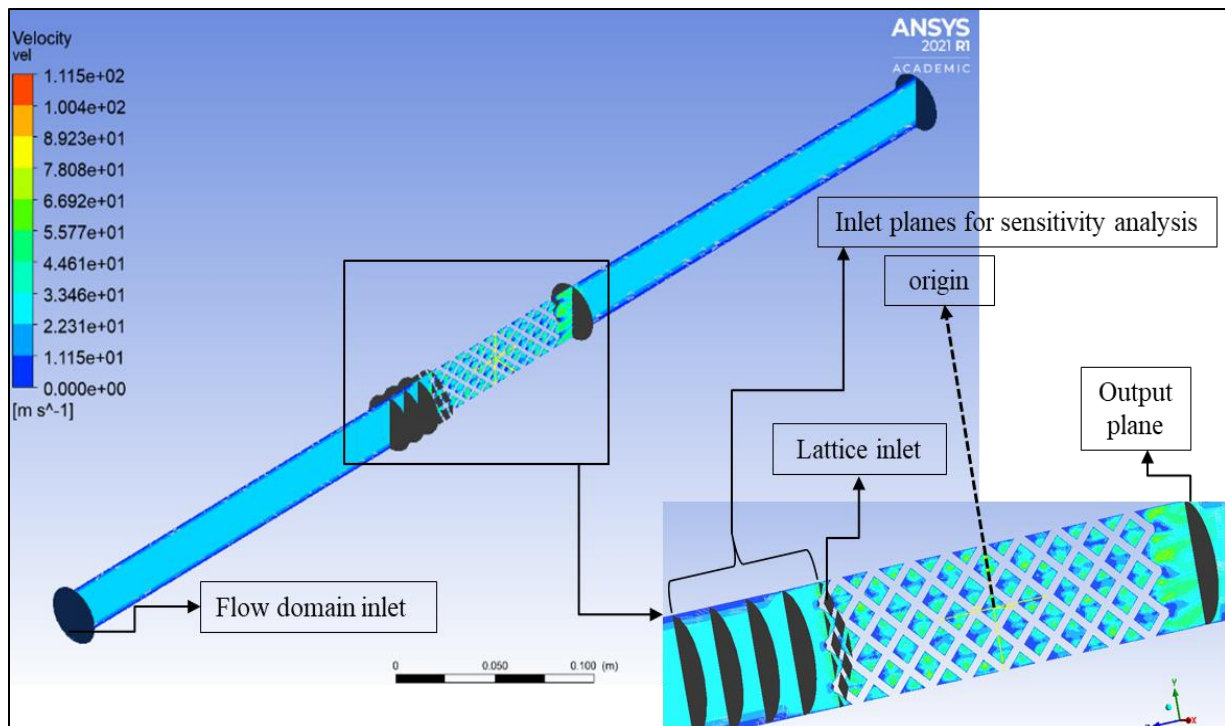


Figure 4.1 Planes chosen for sensitivity analysis.

A plane where the flow is fully developed is detected by obtaining the parameters such as temperature and by looking closely at the velocity profile of the flow. In Figure 4.1, only the boundary layer for the cylinder is considered and not for the lattice structure walls. This gives a suitable plane to choose before the lattice structure seat because velocity turbulence changes the velocity of the flow near the lattice structure seat inlet. Secondly, the diameter of the lattice

structures is so small that boundary layer thickness can be ignored for them (the output parameters remain the same, as can be seen in Table 4.1).

Table 4.1 Sensitivity Analysis

<b>Plane Position</b>	<b>Velocity at that plane</b>	<b>Temperature</b>
Flow Domain Inlet: 300 mm away from the origin	26.9000 m/s	848 K
85 mm away from the origin	26.9039 m/s	848 K
75 mm away from the origin	26.9042 m/s	848 K
65 mm away from the origin	26.9044 m/s	848 K
55 mm away from the origin	26.9044 m/s	848 K
At the lattice structure seat inlet: 45 mm away from the origin	52.5556 m/s	850.494 K

Thus, the plane at a distance of 55 mm is chosen to calculate the output parameters. The area-weighted average over these planes of any scalar property is used for intensive properties such as temperature, pressure, and velocity, while the mass-weighted average is used for extensive properties such as enthalpy, energy, and volume.

#### **4.1 Mesh Convergence Study**

After the plane selection and surface repair (as discussed in Section 3.2.2 of Chapter 3), the results of the mesh convergence study are obtained to choose the suitable element size for mesh generation. The results are obtained for both strut-based and surface-based lattice structures. The complex geometries with the highest number of struts and highest surface curvature from both the categories are chosen, i.e., Octet Truss and TPMS Diamond. Because if mesh generation is successful on these topologies, then topologies with less number of struts and surface curvature can lead to successful mesh generation.

It is found that for Octet Truss (strut-based), the results remain the same for anything below an element size of 0.5 mm, as shown in Figure 4.2. Thus, 0.5 mm is chosen to produce the mesh for the lattice structure seat. Similarly, for TPMS Structures, 0.4 mm is chosen to produce the mesh, as shown in Figure 4.3. These sizes are chosen as per the steps discussed in Section 2.4.2 of Chapter

2 to perform mesh convergence study. The mesh convergence study also resulted in successful mesh generation with conformal and fine mesh elements at the boundaries.

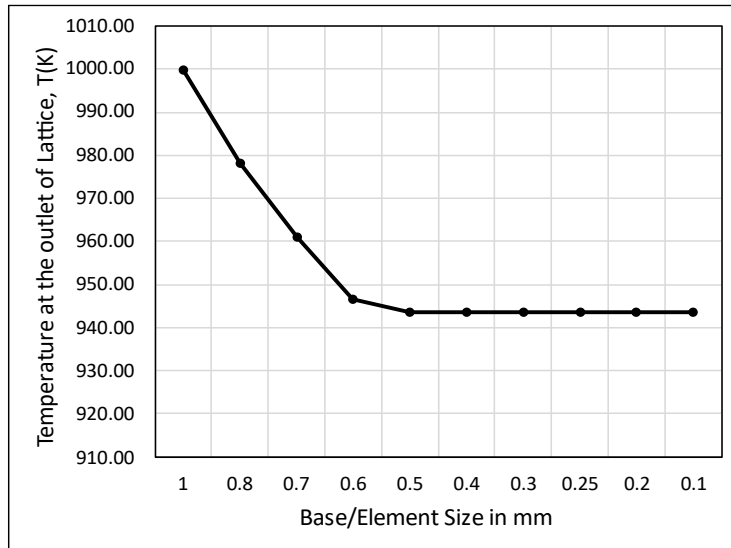


Figure 4.2 Mesh/Grid Convergence results for Octet Truss

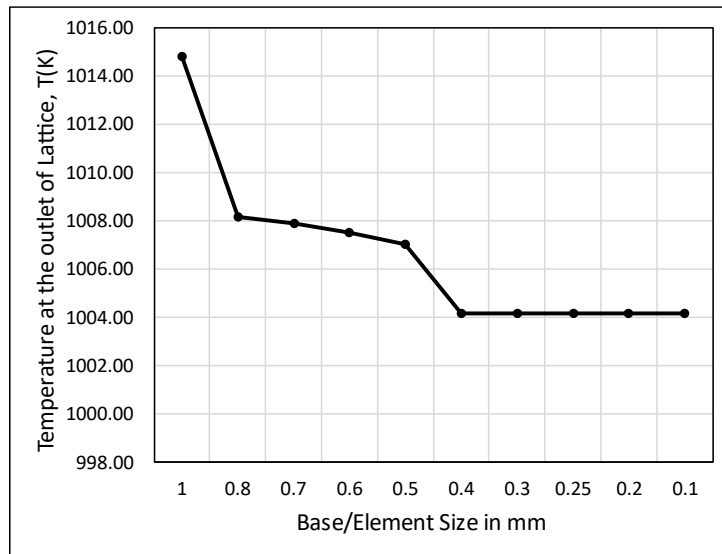


Figure 4.3 Mesh/Grid Convergence results for TPMS Diamond

## 4.2 Dimensional Characteristics of Lattice Structures

Available surface area for heat convection plays a vital role in the heat transfer rate across any structure (discussed in Section 2.2 of Chapter 2). However, it is also known that the volume of the

structure affects the heat transfer rate as well. To understand the effects of surface area as well as the volume of lattice structures on heat transfer rate, an example of a smaller ice cube melting faster than a big block of ice is considered where the smaller cube has a relatively smaller volume in which the heat has to be absorbed as compared to that of the larger cube [54]. Dimensionally, the smaller ice cube has a much larger surface area to volume ratio. Henceforth, the dimensional data of lattice structures from CAD models are extracted to obtain the trend of surface area to volume ratio (S/V) with respect to the porosity of lattice structures. Moreover, this S/V ratio can also be important if light weighting is taken into consideration.

There are various dimensional parameters that can help to enhance the S/V ratio of lattice structures. These can be porosity, the curvature and periodicity for surface-based lattice structures and the angle of inclination for strut-based lattice structures. For this research, only the porosity is considered to compare different structures. Other dimensional parameters are related to mathematical modelling and analysis and are not included in the scope of this research.

It can be seen from Figure 4.4 that with the increase of the porosity of lattice structures, the S/V ratio increases for strut-based lattice structures.

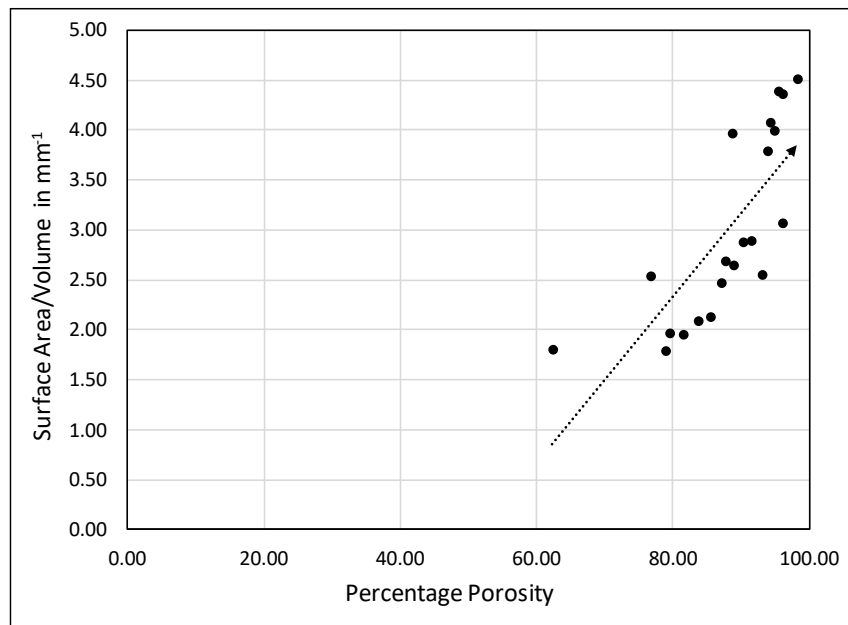


Figure 4.4 Variation of surface area to volume ratio with porosity of strut-based lattice structures

And a similar trend is seen with the surface-based lattice structures, as shown in Figure 4.5. This is because, as the porosity, that is, the empty volume, of lattice structures increases, their volume decreases. Therefore,  $S/V$  increases.

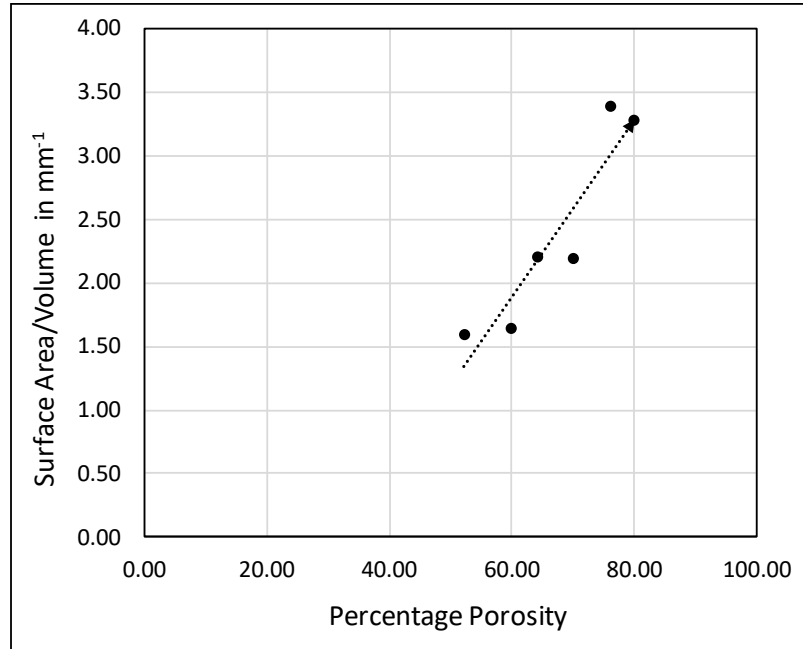


Figure 4.5 Variation of surface area to volume ratio with porosity of surface-based lattice structures

### 4.3 Flow Performance Characteristics

As discussed in Section 2.2 of Chapter 2, the property that influences the flow performance of lattice structures is the friction factor. The friction factor represents the pressure loss of the air across lattice structures. Determining pressure loss is important for the combustor of a gas turbine, as a very large pressure loss can result in less work output at the turbine stage.

According to the scope of this research, it is important to understand the friction factor of different types of lattice structures. Thus, the friction factor augmentation is plotted for various lattice structures for three different Reynold's numbers, as discussed in Section 3.2.4 of Chapter 3. Since the friction factor depends on the pressure drop across the structures, similar lattice structure topologies are grouped together for comparison. They are discussed in detail in the following sections.

### 4.3.1 Flow Characteristics of Primitive Lattice Structures

Figure 4.6 illustrates that the augmented friction factor increases on increasing the strut diameter. This is because thicker struts decrease the volume of the air-flow path. This induces a pressure drop. Furthermore, this trend is observed across all three Reynold's numbers.

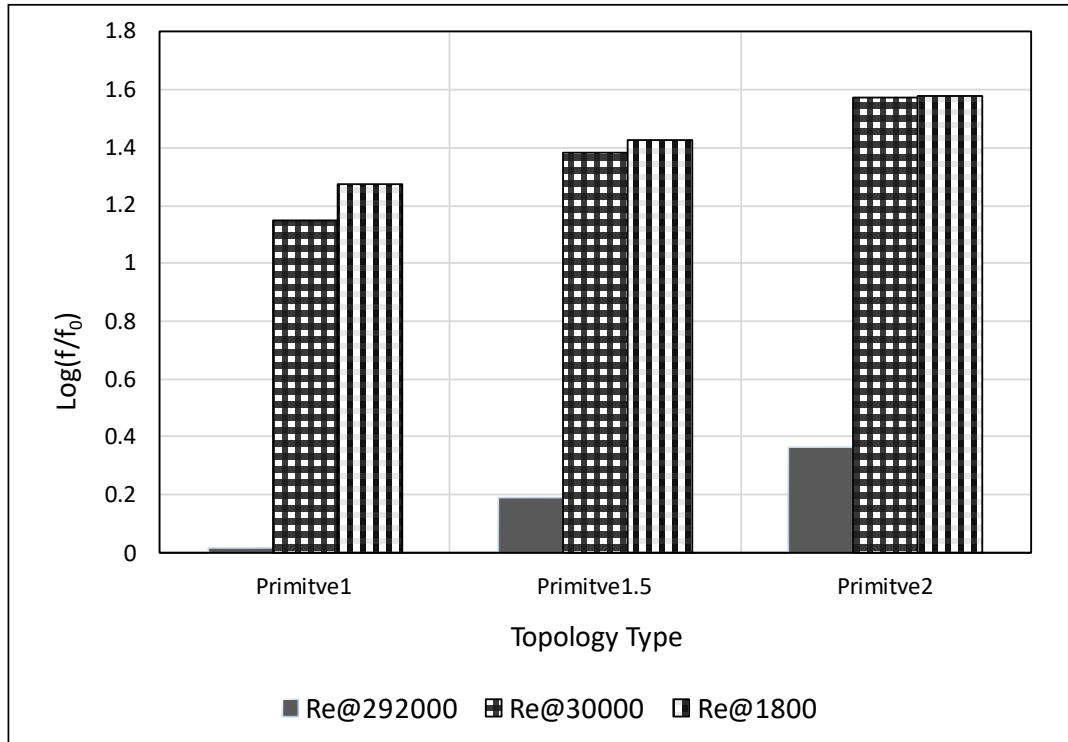


Figure 4.6 Friction factor augmentation ( $f/f_0$ ) across 3 different Reynold's number for Primitive lattice structures

### 4.3.2 Flow Characteristics of BCC, BCCZ, FCC and FCCZ Lattice Structures

The following points are observed in Figure 4.7:

1. Introducing z-struts to the BCC lattice structure affects the air-flow path resulting in a higher pressure drop for all three Reynold's numbers. This is because the perpendicular orientation of z-struts becomes an obstruction to the air-flow path. Hence, inducing pressure drop.
2. The average increase in augmented friction factor value due to the introduction of z-struts is 36%.

- It is also seen that increasing the strut diameter of BCC and BCCZ lattice structures is also increasing the augmented friction factor for all three Reynold's numbers. This clearly implies that strut diameter affects the friction factor.
- The average increase in augmented friction factor values due to increasing the strut diameter is 76%.
- Thus, increasing the strut diameter of BCC and BCCZ lattice structures has a more predominant effect on the augmented friction factor as compared to the effect caused by the introduction of a perpendicular z-strut.

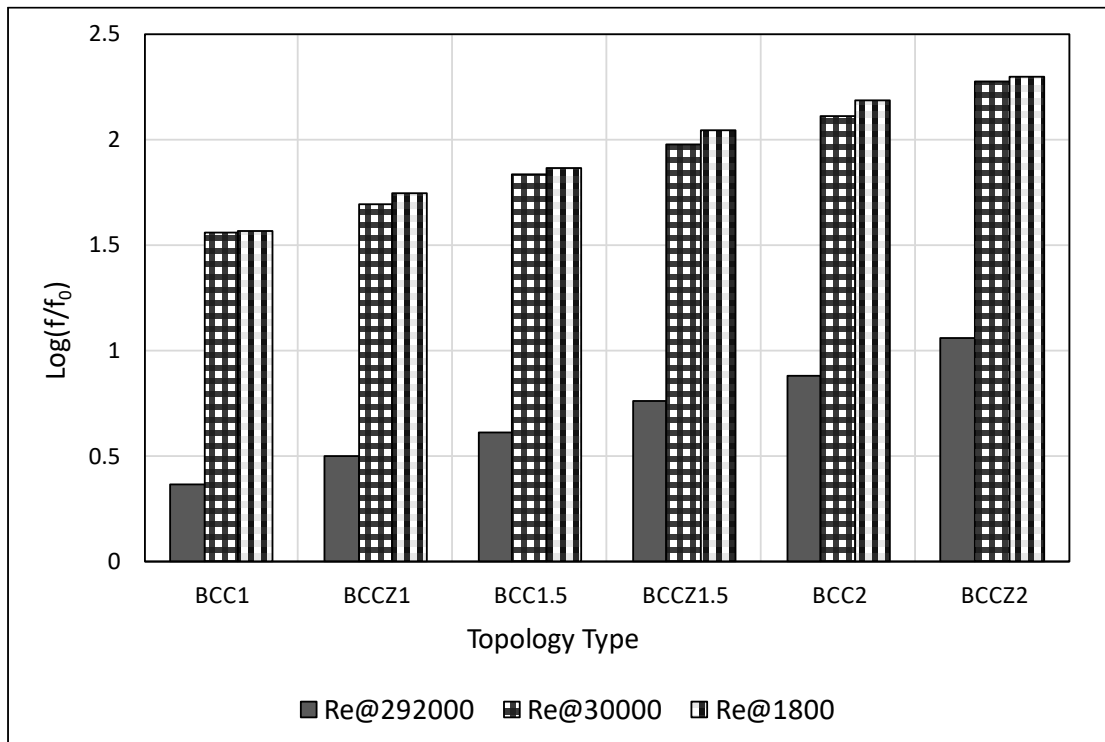


Figure 4.7 Friction factor augmentation ( $f/f_0$ ) across three different Reynold's numbers for BCC and BCCZ

Figure 4.8 illustrates the same observations for FCC and FCCZ lattice structures as discussed in the points above for BCC and BCCZ lattice structures. Furthermore, it is observed that:

- There is an average increase of 17% in augmented friction factor values for FCC(Z) lattice structures as compared to the values of augmented friction factor for BCC(Z) lattice structures.
- The friction factor increases as Reynold's number decreases regardless of the lattice structure topology.

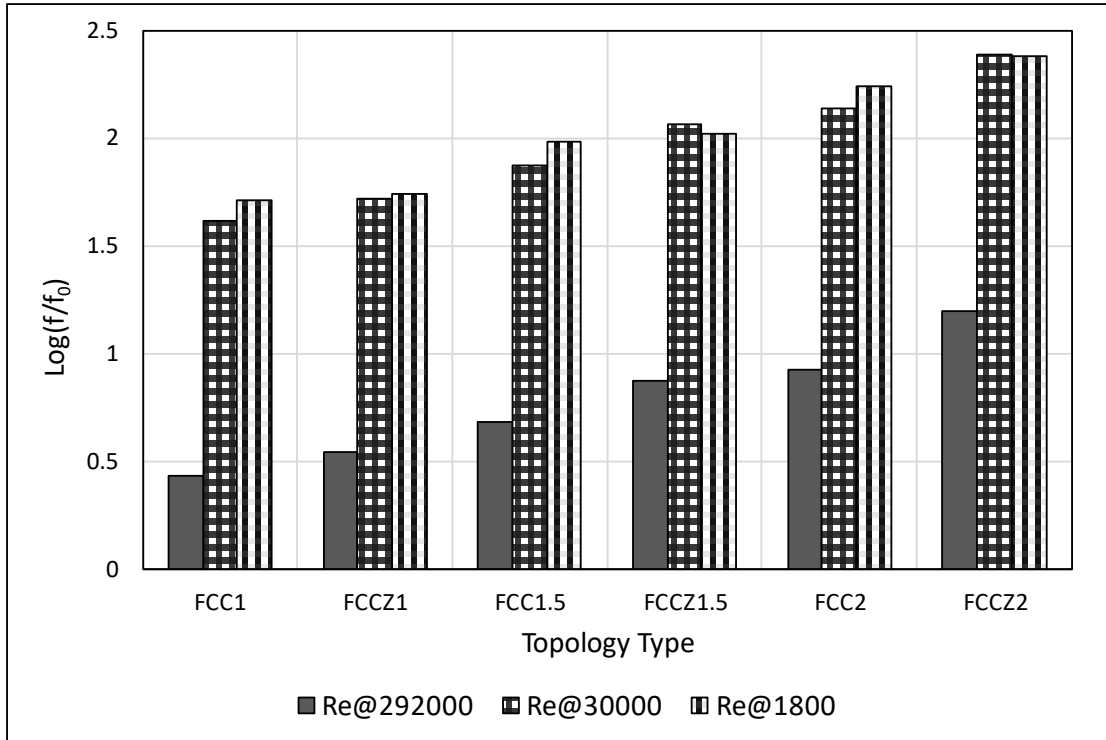


Figure 4.8 Friction factor augmentation ( $f/f_0$ ) across three different Reynold's numbers for FCC(Z)

### 4.3.3 Flow Characteristics of Octahedron and Octet Truss Lattice Structures

An Octet Truss unit cell encloses an Octahedron unit cell by various inclined struts, as seen previously in Table 3.1 in Chapter 3. Thus, the Octet Truss unit cell contains the Octahedron unit cell but is of a smaller size as compared to the standalone Octahedron unit cell. Figure 4.9 shows that Octet Truss lattice structures give more pressure drop as compared to the pressure drop observed across Octahedron lattice structures. This is because:

1. Octet Truss lattice structures have more number of struts as compared to that of Octahedron lattice structures. These extra number of struts become obstructions to the air-flow path.
2. In Octet Truss lattice structures, the volume of the air-flow path is less causing more pressure drop. This air-flow path volume is more in Octahedron lattice structures as compared to that in Octet Truss lattice structures.

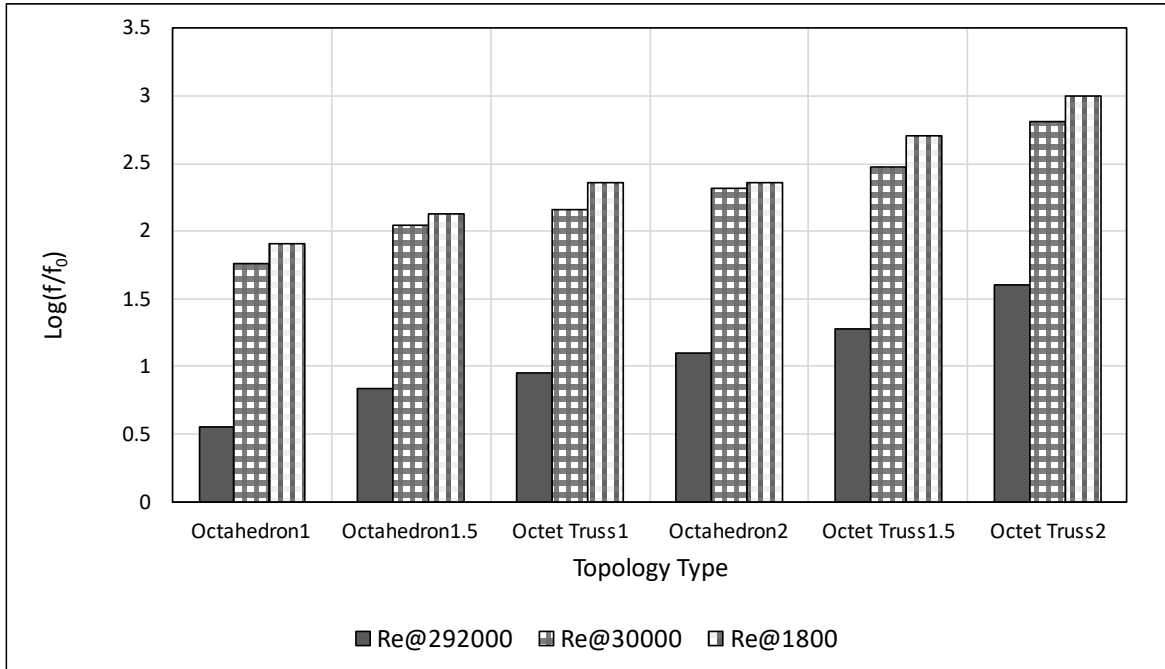


Figure 4.9 Friction factor augmentation ( $f/f_0$ ) across three different Reynold's numbers for Octet Truss and Octahedron

Thus, the air-flow path is an important parameter in investigating the friction factor values of lattice structures. And air-flow path depends mainly on the two-dimensional characteristics of the lattice structures: orientation of the struts and diameter of the struts. Furthermore, parameter like Reynold's number also affects the values of the friction factor.

#### 4.3.4 Flow Characteristics of Surface-Based Lattice Structures

The flow characteristics of surface-based TPMS lattice structures are shown in Figure 4.10. It can be seen that:

1. There is an average increase of 34% in augmented friction factor values for TPMS Diamond lattice structures as compared to the values of augmented friction factor for TPMS Gyroid lattice structures. This implies that the air-flow path in TPMS Gyroid lattice structures is less complicated in shape as compared to that in TPMS Diamond lattice structures.
2. The average increase in augmented friction factor values due to increasing the surface thickness is 69%.
3. Thus, increasing the surface thickness of TPMS lattice structures has a more predominant effect on augmented friction factor as compared to the effect caused by their shape.

4. Augmented friction factor values across surface-based TPMS lattice structures are more than those across strut-based lattice structures.

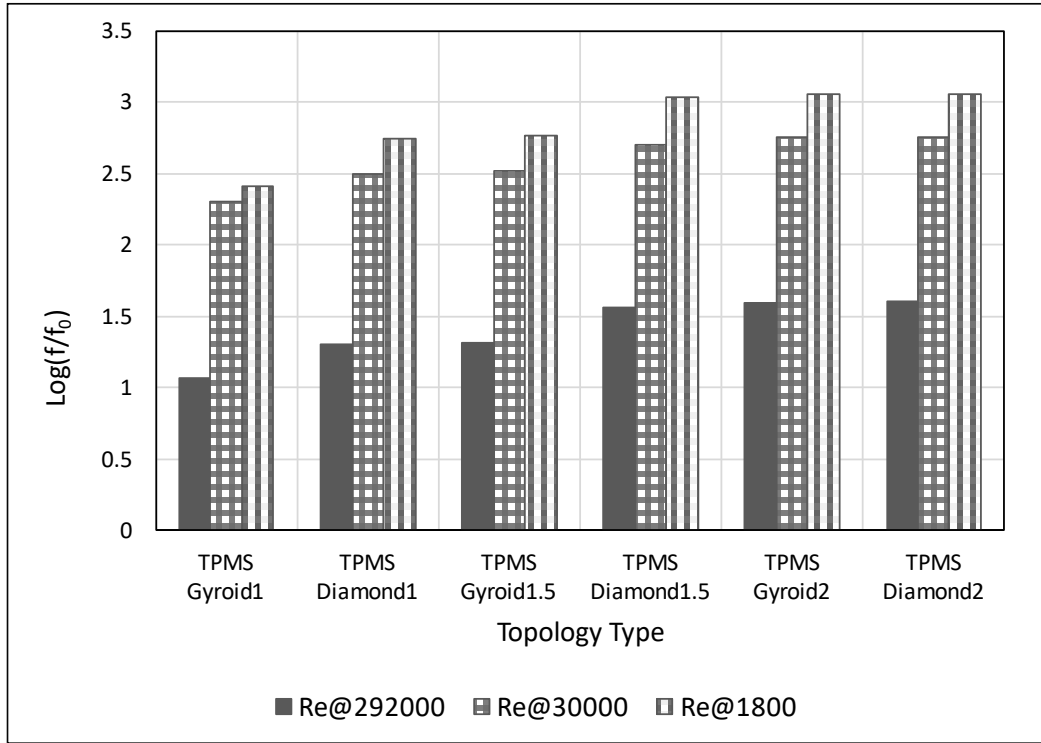


Figure 4.10 Friction factor augmentation ( $f/f_0$ ) across three different Reynold's numbers for Surface-based lattice structures

To benchmark the values of the augmented friction factor, TPMS structures

(Figure 4.11) are compared to those obtained in experiments carried out by Catchpole-Smith [55] (Figure 4.12) to verify the accuracy of the simulation.

1. Figure 4.11 shows that the values of augmented friction factor across surface-based TPMS lattice structures are in the range of 100-600 at Reynold's Number of 30000, and this range agrees with the experimental results shown in Figure 4.12.
2. Also, the trend that on increasing Reynold's number, the values augmented friction factor decreases also agrees with the experiments.

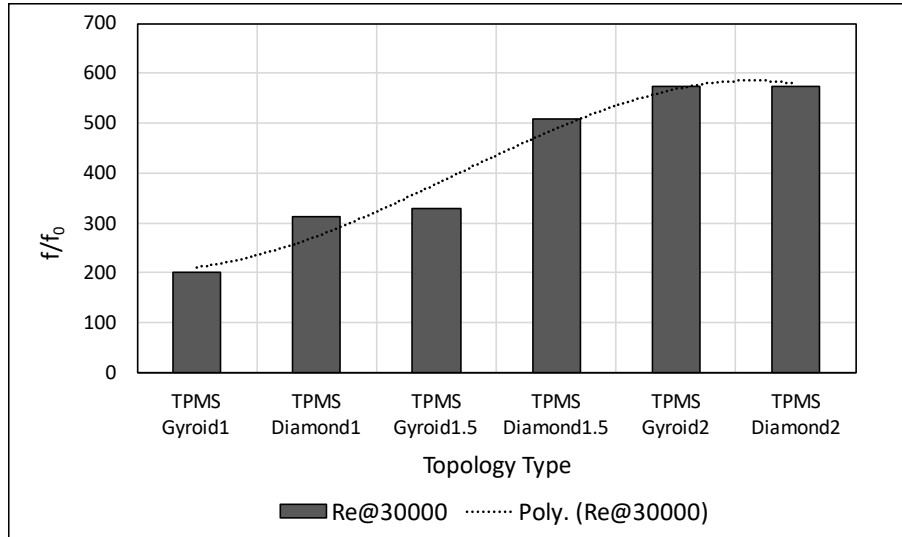


Figure 4.11 Friction Factor augmentation ( $f/f_0$ ) @Re=30000 for benchmarking the results

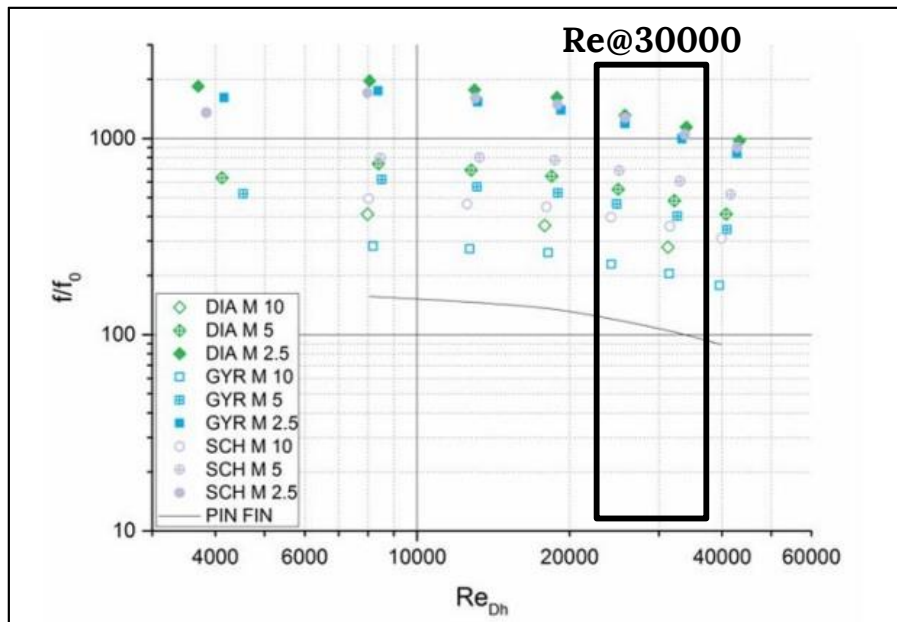


Figure 4.12 Friction factor augmentation ( $f/f_0$ ) across the Reynolds number range. [55]

This benchmarking validates the following points for the simulation setup:

1. The surface repair and mesh convergence study are accurately producing the results because the final output parameters from the simulation are comparable with the experiments conducted by Catchpole-Smith [55].
2. The formulas used are also in accordance with the experiments by Catchpole-Smith [55].

## 4.4 Heat Transfer Characteristics

Two important factors in evaluating the heat transfer characteristics of lattice structures are the convective heat transfer coefficient and Nusselt's number. The following sections discuss them in detail.

### 4.4.1 Convective Heat Transfer Coefficient of Strut-Based Lattice Structures

It is discussed in Section 2.2 of Chapter 2 that the convective heat transfer coefficient depends on the flow regime, the geometry of the structures, the S/V ratio, fluid to wall temperature ratio, properties of the fluid, Reynold's number, and surface roughness. The thermal characteristics of strut-based and surface-based lattice structures are discussed individually. As seen from Figures 4.13, 4.14 and 4.15 the behaviour of strut-based lattice structures for all Reynold's numbers is not following any fixed trend because the convective heat transfer coefficient strongly depends on the fluid flow type (laminar or turbulent), followed by its dependency on dimensional characteristics of lattice structures. Thus, a different style of the graph is chosen to include the correct order of structures for their behaviour for different Reynold's Numbers.

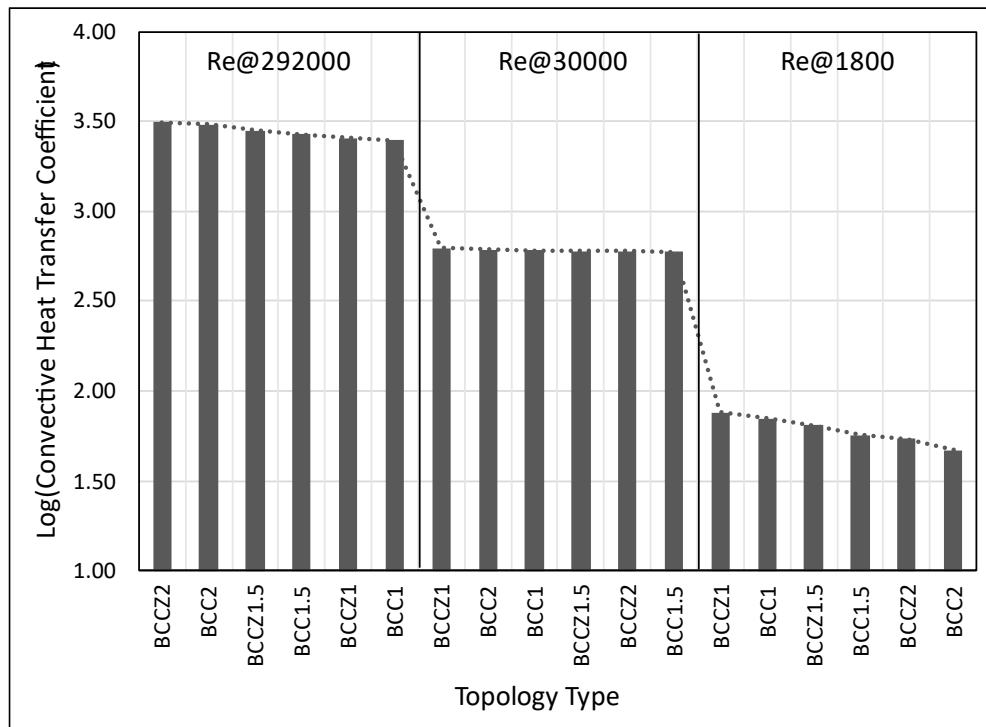


Figure 4.13 Convective HTC ( $W/(m^2-K)$ ) variation for BCC and BCCZ

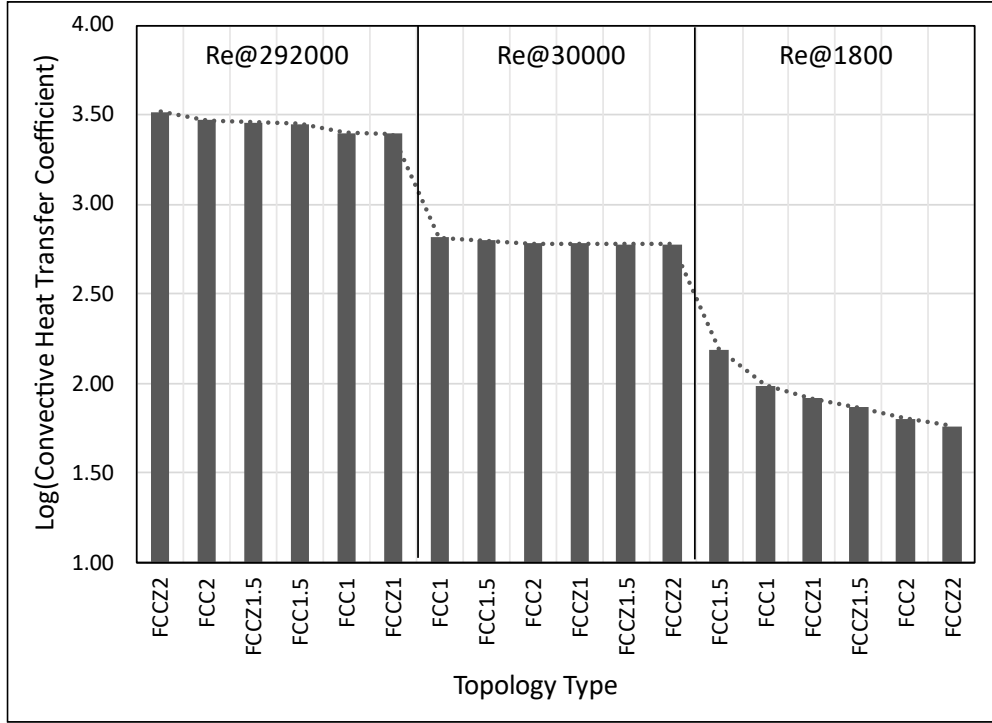


Figure 4.14 Convective HTC ( $W/(m^2-K)$ ) variation for FCC and FCCZ

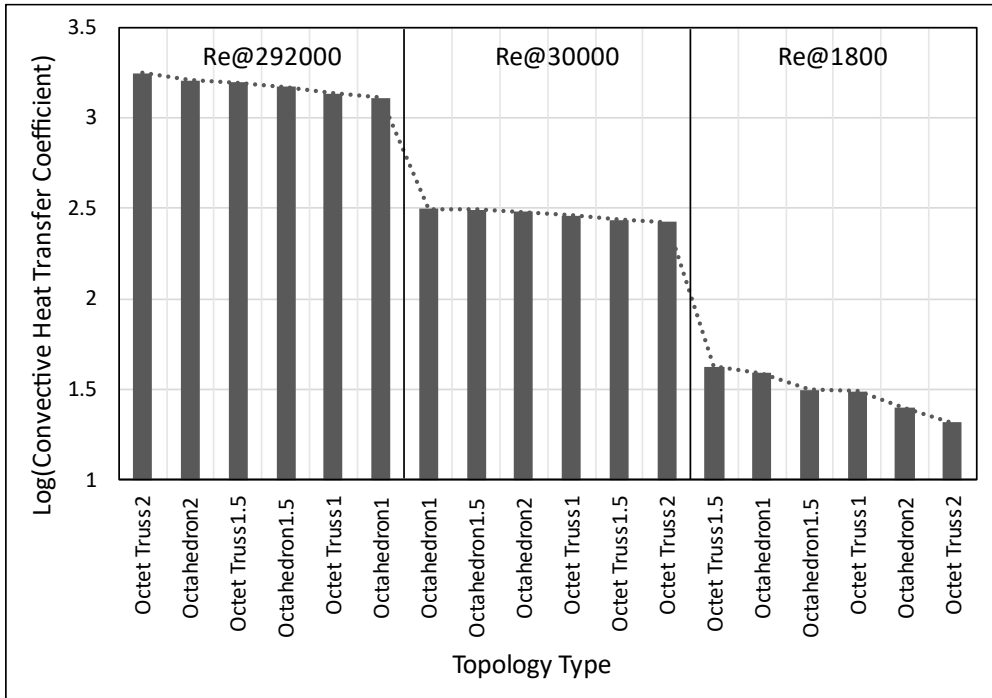


Figure 4.15 Convective HTC ( $W/(m^2-K)$ ) variation for Octahedron and Octet Truss

This behaviour can be shown with the help of Figure 4.16, and it shows that:

1. For high Reynold's (292,000), convection is mainly caused by intermixing of the air particles due to large turbulency causing eddies. After this, the surface area to volume ratio affects the convection within the air. This is also depicted by the polynomial (of order 6) trendline because it is wavier between the S/V ratio range of 1.78 to 4.7. Thus, convection is not fully dependent on the dimensional characteristics for highly turbulent flows.
2. For the less turbulent flow ( $Re=30,000$ ), both the S/V ratio and strut diameter/surface thickness influence the convective heat transfer coefficient. This is because the trendline (polynomial of order 6) is less wavy as compared to the trendline at Reynold's number 292,000.
3. For laminar flow ( $Re=1,800$ ), the polynomial trendline is the least wavy as compared to the other two flow regimes. Thus, convection depends on the S/V ratio for laminar flows, and they are directly proportional to each other (especially between the S/V range of 1.78 to 4.7). This is also because, in the laminar flows, there is no intermixing of the air. Moreover, the velocity of the air is further reduced due to the presence of shear drag at the boundary layers of lattice structures. Hence, convective heat transfer depends more on the dimensional properties of the lattice structures and less on the type of flow.
4. Due to the simple alignment of struts in Primitive lattice structures with a 1 mm strut diameter, the S/V ratio is the highest. Thus, there is a sudden increase in the CHT for these structures.
5. The relation between different Reynold's numbers and the CHT coefficient is proportional. This is because a highly turbulent flow gives more capability to the air for intermixing and recirculation. However, some intermixing and recirculation can also be caused by lattice structure geometry. And there is a sudden dip after TPMS Diamond and TPMS Gyroid lattice structures with a surface thickness of 2mm. This is because of the reduction in the size of the holes in the direction of the air-flow path. This gives more capability for intermixing and recirculation to the air.

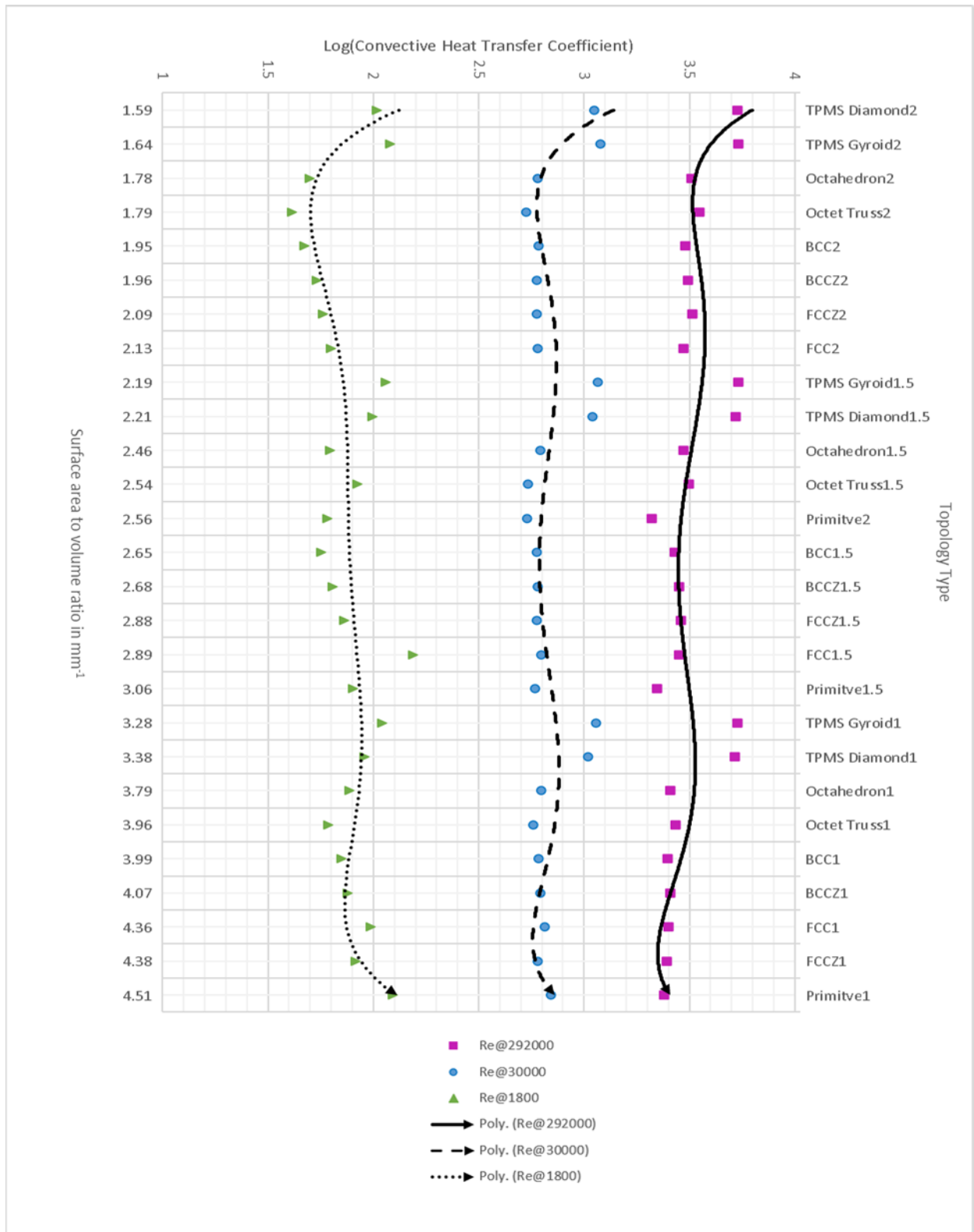


Figure 4.16 HTC ( $W/(m^2 \cdot K)$ ) variation with surface area to volume ratio ( $m^{-1}$ ) for different topologies

#### 4.4.2 Convective Heat Transfer Coefficient of Surface-Based Lattice Structures

For TPMS lattice structures, the trend is separately shown in the

Figure 4.17. It is seen that TPMS Gyroid gives better heat convection capability to air as compared to TPMS Diamond.

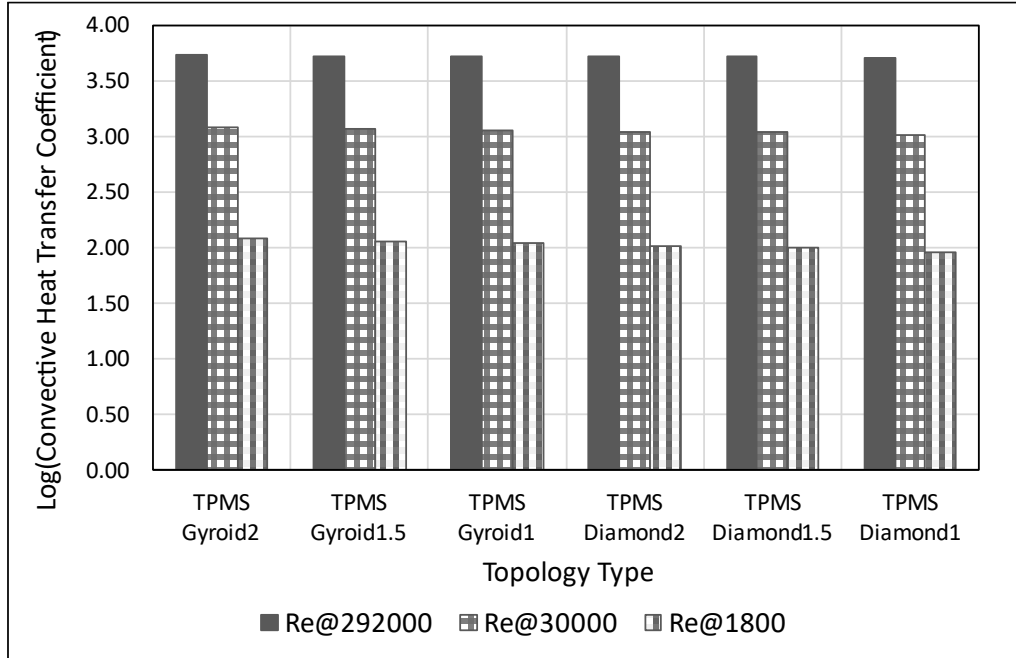


Figure 4.17 Convective HTC ( $W/(m^2 \cdot K)$ ) variation for surface-based lattice structures

However, there is not much difference between the values of convective HTC of TPMS Diamond and TPMS Gyroid because experiments conducted by Catchpole-Smith [55] show that, for TPMS lattice structures, the boundary layer effects dominate over the effects of the air-flow path across these lattice structures.

#### 4.4.3 Nusselt's Number for Benchmarking

The trend of Nusselt's number is the same as that obtained for the convective heat transfer coefficient because, according to Equation (2.7) Nu is obtained by dividing the convective heat transfer coefficient by the thermal conductivity of the air. However, to benchmark the heat transfer properties and simulation results, the values of Nusselt's number of all the TPMS geometries at Reynold's number of 30,000 are compared with the experiments conducted by Catchpole-Smith [55]. The range of values of Nu obtained from the simulation model is similar to the values obtained by experiments conducted, and it can be seen in Figures 4.18 and 4.19.

Thus, the following points from the simulation agree with the experimental results:

1. TPMS Gyroid is showing better heat transfer properties as compared to TPMS Diamond lattice structures, for a similar unit cell size and at  $Re=30,000$ .
2. The convective heat transfer coefficient decreases as Reynold's number decreases.
3. The diameter of the strut plays an important role in the same lattice structure topology type.

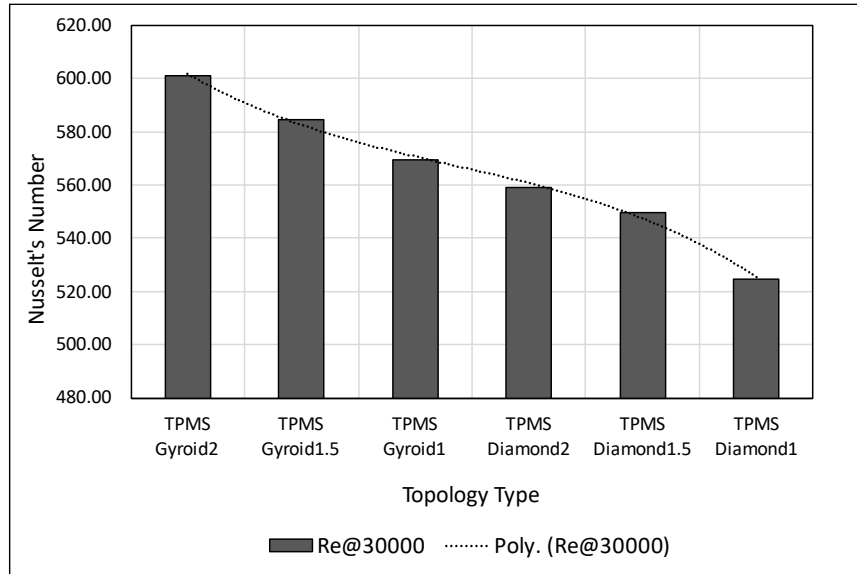


Figure 4.18 Nusselt's number values for benchmarking

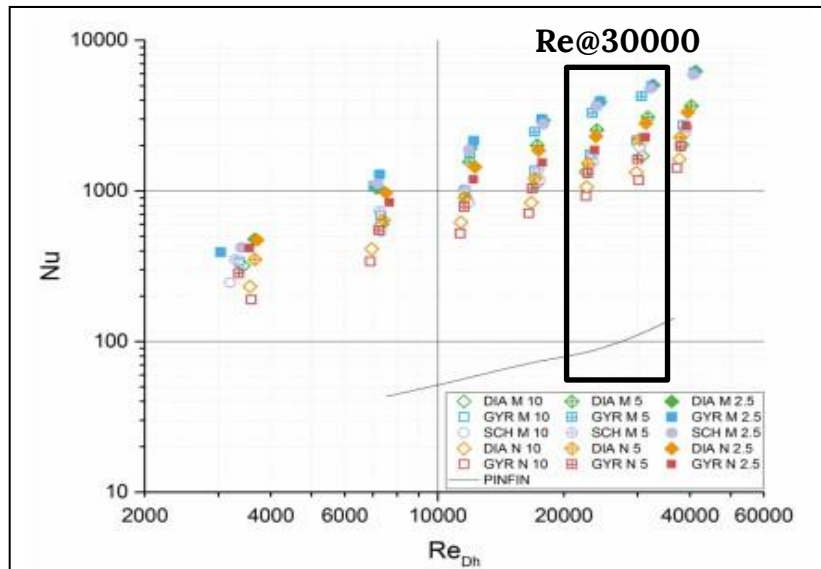


Figure 4.19 Nusselt's number for all lattice structure samples tested [55]

## 4.5 Flow and Thermal Property charts

After analyzing the results, the very last and most important step to completely correlate the flow properties with the thermal properties is to create a *flow and thermal property chart*. And its main advantage is discussed in Section 1.4 of Chapter 1. These charts help design engineers to choose the structures best suited for the operating conditions of the machines. Moreover, these charts become very important at a very high Reynold's number because:

1. Aerospace industries, for very high Reynold's number (here 292,000), can not incur the cost of experiments.
2. Lattice structures exhibit very different behaviour at high Reynold's number as compared to what they exhibit at lower Reynold's number. This is because convection highly depends on the flow regime and geometrical consideration becomes a secondary parameter that affects the convection.

A good structure must be the one which induces less pressure drop or less augmented friction factor and more heat transfer capability, i.e., a high convective heat transfer coefficient. Thus, plots between the convective heat transfer coefficient and the augmented friction factor for all the lattice structures of the same strut diameter or surface thickness can be seen in Figures 4.20, 4.21, 4.22, 4.23, 4.24, 4.25, 4.26, 4.27 and 4.28.

The behaviour of these lattice structures changes as Reynold's number changes. This behaviour is already explained by Figure 4.16 in Section 4.4.1 . The behaviour of strut-based lattice structures is more similar to surface-based lattice structures for the laminar flow. It is because the effect of the  $S/V$  ratio dominates the effect of the flow regime for laminar flow. Whereas for turbulent flow, it is the intermixing that dominates.

Thus, nine thermal and flow property charts are created. A design engineer can select a lattice structure at the optimum value where less friction factor is observed with a high convective heat transfer coefficient. However, this selection should also be based on constraints related to manufacturing, material and time taken to print a structure. These factors contribute to the cost of manufacturing.

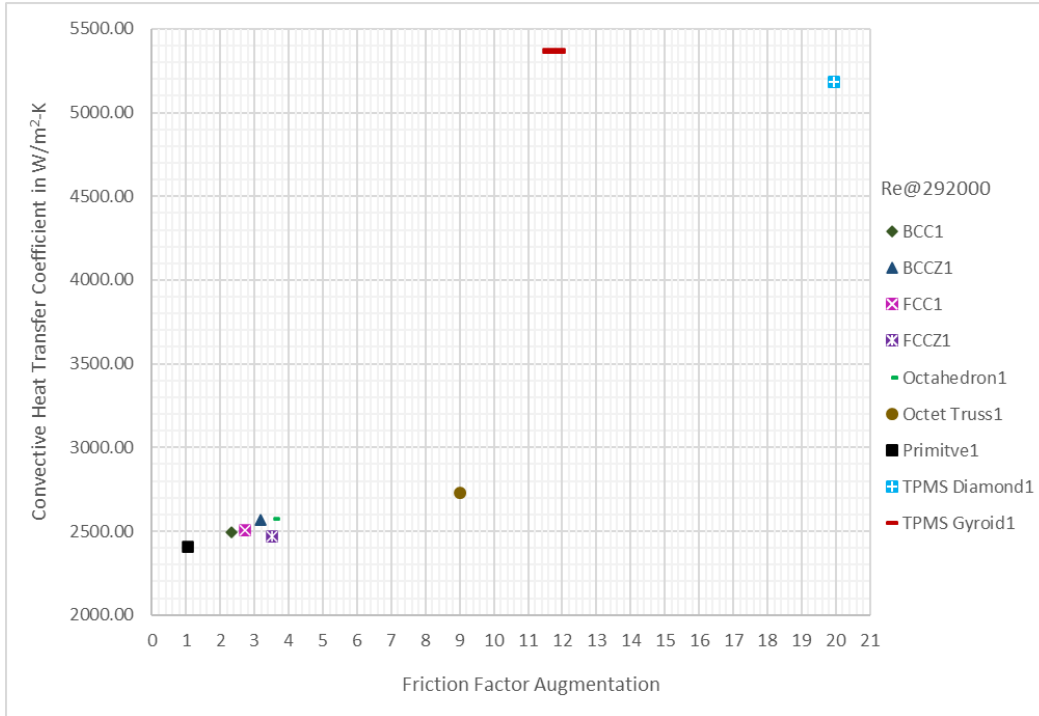


Figure 4.20 CHT( $W/m^2-K$ ) vs. Friction Factor Augmentation ( $f/f_0$ ) at Reynold's number 292,000 for strut diameter/surface thickness of 1 mm

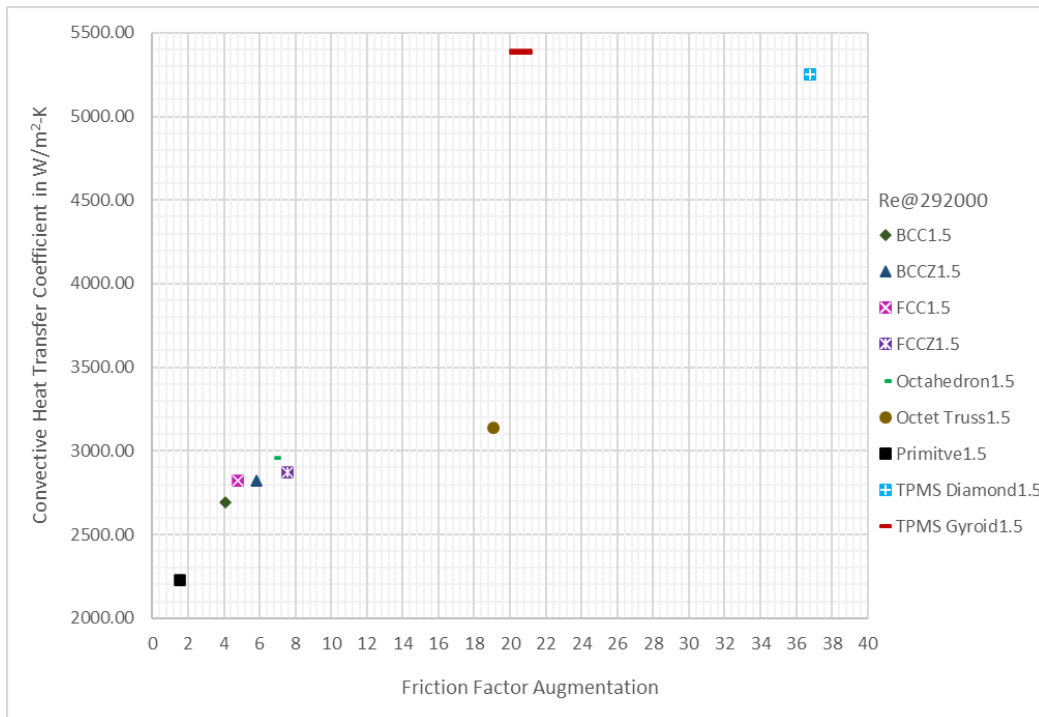


Figure 4.21 CHT( $W/m^2-K$ ) vs. Friction Factor Augmentation ( $f/f_0$ ) at Reynold's number 292,000 for strut diameter/surface thickness of 1.5 mm

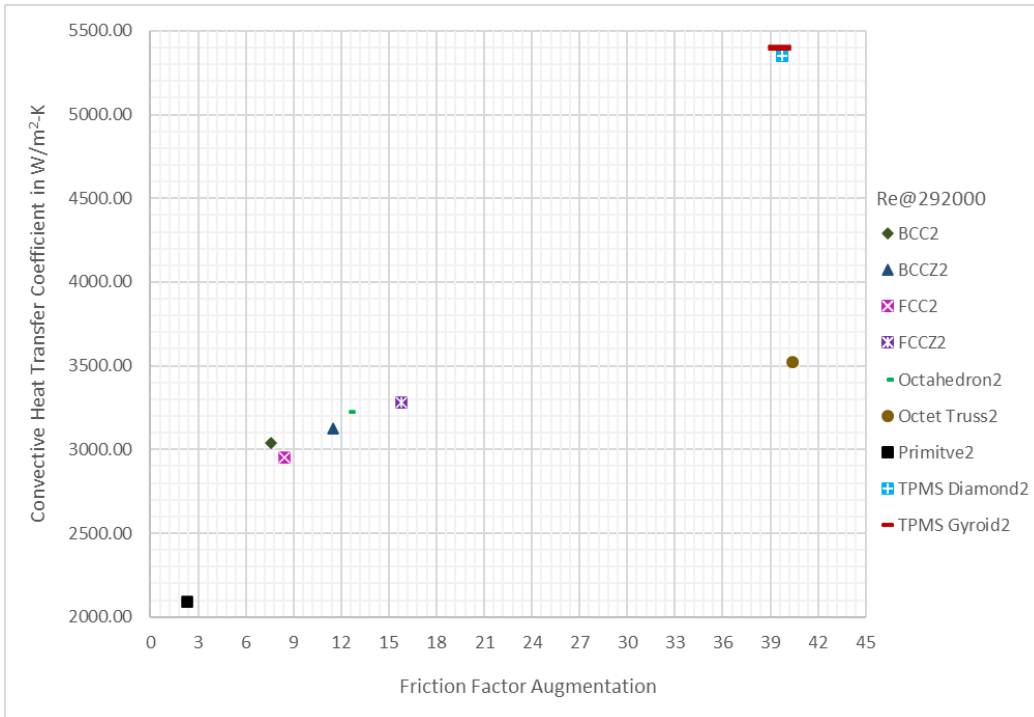


Figure 4.22 CHT( $W/m^2-K$ ) vs. Friction Factor Augmentation ( $f/f_0$ ) at Reynold's number 292,000 for strut diameter/surface thickness of 2 mm

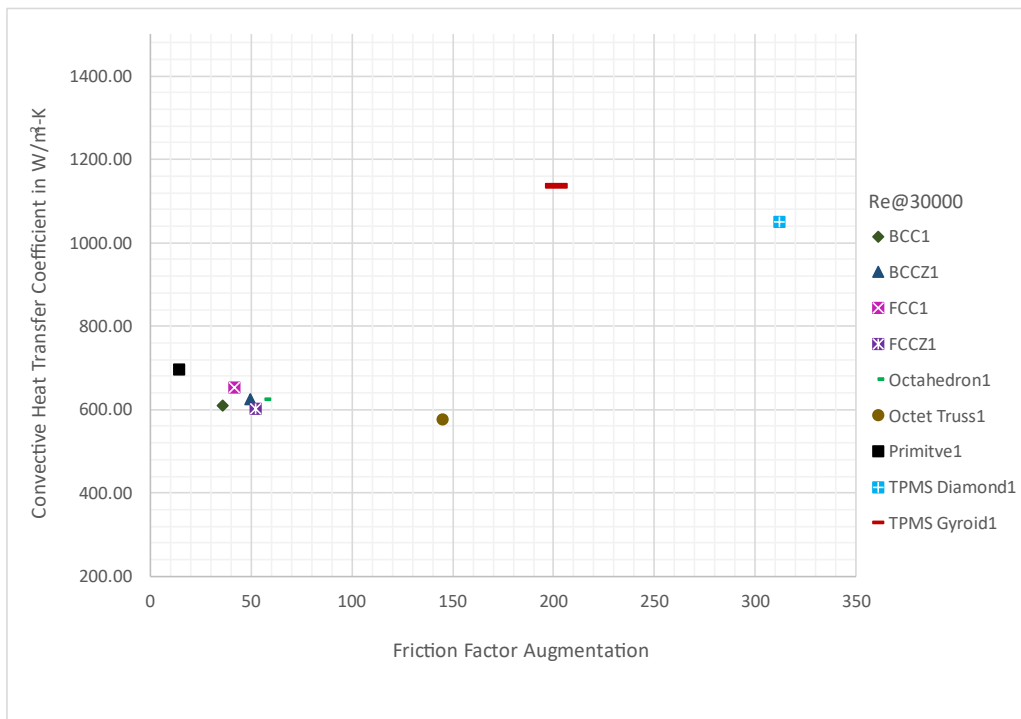


Figure 4.23 CHT( $W/m^2-K$ ) vs. Friction Factor Augmentation ( $f/f_0$ ) at Reynold's number 30,000 for strut diameter/surface thickness of 1 mm

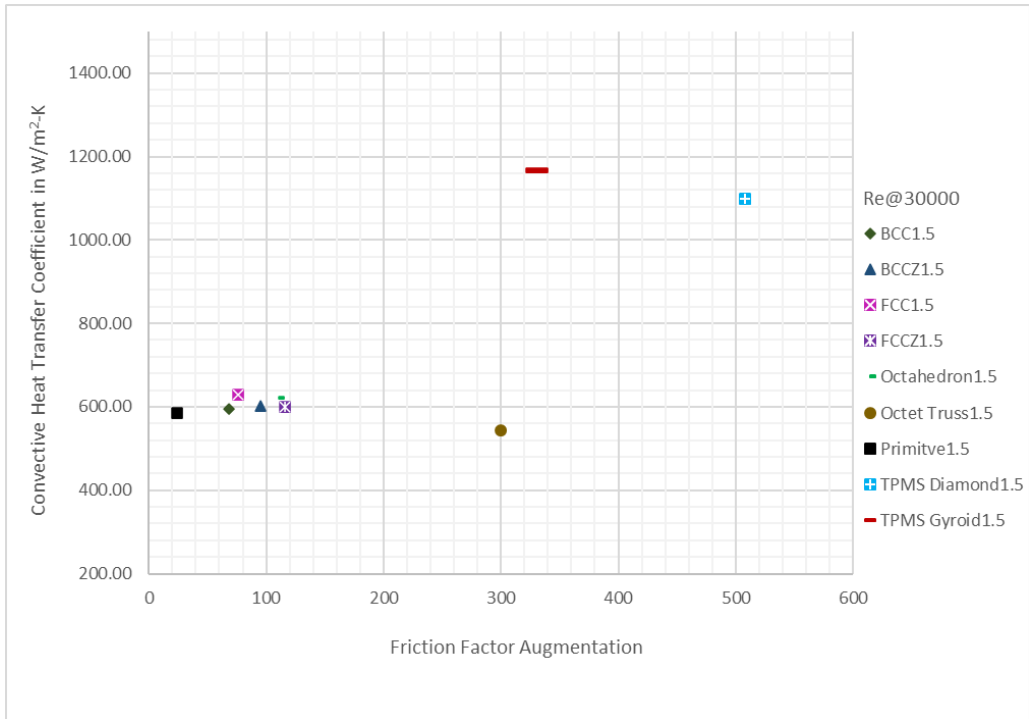


Figure 4.24 CHT( $W/m^2-K$ ) vs. Friction Factor Augmentation ( $f/f_0$ ) at Reynold's number 30,000 for strut diameter/surface thickness of 1.5 mm

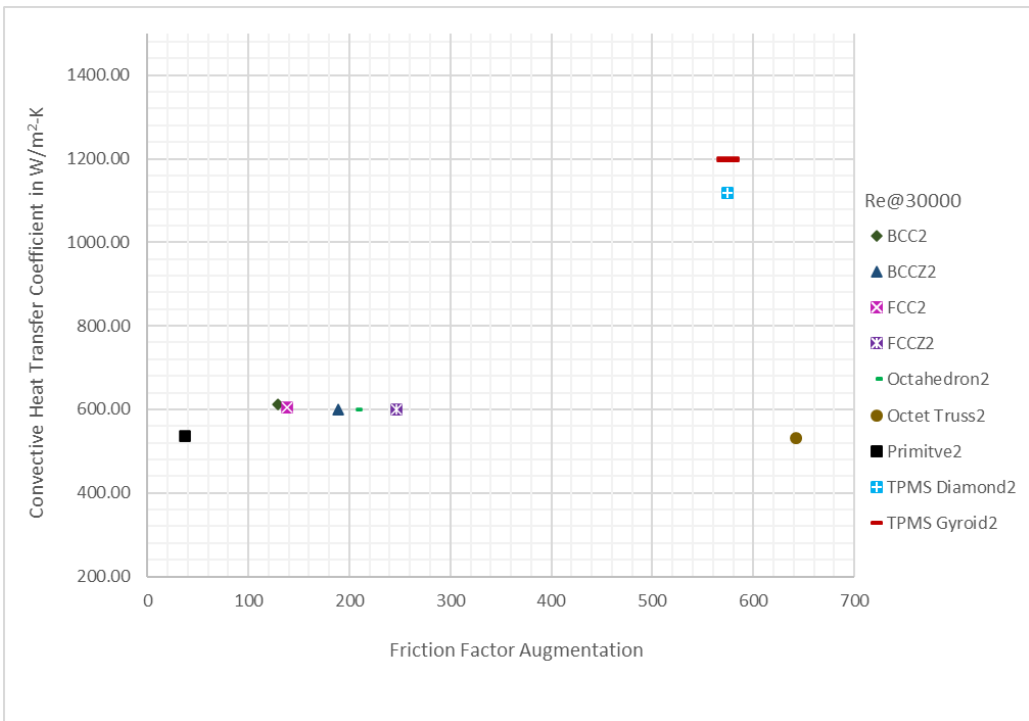


Figure 4.25 CHT( $W/m^2-K$ ) vs. Friction Factor Augmentation ( $f/f_0$ ) at Reynold's number 30,000 for strut diameter/surface thickness of 2 mm

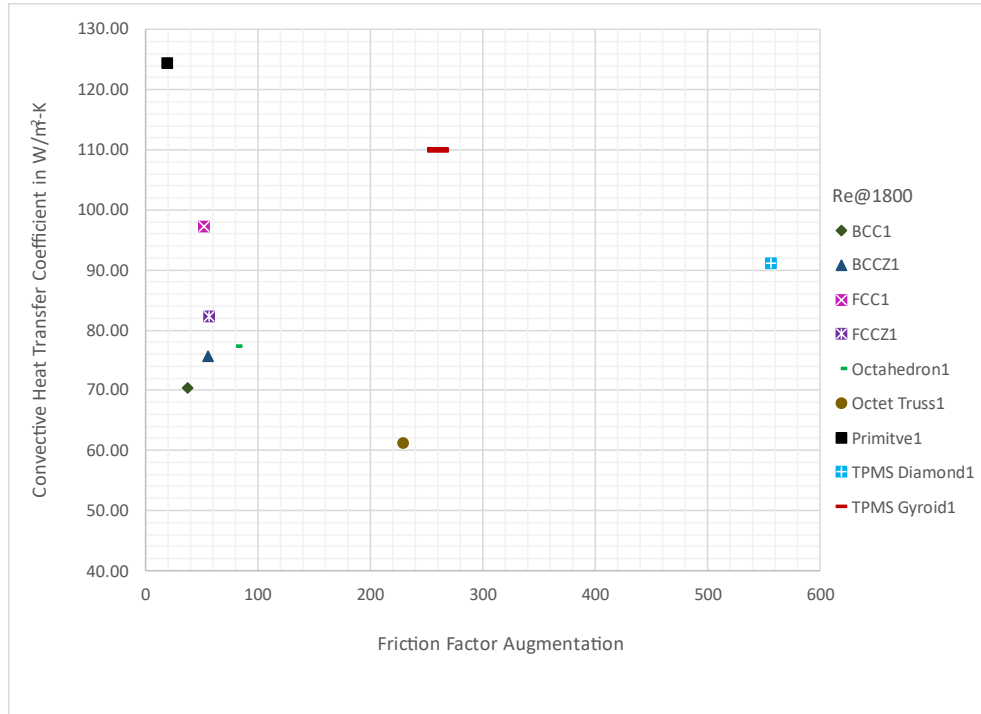


Figure 4.26 CHT( $W/m^2-K$ ) vs. Friction Factor Augmentation ( $f/f_0$ ) at Reynold's number 1,800 for strut diameter/surface thickness of 1 mm

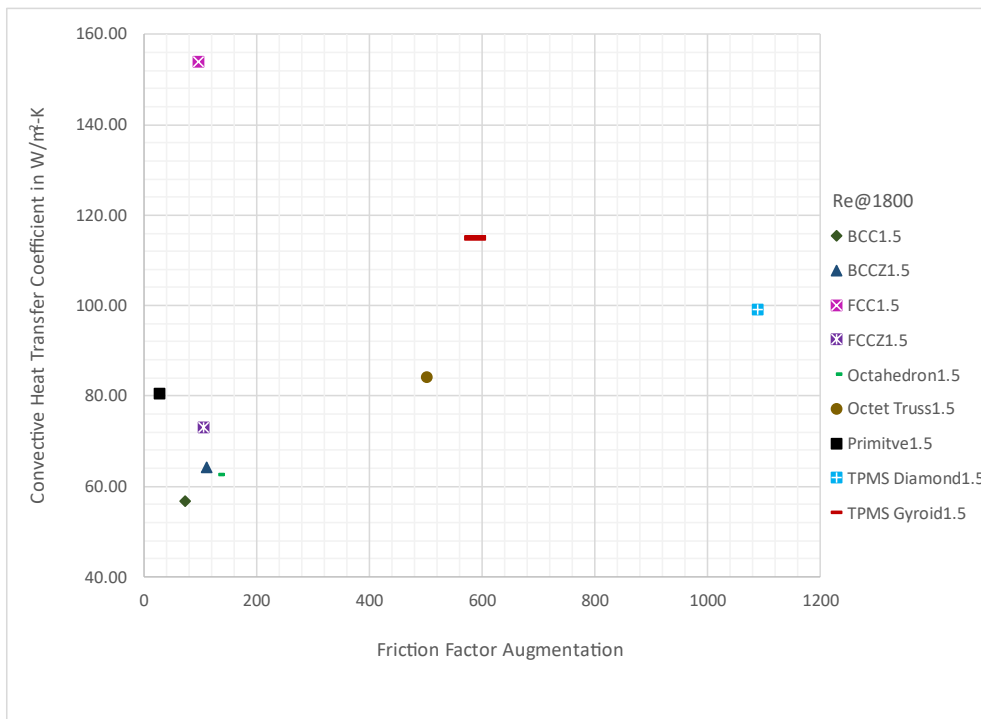


Figure 4.27 CHT( $W/m^2-K$ ) vs. Friction Factor Augmentation ( $f/f_0$ ) at Reynold's number 1,800 for strut diameter/surface thickness of 1.5 mm

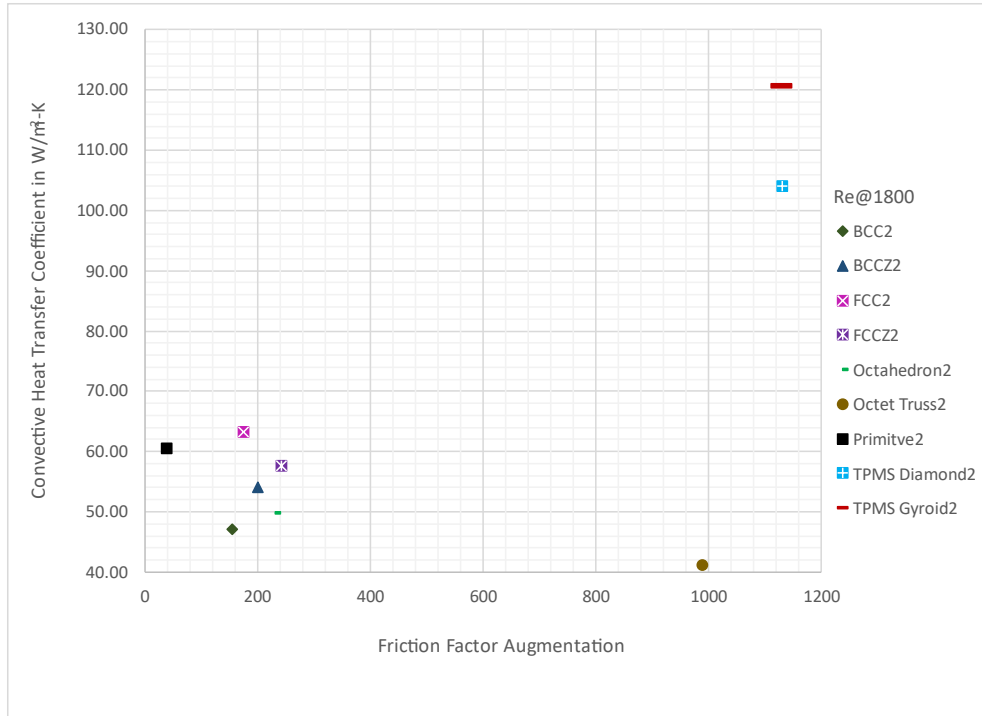


Figure 4.28 CHT( $W/m^2-K$ ) vs. Friction Factor Augmentation ( $f/f_0$ ) at Reynold's number 1,800 for strut diameter/surface thickness of 2 mm

## **Chapter 5: Conclusions and Future Work**

### **5.1 Conclusions**

This research investigated the flow and thermal behaviour of strut-based and surface-based lattice structures. It included the successful geometric modelling of strut-based and surface-based lattice structures, followed by mesh generation and its convergence study. The mesh convergence study signified that the surface repair tool worked accurately on the topologies which were modelled geometrically. Moreover, the results were independent of the element/base size of the mesh.

The results discussed in Chapter 4 demonstrated that the dimensional characteristics provided an approximate relation between porosity and surface area to volume ratio of lattice structures. And it was observed that they are directly proportional to each other. These dimensional characteristics were used to understand the flow and thermal characteristics of the lattice structures because these characteristics depend on the air-flow path.

Flow Characteristics signified that for the strut-based lattice structures, if the struts are aligned in the direction of the air-flow path, then the pressure loss is reduced as compared to when the struts are not in the direction of the air-flow path. This was evident by the introduction of perpendicular z-struts to BCC and FCC lattice structures. Moreover, the effect of increasing the strut diameter is more predominant than the effect of the orientation of the struts on the air-flow path. Similarly, for the surface-based TPMS lattice structures, the holes of the Gyroid are aligned with the air-flow path as compared to the holes of the Diamond. Thus, Gyroid for a particular thickness induces less friction factor.

Convective heat transfer coefficient either depends on the type of flow (laminar, turbulent, or highly turbulent flow) or on the geometrical aspects of the lattice structures (here, surface area to volume ratio) or on both. For highly turbulent flow, the properties of the flow dominate due to better intermixing of air particles. Whereas for turbulent flow, it depends on both of these factors. And for the laminar flow, it highly depends on the surface area to volume ratio. However, the complex shape of the TPMS lattice structure topologies gives the flow better capability to intermix and recirculate.

After analyzing the flow and thermal characteristics of lattice structures, they were combined to generate suitable flow and property charts for the selection of lattice structure topologies at a given

operating condition. The topology with less pressure drop/friction factor and high convective heat transfer coefficient is suitable for gas turbine engines. Furthermore, at the high Reynold's number, surface-based lattice structures give the best heat transfer coefficient as compared to strut-based lattice structures but at the expense of a large pressure drop. Also, it was observed that between the surface-based lattice structures, Gyroid is a better choice because it has better heat transfer performance with lesser pressure drop. And in the case of strut-based structures, this trend is shown by FCC and FCCZ structures.

The results are in agreement with the experiments conducted by Catchpole-Smith [55].

## **5.2 Future Scope**

The future scope of this research can be divided into two parts. And they can help in creating more comprehensive flow and thermal property charts for lattice structures.

1. The first part covers the methods which can help to narrow down the results of geometric modelling and simulation, and it includes the following three points:
  - 1.1 Defining one platform where all types of lattice structure topologies can be designed.
  - 1.2 Investigating the effects of other dimensional parameters like inclination of struts with respect to each other or curvature of the surfaces on flow and thermal characteristics of lattice structures.
  - 1.3 Investigating the results in a conjugated heat transfer environment by introducing the conduction through different types of materials for lattice structures.
2. The second part covers the possible future research direction, and it includes the following points:
  - 2.1 Defining a reverse methodology where for a given flow and thermal property, the topology of the lattice structures can be optimized.
  - 2.2 Identifying suitable AM fabrication processes for complex lattice structures.
  - 2.3 Designing deep neural networks (or other predictive algorithms) which can learn and predict the behaviour of stochastic lattice structures or more bio-inspired cellular solids from the database generated by modelling and simulation of the non-stochastic lattice structures.

## Appendix A

Author	Topology Type
[56]	Diamond
[19]	Cubic, Diamond, Truncated Cube, Truncated Cuboctahedron, Rhombic Dodecahedron, Rhombicuboctahedron
[57]	Octet-Truss
[58]	TPMS Gyroid
[59]	TPMS Gyroid, TPMS Diamond
[60]	FCCZ
[61]	Rhombic Dodecahedron
[62]	Cubic
[63]	Octet-Truss
[64]	Octet-Truss
[65]	BCC, BCCZ, F2BCC
[66]	Cubic, BCC
[67]	Rhombic Dodecahedron
[68]	Octahedron, Rhombic Dodecahedron
[69]	Octet-Truss
[70]	Cubic, Rhombic Dodecahedron, Diamond, Truncated Octahedron
[71]	Diamond
[72]	TPMS Gyroid, TPMS Diamond
[21]	BCC, BCCZ, FCC, FCCZ, F2BCC
[73]	BCC, BCCZ
[74]	BCCZ
[75]	Rhombic Dodecahedron
[76]	BCC, FCC, F2BCCZ
[77]	BCC, BCCZ
[78]	BCC
[79]	BCC

<b>Author</b>	<b>Topology Type</b>
[80]	Rhombic Dodecahedron
[81]	Diamond
[82]	Cubic
[83]	BCC
[84]	CC, FCCZ, BCC, BCCZ, F2BCC, F2BCCZ
[85]	Cubic
[86]	BCC, BCCZ
[87]	BCC, BCCZ
[88]	Octet-Truss
[89]	Octet-Truss
[90]	BCC
[91]	Diamond
[32]	Diamond
[92]	Rhombic Dodecahedron
[93]	TPMS Gyroid
[94]	TPMS Gyroid
[95]	TPMS Gyroid
[96]	Cubic, Diamond, Truncated Cube, Truncated Cuboctahedron, Rhombic Dodecahedron, Rhombicuboctahedron, Truncated Octahedron, Octahedron, BCC, FCC
[97]	Cubic, TPMS Gyroid
[28]	Cubic, Rhombic Dodecahedron
[21]	BCC, BCCZ, FCC, FCCZ
[98]	Rhombic Dodecahedron
[99]	BCC
[100]	Cubic, Diamond, Rhombic Dodecahedron, Truncated Octahedron
[65]	BCC
[101]	Cubic, Truncated Octahedron, Rhombic Dodecahedron, Diamond

<b>Author</b>	<b>Topology Type</b>
[70]	Rhombicuboctahedron
[102]	Truncated Cube
[103]	Truncated Cuboctahedron
[104]	Octahedron
[71]	Diamond
[21]	Rhombic Dodecahedron
[105]	Rhombic Dodecahedron
[106]	Cubic, Rhombic Dodecahedron
[107]	BCC
[108]	TPMS Diamond
[108]	TPMS Gyroid
[109]	TPMS Gyroid
[110]	TPMS Gyroid
[111]	BCC
[112]	Truncated Octahedron
[113]	Metal Foams (V strut, H strut)
[3]	Metal Foams

## Appendix B

Equation	Symbol	Physical quantity	Unit
(2.2)	$\rho$	Relative Density	$\text{Kg/m}^3$
(2.2)	$\rho_s$	Density of the solid core	$\text{Kg/m}^3$
(2.2)	$\bar{\rho}$	Density of the lattice structure core	$\text{Kg/m}^3$
(2.2)	$V_s$	Volume of the solid core	$\text{m}^3$
(2.2)	$V_L$	Volume of the lattice structure core	$\text{m}^3$
(2.3)	$\phi$	Porosity	-
-	L	Strut length	mm
-	D	Strut Diameter	mm
(2.4)	$\bar{\lambda}$	Total thermal conductivity	$\text{W/m}\cdot\text{K}$ or $\text{W/m}\cdot\text{K}$ or $\text{Wm}^{-1}\text{K}^{-1}$
(2.4)	$\lambda_s$	Solid thermal conductivity	$\text{W/m}\cdot\text{K}$ or $\text{W/m}\cdot\text{K}$ or $\text{Wm}^{-1}\text{K}^{-1}$
(2.4)	$\lambda_g$	Thermal conductivity withing the gases	$\text{W/m}\cdot\text{K}$ or $\text{W/m}\cdot\text{K}$ or $\text{Wm}^{-1}\text{K}^{-1}$
(2.5)	$U_0$	Overall heat transfer coefficient	$\text{W/m}^2\cdot\text{K}$ or $\text{W/m}^2\cdot\text{K}$ or $\text{Wm}^{-2}\text{K}^{-1}$
(2.5)	$\dot{Q}$	Rate of heat transfer	W
(2.5)	A	Overall heat transfer area	$\text{m}^2$
(2.5)	$\Delta T$	Overall temperature difference	K
(2.6)	h	Convective heat transfer coefficient	$\text{W/m}^2\cdot\text{K}$ or $\text{W/m}^2\cdot\text{K}$ or $\text{Wm}^{-2}\text{K}^{-1}$
-	$v_f$	Fluid velocity	m/s
(2.7)	l	Characteristic length of the fluid domain	m
(2.7)	Nu	Nusselt's number	-
(2.7)	k	Thermal conductivity of the fluid	$\text{W/m}\cdot\text{K}$ or $\text{W/m}\cdot\text{K}$ or $\text{Wm}^{-1}\text{K}^{-1}$
(2.8)	$\Delta P$	Pressure loss	Pa
(2.8)	f	Friction factor	-

<b>Equation</b>	<b>Symbol</b>	<b>Physical quantity</b>	<b>Unit</b>
(2.8)	V	Mean flow velocity	m/s
(2.8)	d	Diameter of the flow domain	mm
(2.9)-(2.11)	$f_0$	Friction factor of hydraulically smooth channel	-
(2.9)-(2.11)	Re	Reynold's number	-
(3.1),(3.2)	x, y, z	Cartesian coordinates	-
(3.1),(3.2)	X, Y, Z	Thickness related constants in x, y and z directions respectively	-
(3.1),(3.2)	C	Curvature constant	-
(3.3)	$k_t$	Turbulent kinetic energy	J/Kg
(3.3)	U	Mean turbulent velocity	m/s
(3.4)	I	Turbulent Intensity	-
(3.5)	$u'$	Root mean square of the turbulent velocity fluctuations	m/s
(3.7)	$\omega$	Specific turbulent dissipation rate	$s^{-1}$
(3.7)	$C_\mu$	Turbulence model constant	-
(3.7)	$l_t$	Turbulent length scale	m
(3.8)	$\nu_t$	Turbulent viscosity	$Kgm^{-1}s^{-1}$
-	S/V	Surface area to volume ratio	$mm^{-1}$

## References

1. Alvarez, A. *Subtractive Manufacturing: Past, Present, and Future*. 2022 [cited 2022 26th July]; Available from: [https://ketiv.com/blog/subtractive-manufacturing-past-present-and-future/#:~:text=Whether%20you're%20milling%20wood,numerical%20control%20\(NC\)%20machines.](https://ketiv.com/blog/subtractive-manufacturing-past-present-and-future/#:~:text=Whether%20you're%20milling%20wood,numerical%20control%20(NC)%20machines.)
2. Markforged. *Additive Manufacturing History: From the 1980's to Now*. 2022 [cited 2022 26th July]; Available from: <https://markforged.com/de/resources/blog/additive-manufacturing-history-from-the-1980s-to-now>.
3. Mancin, S., et al., *Experimental air heat transfer and pressure drop through copper foams*. *Experimental thermal and fluid science*, 2012. **36**: p. 224-232.
4. González, C.M. *Infographic: The History of 3D Printing*. 2020 [cited 2022 26th July]; Available from: <https://www.asme.org/topics-resources/content/infographic-the-history-of-3d-printing>.
5. Reddy, K.S., *ADDITIVE MANUFACTURING TECHNOLOGIES*. *BEST: International Journal of Management, Information Technology and Engineering (BEST: IJMITE)*, 2016. **4**(7): p. 89-112.
6. Reddy, K.S. and S. Dufera, *Additive manufacturing technologies*. *Int. J. of Man., Inf., Tech. and Eng*, 2016. **4**(7): p. 89-112.
7. Park, K.-M., K.-S. Min, and Y.-S. Roh, *Design Optimization of Lattice Structures under Compression: Study of Unit Cell Types and Cell Arrangements*. *Materials*, 2021. **15**(1): p. 97.
8. Varotsis, A.B. *Guide to Lattice Structures in Additive Manufacturing*. 2022 [cited 2022 29th July]; Available from: <https://ntopology.com/blog/guide-to-lattice-structures-in-additive-manufacturing/#:~:text=Simply%20put%2C%20lattice%20structures%20are,an%20ordered%20or%20stochastic%20pattern.>
9. *Rethinking foam—the Carbon lattice innovation*. 2022 [cited 2022 August 1st]; Available from: <https://www.carbon3d.com/resources/whitepaper/rethinking-foam-carbons-lattice-innovation>.
10. Kawasaki. *About Gas Turbines*. 2022 [cited 2022]; Available from: [https://global.kawasaki.com/en/energy/equipment/gas\\_turbines/outline.html](https://global.kawasaki.com/en/energy/equipment/gas_turbines/outline.html).
11. ANSYS. *Material property charts*. ANSYS Granta @ 2020 Granta Design 2020 [cited 2022; Available from: <https://www.grantadesign.com/education/students/charts/>.

12. Ashby, M.F., *The properties of foams and lattices*. Philosophical Transactions of the Royal Society A: Mathematical, Physical and Engineering Sciences, 2006. **364**(1838): p. 15-30.
13. Alghamdi, A., et al., *Effect of additive manufactured lattice defects on mechanical properties: an automated method for the enhancement of lattice geometry*. The International Journal of Advanced Manufacturing Technology, 2020. **108**(3): p. 957-971.
14. Schwarz, H.A., *Gesammelte mathematische abhandlungen*. Vol. 260. 1972: American Mathematical Soc.
15. Köhnen, P., et al., *Mechanical properties and deformation behavior of additively manufactured lattice structures of stainless steel*. Materials & Design, 2018. **145**: p. 205-217.
16. Maskery, I., et al., *Compressive failure modes and energy absorption in additively manufactured double gyroid lattices*. Additive Manufacturing, 2017. **16**: p. 24-29.
17. Maconachie, T., et al., *SLM lattice structures: Properties, performance, applications and challenges*. Materials & Design, 2019. **183**: p. 108137.
18. Gibson, L.J., M.F. Ashby, and B.A. Harley, *Cellular materials in nature and medicine*. 2010: Cambridge University Press.
19. Ahmadi, S.M., et al., *Additively manufactured open-cell porous biomaterials made from six different space-filling unit cells: The mechanical and morphological properties*. Materials, 2015. **8**(4): p. 1871-1896.
20. Kadkhodapour, J., et al., *Failure mechanisms of additively manufactured porous biomaterials: Effects of porosity and type of unit cell*. Journal of the mechanical behavior of biomedical materials, 2015. **50**: p. 180-191.
21. Leary, M., et al., *Inconel 625 lattice structures manufactured by selective laser melting (SLM): Mechanical properties, deformation and failure modes*. Materials & Design, 2018. **157**: p. 179-199.
22. Liu, L., et al., *Elastic and failure response of imperfect three-dimensional metallic lattices: the role of geometric defects induced by Selective Laser Melting*. Journal of the Mechanics and Physics of Solids, 2017. **107**: p. 160-184.
23. Hitzler, L., et al., *Direction and location dependency of selective laser melted AlSi10Mg specimens*. Journal of Materials Processing Technology, 2017. **243**: p. 48-61.
24. Quevedo González, F.J. and N. Nuño, *Finite element modelling approaches for well-ordered porous metallic materials for orthopaedic applications: cost effectiveness and geometrical considerations*. Computer methods in BiomeChaniCs and BiomedicaCal engineering, 2016. **19**(8): p. 845-854.

25. Xue, Y., et al., *Compressive property of Al-based auxetic lattice structures fabricated by 3-D printing combined with investment casting*. Materials Science and Engineering: A, 2018. **722**: p. 255-262.
26. Yang, H. and L. Ma, *Design and characterization of axisymmetric auxetic metamaterials*. Composite Structures, 2020. **249**: p. 112560.
27. Zargarian, A., et al., *On the fatigue behavior of additive manufactured lattice structures*. Theoretical and Applied Fracture Mechanics, 2019. **100**: p. 225-232.
28. Zhao, S., et al., *The influence of cell morphology on the compressive fatigue behavior of Ti-6Al-4V meshes fabricated by electron beam melting*. Journal of the mechanical behavior of biomedical materials, 2016. **59**: p. 251-264.
29. Zhang, X., et al., *Selective electron beam manufactured Ti-6Al-4V lattice structures for orthopedic implant applications: Current status and outstanding challenges*. Current Opinion in Solid State and Materials Science, 2018. **22**(3): p. 75-99.
30. Yavari, S.A., et al., *Relationship between unit cell type and porosity and the fatigue behavior of selective laser melted meta-biomaterials*. Journal of the mechanical behavior of biomedical materials, 2015. **43**: p. 91-100.
31. Zadpoor, A.A., *Mechanical performance of additively manufactured meta-biomaterials*. Acta biomaterialia, 2019. **85**: p. 41-59.
32. Wauthle, R., et al., *Effects of build orientation and heat treatment on the microstructure and mechanical properties of selective laser melted Ti6Al4V lattice structures*. Additive Manufacturing, 2015. **5**: p. 77-84.
33. Narkhede, S. and A. Sur, *Performance prediction of hollow micro-lattice cross-flow heat exchanger using a numerical approach*. International Journal of Ambient Energy, 2021: p. 1-8.
34. Calmidi, V.V. and R.L. Mahajan, *Forced convection in high porosity metal foams*. J. Heat Transfer, 2000. **122**(3): p. 557-565.
35. Lu, T., *Heat transfer efficiency of metal honeycombs*. International Journal of Heat and Mass Transfer, 1999. **42**(11): p. 2031-2040.
36. Deng, H., J. Zhao, and C. Wang, *Leaf Vein-Inspired Bionic Design Method for Heat Exchanger Infilled with Graded Lattice Structure*. Aerospace, 2021. **8**(9): p. 237.
37. Lu, T., H.A. Stone, and M. Ashby, *Heat transfer in open-cell metal foams*. Acta materialia, 1998. **46**(10): p. 3619-3635.
38. Kim, T., et al., *Convective heat dissipation with lattice-frame materials*. Mechanics of Materials, 2004. **36**(8): p. 767-780.

39. Ho, J., K. Leong, and T. Wong, *Experimental and numerical investigation of forced convection heat transfer in porous lattice structures produced by selective laser melting*. International Journal of Thermal Sciences, 2019. **137**: p. 276-287.
40. Kaur, I. and P. Singh, *Conjugate heat transfer in lattice frame materials based on novel unit cell topologies*. Numerical Heat Transfer, Part A: Applications, 2022: p. 1-14.
41. Petrock, S. *Simulation Makes Meshing Easy. Too Easy?* 2020 [cited 2022; Available from: <https://www.engineersrule.com/solidworks-simulation-makes-meshing-easy-too-easy/>].
42. idealsimulations. *CFD Computational Domain*. 2020 [15th August 2022]; Available from: <https://www.idealsimulations.com/resources/cfd-computational-domain/>.
43. Allison, C. *Meshing in FEA: Introduction to meshing* 2020; Available from: <https://onscale.com/blog/meshing-in-fea-introduction-to-meshing/>.
44. team, M. *All there is to know about different mesh types in CFD!* 2016 [cited 2022; Available from: <https://www.manchestercfd.co.uk/post/all-there-is-to-know-about-different-mesh-types-in-cfd>].
45. Lidar, J., *Thermal Analysis of Engine Bay in Star-CCM+. Method Development and Correlation with Experimental Data*. 2018.
46. Behera, S.K.B. *Surface Repair Star-ccm+*. 2020 [cited 2022; Available from: <https://skill-lync.com/student-projects/surface-repair-star-ccm>].
47. Siemens. *2D & 3D CAD Modeling*. 2022 [cited 2022; Available from: <https://www.plm.automation.siemens.com/global/en/products/mechanical-design/2d-and-3d-cad-modeling.html>].
48. Exchanger, C. *How to convert Siemens NX to Open CASCADE?* 2022 [cited 2022; Available from: <https://cadexchanger.com/nx-to-brep/>].
49. Reitz, A. *Implicits and Fields for Beginners*. 2019 [cited 2022; Available from: <https://ntopology.com/blog/implicits-and-fields-for-beginners/>].
50. Courter, B. *B-rep vs. Implicit Modeling: Understanding the Basics*. 2019 [cited 2022; Available from: <https://ntopology.com/blog/understanding-the-basics-of-b-reps-and-implicits/>].
51. Al-Ketan, O. and R.K. Abu Al-Rub, *MSLattice: A free software for generating uniform and graded lattices based on triply periodic minimal surfaces*. Material Design & Processing Communications, 2021. **3**(6): p. e205.
52. Jamshed, S., *Using HPC for Computational Fluid Dynamics: A Guide to High Performance Computing for CFD Engineers*. 2015: Academic Press.

53. Simscale. *K-Omega and K-Omega SST*. 2021 [cited 2022; Available from: <https://www.simscale.com/docs/simulation-setup/global-settings/k-omega-sst/>].
54. EnggCyclopedia. *The importance of heat transfer surface area*. [cited 2022; Available from: <https://www.enggcyclopedia.com/2019/04/understanding-the-importance-of-surface-area/>].
55. Catchpole-Smith, S., *LASER POWDER BED FUSION OF LATTICE STRUCTURES FOR THERMOMECHANICAL APPLICATIONS*, in *Engineering*. 2019, University of Nottingham. p. 294.
56. Ahmadi, S., et al., *Mechanical behavior of regular open-cell porous biomaterials made of diamond lattice unit cells*. *Journal of the mechanical behavior of biomedical materials*, 2014. **34**: p. 106-115.
57. Arabnejad, S., et al., *High-strength porous biomaterials for bone replacement: A strategy to assess the interplay between cell morphology, mechanical properties, bone ingrowth and manufacturing constraints*. *Acta biomaterialia*, 2016. **30**: p. 345-356.
58. Ataee, A., et al., *Ultrahigh-strength titanium gyroid scaffolds manufactured by selective laser melting (SLM) for bone implant applications*. *Acta Materialia*, 2018. **158**: p. 354-368.
59. Bobbert, F., et al., *Additively manufactured metallic porous biomaterials based on minimal surfaces: A unique combination of topological, mechanical, and mass transport properties*. *Acta biomaterialia*, 2017. **53**: p. 572-584.
60. Campanelli, S.L., et al., *Manufacturing and characterization of Ti6Al4V lattice components manufactured by selective laser melting*. *Materials*, 2014. **7**(6): p. 4803-4822.
61. Cheng, X., et al., *Compression deformation behavior of Ti-6Al-4V alloy with cellular structures fabricated by electron beam melting*. *Journal of the mechanical behavior of biomedical materials*, 2012. **16**: p. 153-162.
62. Choy, S.Y., et al., *Compressive properties of Ti-6Al-4V lattice structures fabricated by selective laser melting: Design, orientation and density*. *Additive Manufacturing*, 2017. **16**: p. 213-224.
63. de Formanoir, C., et al., *Improving the mechanical efficiency of electron beam melted titanium lattice structures by chemical etching*. *Additive Manufacturing*, 2016. **11**: p. 71-76.
64. Deshpande, V.S., N.A. Fleck, and M.F. Ashby, *Effective properties of the octet-truss lattice material*. *Journal of the Mechanics and Physics of Solids*, 2001. **49**(8): p. 1747-1769.

65. Gümruk, R. and R. Mines, *Compressive behaviour of stainless steel micro-lattice structures*. International Journal of Mechanical Sciences, 2013. **68**: p. 125-139.
66. Han, C., et al., *Effects of the unit cell topology on the compression properties of porous Co-Cr scaffolds fabricated via selective laser melting*. Rapid Prototyping Journal, 2017. **23**(1): p. 16-27.
67. Harrysson, O.L., et al., *Direct metal fabrication of titanium implants with tailored materials and mechanical properties using electron beam melting technology*. Materials Science and Engineering: C, 2008. **28**(3): p. 366-373.
68. Hasib, H.B., *Mechanical Behavior of Non-Stochastic Ti-6Al-4V Cellular Structures Produced via Electron Beam Melting (EBM)*. 2011.
69. He, Z., et al., *Mechanical properties of copper octet-truss nanolattices*. Journal of the Mechanics and Physics of Solids, 2017. **101**: p. 133-149.
70. Hedayati, R., et al., *Mechanics of additively manufactured porous biomaterials based on the rhombicuboctahedron unit cell*. Journal of the mechanical behavior of biomedical materials, 2016. **53**: p. 272-294.
71. Heintl, P., C. Körner, and R.F. Singer, *Selective electron beam melting of cellular titanium: mechanical properties*. Advanced Engineering Materials, 2008. **10**(9): p. 882-888.
72. Helou, M., S. Vongbunyong, and S. Kara, *Finite element analysis and validation of cellular structures*. Procedia CIRP, 2016. **50**: p. 94-99.
73. Lei, H., et al., *Evaluation of compressive properties of SLM-fabricated multi-layer lattice structures by experimental test and  $\mu$ -CT-based finite element analysis*. Materials & Design, 2019. **169**: p. 107685.
74. Li, C., et al., *Crushing behavior of multi-layer metal lattice panel fabricated by selective laser melting*. International Journal of Mechanical Sciences, 2018. **145**: p. 389-399.
75. Liu, Y., et al., *Compressive and fatigue behavior of beta-type titanium porous structures fabricated by electron beam melting*. Acta Materialia, 2017. **126**: p. 58-66.
76. Mazur, M., et al., *Deformation and failure behaviour of Ti-6Al-4V lattice structures manufactured by selective laser melting (SLM)*. The International Journal of Advanced Manufacturing Technology, 2016. **84**(5): p. 1391-1411.
77. McKown, S., et al., *The quasi-static and blast loading response of lattice structures*. International Journal of Impact Engineering, 2008. **35**(8): p. 795-810.
78. Mines, R., et al., *Drop weight impact behaviour of sandwich panels with metallic micro lattice cores*. International Journal of Impact Engineering, 2013. **60**: p. 120-132.

79. Mullen, L., et al., *Selective Laser Melting: A regular unit cell approach for the manufacture of porous, titanium, bone in-growth constructs, suitable for orthopedic applications*. Journal of Biomedical Materials Research Part B: Applied Biomaterials: An Official Journal of The Society for Biomaterials, The Japanese Society for Biomaterials, and The Australian Society for Biomaterials and the Korean Society for Biomaterials, 2009. **89**(2): p. 325-334.
80. Murr, L., et al., *Microstructure and mechanical properties of open-cellular biomaterials prototypes for total knee replacement implants fabricated by electron beam melting*. Journal of the mechanical behavior of biomedical materials, 2011. **4**(7): p. 1396-1411.
81. Ozdemir, Z., et al., *Energy absorption in lattice structures in dynamics: Nonlinear FE simulations*. International Journal of Impact Engineering, 2017. **102**: p. 1-15.
82. Parthasarathy, J., et al., *Mechanical evaluation of porous titanium (Ti6Al4V) structures with electron beam melting (EBM)*. Journal of the mechanical behavior of biomedical materials, 2010. **3**(3): p. 249-259.
83. Ptochos, E. and G. Labeas, *Elastic modulus and Poisson's ratio determination of micro-lattice cellular structures by analytical, numerical and homogenisation methods*. Journal of Sandwich Structures & Materials, 2012. **14**(5): p. 597-626.
84. Rehme, O. and C. Emmelmann. *Rapid manufacturing of lattice structures with selective laser melting*. in *Laser-based Micropackaging*. 2006. SPIE.
85. Sallica-Leva, E., A. Jardini, and J. Fogagnolo, *Microstructure and mechanical behavior of porous Ti-6Al-4V parts obtained by selective laser melting*. Journal of the mechanical behavior of biomedical materials, 2013. **26**: p. 98-108.
86. Shen, Y., et al., *The mechanical properties of sandwich structures based on metal lattice architectures*. Journal of Sandwich Structures & Materials, 2010. **12**(2): p. 159-180.
87. Smith, M., Z. Guan, and W. Cantwell, *Finite element modelling of the compressive response of lattice structures manufactured using the selective laser melting technique*. International Journal of Mechanical Sciences, 2013. **67**: p. 28-41.
88. Suard, M., *Characterization and optimization of lattice structures made by Electron Beam Melting*. 2015, Université Grenoble Alpes (ComUE).
89. Tancogne-Dejean, T., A.B. Spierings, and D. Mohr, *Additively-manufactured metallic micro-lattice materials for high specific energy absorption under static and dynamic loading*. Acta Materialia, 2016. **116**: p. 14-28.
90. Ushijima, K., W. Cantwell, and D. Chen, *Prediction of the mechanical properties of micro-lattice structures subjected to multi-axial loading*. International Journal of Mechanical Sciences, 2013. **68**: p. 47-55.

91. Van Grunsven, W., et al., *Fabrication and mechanical characterisation of titanium lattices with graded porosity*. *Metals*, 2014. **4**(3): p. 401-409.
92. Xiao, L., et al., *Mechanical behavior of open-cell rhombic dodecahedron Ti-6Al-4V lattice structure*. *Materials Science and Engineering: A*, 2015. **640**: p. 375-384.
93. Yan, C., et al., *Microstructure and mechanical properties of aluminium alloy cellular lattice structures manufactured by direct metal laser sintering*. *Materials Science and Engineering: A*, 2015. **628**: p. 238-246.
94. Yáñez, A., et al., *Gyroid porous titanium structures: a versatile solution to be used as scaffolds in bone defect reconstruction*. *Materials & Design*, 2018. **140**: p. 21-29.
95. Yang, E., et al., *Effect of geometry on the mechanical properties of Ti-6Al-4V Gyroid structures fabricated via SLM: A numerical study*. *Materials & Design*, 2019. **184**: p. 108165.
96. Zadpoor, A.A. and R. Hedayati, *Analytical relationships for prediction of the mechanical properties of additively manufactured porous biomaterials*. *Journal of Biomedical Materials Research Part A*, 2016. **104**(12): p. 3164-3174.
97. Zaharin, H.A., et al., *Effect of unit cell type and pore size on porosity and mechanical behavior of additively manufactured Ti6Al4V scaffolds*. *Materials*, 2018. **11**(12): p. 2402.
98. Murr, L., et al., *Open-cellular Co-base and Ni-base superalloys fabricated by electron beam melting*. *Materials*, 2011. **4**(4): p. 782-790.
99. Beyer, C. and D. Figueroa, *Design and analysis of lattice structures for additive manufacturing*. *Journal of Manufacturing Science and Engineering*, 2016. **138**(12).
100. Borleffs, M., *Finite element modeling to predict bulk mechanical properties of 3D printed metal foams*. 2012.
101. Hedayati, R., et al., *Comparison of elastic properties of open-cell metallic biomaterials with different unit cell types*. *Journal of Biomedical Materials Research Part B: Applied Biomaterials*, 2018. **106**(1): p. 386-398.
102. Hedayati, R., et al., *Mechanical properties of regular porous biomaterials made from truncated cube repeating unit cells: Analytical solutions and computational models*. *Materials Science and Engineering: C*, 2016. **60**: p. 163-183.
103. Hedayati, R., et al., *Mechanical behavior of additively manufactured porous biomaterials made from truncated cuboctahedron unit cells*. *International Journal of Mechanical Sciences*, 2016. **106**: p. 19-38.
104. Hedayati, R., et al., *Analytical relationships for the mechanical properties of additively manufactured porous biomaterials based on octahedral unit cells*. *Applied Mathematical Modelling*, 2017. **46**: p. 408-422.

105. Liu, Y., et al., *Microstructure, defects and mechanical behavior of beta-type titanium porous structures manufactured by electron beam melting and selective laser melting*. Acta materialia, 2016. **113**: p. 56-67.
106. Murr, L.E., et al., *Next-generation biomedical implants using additive manufacturing of complex, cellular and functional mesh arrays*. Philosophical Transactions of the Royal Society A: Mathematical, Physical and Engineering Sciences, 2010. **368**(1917): p. 1999-2032.
107. Ushijima, K., et al., *An investigation into the compressive properties of stainless steel micro-lattice structures*. Journal of Sandwich Structures & Materials, 2011. **13**(3): p. 303-329.
108. Yan, C., et al., *Evaluations of cellular lattice structures manufactured using selective laser melting*. International Journal of Machine Tools and Manufacture, 2012. **62**: p. 32-38.
109. Yan, C., et al., *Advanced lightweight 316L stainless steel cellular lattice structures fabricated via selective laser melting*. Materials & Design, 2014. **55**: p. 533-541.
110. Yan, C., et al., *Ti-6Al-4V triply periodic minimal surface structures for bone implants fabricated via selective laser melting*. Journal of the mechanical behavior of biomedical materials, 2015. **51**: p. 61-73.
111. Zhao, M., et al., *Improved mechanical properties and energy absorption of BCC lattice structures with triply periodic minimal surfaces fabricated by SLM*. Materials, 2018. **11**(12): p. 2411.
112. Zhu, H., J. Knott, and N. Mills, *Analysis of the elastic properties of open-cell foams with tetrakaidecahedral cells*. Journal of the Mechanics and Physics of Solids, 1997. **45**(3): p. 319-343.
113. Bai, M. and J. Chung, *Analytical and numerical prediction of heat transfer and pressure drop in open-cell metal foams*. International Journal of Thermal Sciences, 2011. **50**(6): p. 869-880.